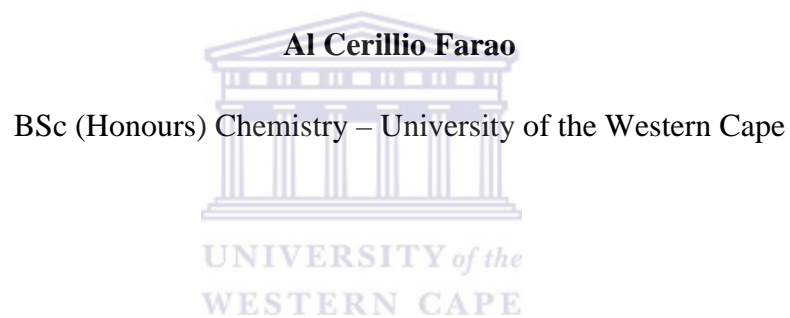


# **The Composition of Photocatalytic Nanofibres through Electrospinning**

**By**



**A thesis submitted in partial fulfilment of the requirements for the degree of  
Magister Nano Science in the Department of Chemistry, University of the  
Western Cape.**

**Supervisor: Professor Leslie F. Petrik**

**Co-supervisor: Dr O Babajide**

**May 2014**

# **The Composition of Photocatalytic Nanofibres through Electrospinning**

**By**



## **KEYWORDS**

Anatase phase

Amorphous phase

Electrospinning

Nanofibres

Photocatalytic degradation

Photocatalysis

Photonic efficiency

Titanium dioxide

## ABSTRACT

The reported application of TiO<sub>2</sub> as photocatalyst for the removal of cyanide from water in 1977 stimulated meaningful interests in the environmental applications of photocatalysis. By supporting TiO<sub>2</sub> on electrospun nanofibres, with their large surface to volume ratio, the limitations of powdered TiO<sub>2</sub> such as solution fouling, light scattering, separation after use and loss of active surface can be eliminated. The aim of this study was to enrich electrospun fibres with the active mineral phase TiO<sub>2</sub> nanoparticles and then to evaluate how well the composite fibres performed in the photocatalytic degradation of methylene blue (MB). Electrospun hydrophobic PAN polymer fibres were used as support structures for the TiO<sub>2</sub> nanoparticles. The photocatalytic activity of the TiO<sub>2</sub> enriched fibres for dye degradation was evaluated and the effect of external stressors on the fibres was assessed. A comparison was also made to determine whether the TiO<sub>2</sub> - photocatalyst catalyst should be coated on top of, or loaded inside the electrospun PAN fibres.

The composite fibres were synthesised by either coating commercial electrospun PAN nanofibres with a titanium precursor using a thermal method or by incorporating various loadings of powdered TiO<sub>2</sub> into a 7 wt% PAN/DMF polymer sol-gel solution prior to electrospinning. The first method involved the deposition of a titanium dioxide precursor onto pre-made commercial electrospun polymer nanofibres and crystallising the amorphous titania to the TiO<sub>2</sub> anatase crystal phase by means of a heat treatment step. The second method involved the incorporation of commercial powdered TiO<sub>2</sub> into the polymer sol-gel solution prior to electrospinning. Four concentration profiles of each fibre type were prepared.

The nanofibres that were coated with TiO<sub>2</sub> were prepared by drop coating solubilised titanium oxy acetylacetonate onto commercial electrospun PAN fibres. Four concentration profiles of the TiO<sub>2</sub> coated nanofibres were prepared by coating the electrospun nanofibres with 10, 15, 20 or 30 wt% of the solubilised titanium precursor. Thermal annealing and oxidative stabilisation of the TiO<sub>2</sub> coated fibres was achieved by heating the drop coated PAN fibres to 275 °C at a

heating rate of 1 °C per minute in air. The temperature was maintained for 1 hour that was succeeded by cooling of the fibres to room temperature.

The TiO<sub>2</sub> coated carbonised fibres were prepared using a similar synthesis method. The only difference between the oxidatively stabilised nanofibres and the carbonised nanofibres' synthesis procedure was the addition of a carbonisation step that followed after the oxidative stabilisation step. After the stabilisation step some of the fibres were carbonised by heating from 275 °C to 400 °C at a heating rate of 5 °C per minute in nitrogen gas with a 2 cm<sup>2</sup>/min flow rate. The temperature of 400 °C was maintained for 1 hour whereafter the fibres were cooled to room temperature under nitrogen gas. TGA analysis indicated that cyclisation of the PAN polymer took place between 285 and 300 °C and that carbonisation of the polymer initiated at 400 °C. During this step the fibres were oxidized from a thermoplastic polymer to a brittle non-plastic cyclic carbonaceous compound. FTIR analysis of the fibres coated with TiO<sub>2</sub> revealed no coordination between the catalyst and the fibres. All that could be concluded from the data was that the thermal treatment steps proved not to enhance fibre performance. Although carbonisation of PAN fibres is considered to enhance the stability of the fibres for the application as catalyst support structures this thermal pre-treatment step can be excluded.

The photocatalytic activities of the TiO<sub>2</sub> coated fibres were evaluated by submerging the fibres in 100 mL solutions of a range of methylene blue (MB) concentrations exposed to 254 nm UV light source. The study was conducted over 8 hours. Experimental results of the averaged photocatalytic activity for the oxidatively stabilised TiO<sub>2</sub> coated fibres achieved a maximum MB degradation of only 48 % over the 8 hour period. The TiO<sub>2</sub> coated carbonised fibres displayed very little to no photocatalytic activity over the 8 hour period under similar conditions.

In order to synthesise PAN nanofibres embedded with TiO<sub>2</sub>, rheological analysis was first performed on PAN/DMF sol-gel solutions of different concentrations in order to determine the optimum PAN/DMF wt% ratio required to electrospin continuous nanofibres and also to determine the rheological properties of the

various sol-gel solutions. The rheological analysis showed that the flow curves of the polymer solutions were representative of non-Newtonian fluid behaviour elicited at different polymer concentrations. HRSEM revealed bead formation to be more prevalent with the 6 wt% PAN/DMF sol-gel and identified the ideal sol-gel formulation to be the 7 wt% PAN/DMF solution. Nanoparticulate TiO<sub>2</sub> was then incorporated into the 7 wt% PAN/DMF sol-gel prior to electrospinning the nanofibres and the polymer concentration and catalyst loading evaluated. The electrospun fibres loaded with commercial powdered TiO<sub>2</sub> were thus prepared by mixing 5 g of the 7 wt% PAN/DMF sol-gel with 3, 5, 7 or 10 wt% of commercial nanoparticulate TiO<sub>2</sub>. The mixture was stirred and vortex mixed to facilitate adequate dispersion of the TiO<sub>2</sub> nanoparticles. The TiO<sub>2</sub> containing polymer sol-gel was then electrospun with an applied potential of 17.5 kV over a tip collector distance of 13.5 cm and fibres were collected on a stationary collector plate. HRSEM and TEM analysis were used to identify the ideal TiO<sub>2</sub> powder loading for adequate catalyst distribution in the polymer fibres. EDS indicated a positive correlation between the actual and theoretical Ti loading when electrospinning nanofibres from the PAN/DMF sol-gel loaded with commercial Ti powder. The XRD results confirmed the TiO<sub>2</sub> anatase structure in the PAN fibres containing commercial TiO<sub>2</sub> powder. DSC suggested that incorporating TiO<sub>2</sub> in the electrospun polymer fibres improved the thermal stability of the PAN fibres.

Experimental results of the TiO<sub>2</sub> loaded PAN fibres showed that 5 wt% loaded (EF-04b) TiO<sub>2</sub> electrospun PAN fibres yielded the greatest photocatalytic degradation of methylene blue. The 20 mg fibres samples achieved a maximum photocatalytic degradation of 90 % of the 100 mL 10 mg/L methylene blue dye solution over the 8 hour testing period using UV light (UV illumination wavelength of 254 nm and 1.242 W/m<sup>2</sup> UV intensity). The electrospun nanofibres containing 3, 5, 7 and 10 wt% of the commercial powdered TiO<sub>2</sub> outperformed the commercial powdered TiO<sub>2</sub> itself as well as the commercial PAN electrospun nanofibres coated with Ti precursor catalyst. In terms of catalyst loading, incorporating the TiO<sub>2</sub> catalyst into the polymer nanofibres was more effective than coating the TiO<sub>2</sub> catalyst onto the surface of the PAN fibres. The commercial TiO<sub>2</sub> nanoparticles appeared to be better dispersed inside the fibres and the

loading of the  $\text{TiO}_2$  catalyst was also much easier. Durability testing, up to 12 hours, with 100 mL 4 mg/L peroxide solutions under UV-light illumination (254 nm) revealed the  $\text{TiO}_2$  loaded electrospun PAN fibres could lose viscoelasticity under accelerated aging conditions. The composite  $\text{TiO}_2$  containing electrospun fibres are therefore suitable for application as supported photocatalysts in advanced oxidation process systems for organic decomposition, but their long term durability may need improvement.

The outcome of the research was to provide a route to prepare robust, highly photoactive, supported  $\text{TiO}_2$  PAN nanofibres of 300 nm diameter which did not require thermal stabilisation. The study demonstrated that such fibres when illuminated by 9 W UV light with 254 nm wavelength could achieve more than 90 % decomposition of methylene blue dye (10 mg/L MB 4 cm from the light source) within 8 hours, which has not been reported in literature to date.



## DECLARATION

I declare that “*The Composition of Photocatalytic Nanofibres through Electrospinning*” is my own work, that it has not been submitted for any degree or examination in any other university, and that all the resources I have used or quoted have been indicated and acknowledged by complete references.



Al Cerillio Farao

May 2014

Signed.....

## ACKNOWLEDGEMENTS

I would like to express my sincere appreciation to the following people who have made it possible for me to complete this study:

- All glory and honour to the Lord, my God for his blessings.
- My parents Cerillio and Greta for all their sacrifices and unconditional love, guidance, motivation and support throughout my studies and affording me so many opportunities.
- My supervisor Professor L Petrik for her guidance, patience and wisdom affording me the freedom to really have fun with the study.
- My girl friend Kim for her love, support and patience seeing me through tough times.
- Drs Trevor and Colleen Moodley for their support, guidance and their willingness to always assist me.
- Ms V Jamalie, Ms C Abrahams and Professor D Knoesen for their support and assistance. This program would have not been possible without them.
- Dr O Ayanda for his assistance, A. Abbott, V. Kellerman, I Wells, R Richards and the rest of my colleagues at the ENS group for their companionship and for making life comfortable for the duration of my study.
- Mr A Josephs and Dr F Cummings in the Physics department, Ms A Ramplin and Mr Y Kippie from the School of Pharmacy and Dr W Davids from SAIAMC at UWC for their assistance in TEM, HRSEM, FTIR, DSC and TGA analysis.
- Professor F Ameer, Professor E Iwuoha and the department of chemistry for affording me this opportunity.
- I would also like to acknowledge Mr N Hendricks for his technical support

In conclusion I recognise that this research would have not been possible without the financial assistance from the Department of Science and Technology's nanoscience and nanotechnology programme.

## TABLE OF CONTENTS

KEYWORDS.....	i
ABSTRACT.....	ii
DECLARATION.....	vi
ACKNOWLEDGEMENTS.....	vii
TABLE OF CONTENTS.....	viii
LIST OF FIGURES.....	xiii
LIST OF TABLES.....	xvi
LIST OF ABBREVIATIONS.....	xvii
CHAPTER 1.....	1
1: INTRODUCTION.....	1
1.1 Background.....	1
1.1.1 Photocatalysis.....	1
1.1.2 Electrospinning.....	3
1.2 Problem statement.....	5
1.3 Motivation and objectives.....	6
1.4 Hypothesis.....	7
1.5 Research questions.....	8
1.6 Research approach.....	8
1.7 Scope and delimitations of the thesis.....	11
1.8 Thesis structure.....	11

CHAPTER 2.....	13
2: LITERATURE REVIEW.....	13
2.1 Electrospinning.....	13
2.1.1 Single needle electrospinning.....	14
2.1.2 Electrospinning parameters.....	18
2.1.3 Processing Parameters.....	22
2.2 Polyacrylonitrile.....	26
2.3 Advance Oxidation Processes.....	31
2.3.1 Heterogeneous photocatalysis.....	32
2.3.2 The Fenton process.....	34
2.3.3 Electrochemical methods.....	35
2.4 Environmental catalysis.....	35
2.4.1 Titanium Dioxide (TiO <sub>2</sub> ).....	36
2.4.2 Challenges associated with TiO <sub>2</sub> .....	42
2.4.3 Catalysis from nano to macro scale.....	43
2.4.4 Catalyst support structures.....	44
2.5 Electrohydraulic discharge reactors.....	49
2.6 Characterisation of nanomaterials.....	50
2.7 Summary.....	51
CHAPTER 3.....	53
3: METHODOLOGY.....	53
3.1 Chemicals and Equipment.....	55
3.2 Electrospinning chemical parameters.....	55

3.3	Electrospinning physical parameters.....	57
3.4	Ambient Parameters.....	58
3.5	Deposition of TiO <sub>2</sub> into and onto the electrospun nanofibres.....	58
3.5.1	Doping of the PAN sol-gel with TiO <sub>2</sub> .....	58
3.5.2	Deposition of TiO <sub>2</sub> on top of electrospun nanofibres.....	60
3.6	Photocatalytic study.....	63
3.6.1	Dye degradation analysis.....	65
3.6.2	Photolysis of H <sub>2</sub> O <sub>2</sub> for OH radical formation.....	65
3.7	Characterization techniques.....	66
3.7.1	Rheological analysis.....	66
3.7.2	Physical characterization.....	66
3.7.2.1	High Resolution Scanning Electron Microscopy (HRSEM)	66
3.7.2.2	Energy Dispersive Spectroscopy (EDS).....	67
3.7.2.3	Transition Electron Microscopy (TEM).....	67
3.7.3	X-ray Diffraction Spectroscopy (XRD).....	68
3.7.4	RAMAN Spectroscopy.....	69
3.7.5	Fourier Transform Infrared (FTIR).....	70
3.7.6	Thermal Gravimetric Analysis (TGA).....	70
3.7.7	Differential Scanning Calorimetry (DSC).....	70
CHAPTER 4	.....	71
4:	Rheology of PAN polymer sol-gel and characteristics of electrospun fibres.....	71
4.1	Introduction.....	71
4.1.1	Optimum sol-gel formulation.....	71

4.1.2 Morphology of electrospun fibres.....	74
4.2 Fourier Transform Infrared Spectroscopy (FTIR).....	80
4.3 Thermal Gravimetric Analysis (TGA).....	81
4.4 Summary.....	82
CHAPTER 5.....	83
5: CHARACTERIZATION OF THE TiO <sub>2</sub> DOPED ELECTROSPUN FIBRES: RESULTS AND DISCUSSION.....	83
5.1 Introduction.....	83
5.1.1 Characterization of the composite polymer fibre fabrication.....	84
5.1.1.1 Morphology of EF-04a.....	85
5.1.1.2 Morphology of EF-04b.....	86
5.1.1.3 Morphology of EF-04c.....	88
5.1.1.4 Morphology of EF-04d.....	90
5.1.2 Electron Dispersive X-ray Spectroscopy.....	92
5.1.3 X-ray Diffraction Spectroscopy.....	93
5.1.4 Raman spectroscopy.....	95
5.1.5 Fourier Transform Infrared Spectroscopy.....	96
5.1.6 Photocatalytic electrospun nanofibres exposure to H <sub>2</sub> O <sub>2</sub> photolysis.....	97
5.1.7 Differential Scanning Calorimetry.....	98
5.2 Characterization of oxidatively stabilised composite nanofibres.....	99
5.2.1 Morphology of oxidatively stabilised composite nanofibres.....	100
5.2.2 Energy Dispersive X-ray Spectroscopy.....	102
5.2.3 X-ray Diffraction Spectroscopy.....	104

5.2.4 Fourier Transform Infrared spectroscopy.....	105
5.3 Carbonisation of the commercial PAN nanofibres.....	106
5.3.1 Preparation of the carbonised commercial nanofibres.....	106
5.3.2 Energy Dispersive X-ray Spectroscopy.....	109
5.3.3 X-ray Diffraction Spectroscopy.....	111
5.3.4 Fourier Transform Infrared Spectroscopy.....	112
5.4 Summary.....	113
CHAPTER 6.....	115
6: Photocatalytic degradation of methylene blue.....	115
6.1 Baseline study.....	115
6.2 Photocatalytic activity of EF-04 series nanofibres.....	119
6.3 Photocatalytic activity of EF-05 – EF-08 nanofibres.....	123
6.4 Photocatalytic activity of EF-09 – EF-12 nanofibres.....	126
6.5 Summary.....	128
CHAPTER 7.....	130
7: Conclusions and Recommendations.....	130
7.1 Introduction.....	130
7.2 Conclusions of this research.....	130
7.3 Recommendations and future work.....	133
References.....	135
Appendix.....	155

## LIST OF FIGURES

Figure 1.1: Schematic description of research approach.....	9
Figure 2.1: Schematic description of the standard two types of electrospinning setups.....	15
Figure 2.2: Schematic description of a bubble electrospinning setup.....	16
Figure 2.3: Schematic description of an electroblowing setup.....	16
Figure 2.4: Schematic description of porous hollow tube electrospinning.	17
Figure 2.5: Schematic description of roller electrospinning.....	18
Figure 2.6: Schematic description of molecular structure of PAN polymer.....	27
Figure 2.7: Schematic description of cyclisation and dehydrogenation of PAN.....	29
Figure 2.8: FTIR spectra of PAN fibres.....	30
Figure 2.9: Raman spectra of PAN nanofibres.....	30
Figure 2.10: XRD spectra of PAN fibres.....	31
Figure 2.11: An energy band gap diagram of TiO <sub>2</sub> .....	34
Figure 2.12: Schematic description of photo-induced superhydrophilicity.	37
Figure 2.13: Primary process involved in mineralization of organic compounds.....	39
Figure 2.14: Crystalline structures of TiO <sub>2</sub> .....	40
Figure 2.15: XRD spectra of nanostructure XRD.....	41
Figure 2.16: FTIR spectra of TiO <sub>2</sub> and modified TiO <sub>2</sub> .....	42
Figure 2.17: SEM image of a TiO <sub>2</sub> nanotube.....	47
Figure 3.1: Research methodology of the photocatalytic study.....	54
Figure 3.2: Horizontal electrospinning setup employed in the study.....	58

Figure 3.3: Experimental setup of photocatalytic degradation of MB dye..	64
Figure 3.4: Characteristic XRD spectrum of TiO and anatase crystal phase TiO <sub>2</sub> .....	69
Figure 4.1: Shear stress versus shear rate for PAN/DMF sol-gel .....	72
Figure 4.2: The effect of polymer concentration on sol-gel viscosity.....	73
Figure 4.3: HRSEM images of preliminary electrospun fibres.....	75
Figure 4.4: HRSEM image of the 6 wt% PAN/DMF electrospun nanofibres.....	76
Figure 4.5: HRSEM image of the 8 wt% PAN/DMF electrospun nanofibres.....	77
Figure 4.6: HRSEM image of the 10 wt% PAN/DMF electrospun nanofibres.....	77
Figure 4.7: The effect of polymer concentration on fibre diameter.....	79
Figure 4.8: FTIR spectra of blank 7 wt% PAN electrospun nanofibres.....	80
Figure 4.9: The TGA spectra of 7wt% PAN electrospun nanofibres.....	81
Figure 5.1: HRSEM image of EF-04a.....	85
Figure 5.2: HRSEM image of EF-04a where TiO <sub>2</sub> breach the surface.....	86
Figure 5.3: HRSEM image of EF-04b.....	87
Figure 5.4: HRSEM image of EF-04b where TiO <sub>2</sub> breach the surface.....	88
Figure 5.5: HRSEM image of EF-04c.....	89
Figure 5.6: HRSEM image of bead morphology of EF-04c.....	89
Figure 5.7: HRSEM image of EF-04d.....	90
Figure 5.8: HRSEM image of morphology of EF-04d.....	91
Figure 5.9: TEM image of EF-04d.....	92
Figure 5.10: XRD spectra of EF-04b.....	94

Figure 5.11: Raman spectra of EF-04b.....	95
Figure 5.12: FTIR spectra of EF-04b.....	96
Figure 5.13: FTIR spectra of EF-04b chemical stability assessment.....	97
Figure 5.14: FTIR spectra of EF-04b chemical stability after 2, 4, 6 and 12 hours.....	98
Figure 5.15: DSC spectra of TiO <sub>2</sub> containing PAN and bare PAN fibre....	99
Figure 5.16: HRSEM images of EF-05 – EF-08 series nanofibres.....	101
Figure 5.17: HRSEM image of EF-05.....	102
Figure 5.18: XRD spectra of EF-06.....	104
Figure 5.19: HRSEM images of EF-09 – EF-12 series nanofibres.....	107
Figure 5.20: HRSEM image of EF-12.....	108
Figure 5.21: Bar graph of actual loading of Ti on the nanofibres.....	110
Figure 5.22: XRD spectra of EF-09.....	111
Figure 6.1: Aqueous MB decolouration for the control group.....	116
Figure 6.2: Kinetics of photocatalytic MB degradation by powdered TiO <sub>2</sub> .	117
Figure 6.3: Aqueous MB decolouration for EF-04 series nanofibres.....	120
Figure 6.4: Kinetics of photocatalytic MB degradation by EF-04 series nanofibres.....	121
Figure 6.5: Aqueous MB decolouration for the EF-05 – EF-08 series nanofibres.....	124
Figure 6.6: Kinetics of photocatalytic degradation of MB by EF-05 – EF- 08 series nanofibres.....	125
Figure 6.7: Aqueous MB decolouration for the EF-09 – EF-12 series nanofibres.....	127

## LIST OF TABLES

Table 2.1: Solution properties for PAN nanofibre fabrication.....	28
Table 2.2: Photocatalytic mineralization of organic compounds.....	38
Table 3.1: Table of chemicals used in the study.....	55
Table 3.2: Table of equipment used in the study.....	55
Table 3.3: Formulation of polymer solutions.....	56
Table 3.4: Physical parameters used for electrospinning.....	57
Table 3.5: Summary of the catalyst loading on the electrospun titanium nanofibres.....	59
Table 3.6: Summary of the electrospun PAN polymer nanofibres.....	60
Table 3.7: Thermal conditions for stabilisation and carbonisation.....	62
Table 3.8: Summary of the commercial nanofibres coated with TiO <sub>2</sub> .....	62
Table 3.9: XRD instrument conditions.....	68
Table 5.1: EDS data of the Ti wt% on the EF-04 series nanofibres.....	93
Table 5.2: EDS data of the Ti wt% on the EF-05 – EF-08 series nanofibres.....	103
Table 5.3: FTIR absorbance of EF-08.....	105
Table 5.4: EDS data of the Ti wt% on the EF-09 – EF-12 series nanofibres.....	109
Table 5.5: FTIR absorbance of EF-09.....	112
Table 6.1: The decolouration of MB during the photocatalyst study for commercial powdered TiO <sub>2</sub> .....	118
Table 6.2: The degradation of MB during the photocatalyst study for the EF-04 series nanofibres.....	122
Table 6.3: The degradation of MB during the photocatalyst study for the EF-05 – EF-08 series nanofibres.....	125

## LIST OF ABBREVIATIONS

AC	- activated carbon
Acac	- acetylacetonate
Abs	- absorbance
AOP	- advance oxidation processes
at %	- atomic percentage
CVD	- chemical vapour deposition
DMAc	- dimethylacetamide
DMF	- dimethylformamide
DMSO	- dimethyl sulfoxide
DSC	- differential scanning calorimetry
DTAB	- dodecyltrimethylammonium bromide
EDS	- energy dispersive spectroscopy
EF	- Electro-Fenton
FTIR	- Fourier transform infrared
HRSEM	- high resolution scanning electron microscopy
k	- rate constant
LCA	- life cycle assessment
MB	- methylene blue
PAN	- polyacrylonitrile
PMCS	- pulsed microplasma cluster source
PS	- polystyrene
PVP	- polyvinylpyrrolidone

RH	- relative humidity
TEM	- transmission electron microscopy
THF	- tetrahydrofuran
TiO <sub>2</sub>	- titanium dioxide
TGA	- thermogravimetric analysis
UV	- ultra violet
Vis	- visible
wt%	- weight percentage
XRD	- x-ray diffraction



## Chapter 1

### 1. Introduction

The aim of chapter one is to give an overview of the objectives and a brief introduction to key aspects of the study.

The scope of the thesis is defined within this section. The chapter also sums up the problem statement, the motivation and objectives of the study are also clearly stated.

#### 1.1 Background

Photocatalysis utilizes solar or UV radiation to accelerate the rate of chemical redox reactions, usually on semiconductor oxides. Advanced oxidation processes (AOP), including photocatalytic degradation, is gradually increasing in popularity as a viable method for the removal of organic pollutants from water (Andreozzi *et al.*, 1999). The AOP processes generate reactive hydroxyl radicals which are precursors for the degradation of organic and inorganic pollutants. In heterogeneous photocatalysis semiconductors generate radicals through redox reactions by absorbing photons, adsorbing organic pollutants, oxidizing the pollutants and desorbing the products into the heterogeneous environment. Titanium dioxide (TiO<sub>2</sub>) is the most commonly used photocatalyst. However, despite its potential, in its particulate form, it is an environmental hazard which impedes its true potential. In order to access the potential of TiO<sub>2</sub>, the catalyst will have to be supported without altering the novel characteristics of these nanomaterials.

##### 1.1.1 Photocatalysis

The purpose of a photocatalyst is to generate a charge carrier by band gap excitation, an ability that only semiconductors possess. Heterogeneous photocatalysis forms part of the advanced oxidative processes. It has established itself as a suitable technology for air and water treatment (Herman, 1999). Photocatalytic degradation using solar radiation offered promising prospects (Xiao *et al.*, 2009). The difference between conventional catalysis and advanced

oxidative catalysis is the mode of activation. In advanced oxidative catalysis photonic activation replaces thermal activation of the conventional catalytic systems. With heterogeneous photocatalysis, semiconductor particles have the ability to utilize sunlight to degrade organic and inorganic contaminants. Semiconductors can be activated by solar radiation where the irradiation energy can either be equal to or exceed the band-gap energy of the semiconductor (Herrmann, 1999). By bridging this gap, electrons can travel between the energy levels. Once the semi conductor is illuminated with photons, there is an absorption of photons which creates electron-hole pairs. An electron in the valence band is excited and migrates toward the conduction band to form the photogenerated electron creating a photogenerated hole in the valence band (Linsebigler *et al.*, 1995).

TiO<sub>2</sub> performance has been most promising in overcoming the limitations experienced by other semiconductors. TiO<sub>2</sub> has two active forms anatase and rutile, the former being more active due to a higher reduction potential. TiO<sub>2</sub> in its nano form is much more suitable for photocatalytic applications than its bulkier counterpart (Diebold, 2003). TiO<sub>2</sub> does however have a very wide band-gap, restricting its functionality to the UV region and thus only utilizes five percent of the solar spectrum. However its oxidative versatility, simplicity and low cost make it the ideal photocatalyst (Andreozzi *et al.*, 1999).

At the nano scale classical physics do not apply and quantum mechanics need to be consulted. Nanoparticles form a new class of material that exhibit completely new properties and characteristics in comparison to molecular and bulk states (Lue and Nalwa, 2007). The physical dimensions of nanomaterials impart unique properties that are very advantageous for catalysis. The high surface area and surface to bulk ratio of nanomaterials enhance reaction rates due to increased active sites (Chen and Mao, 2007).

A number of techniques have been developed for the synthesis of nano-TiO<sub>2</sub> catalysts of different size and morphologies. The synthetic routes can either be gas phase or solution phase, each technique adding its own unique trait to the final product. Solution phase techniques are mainly used for the synthesis of thin films

and powders. The gas phase techniques include chemical vapour deposition, physical vapour deposition and spray pyrolysis deposition. These techniques are mainly used in thin film synthesis. By varying the reaction conditions it is possible to manipulate the properties of the nanoparticles such as the phase composition, particle size, porosity, surface area and band gap (Chen and Mao, 2007; Carp *et al.*, 2004).

### **1.1.2 Electrospinning**

Electrospinning is a low cost technique and has the ability to reproduce inherent surface morphologies of materials onto nanofibres (Ramakrishna *et al.*, 2006). Electrospinning has generally been accepted as a versatile technique to consistently produce fibres in the submicron range. These fibres display extremely high surface to weight ratios compared to normal nonwovens that can assist in overcoming the limitations associated with free form photocatalysts (Wang *et al.*, 2013).

Electrospinning is a technique that uses electrical forces to form electrostatic polymer fibres with diameters ranging from 2 nm up to the micrometer range. Nanofibres can be extruded from melt mixtures of both natural and synthetic polymers (Liang *et al.*, 2007). Electrospinning can consistently produce fibres in the submicron range and because of its versatility it can spin a range of polymer fibres producing fabrics with controllable pore structures. The nanofibres that are produced in electrospinning offer a very high surface to volume ratio. By altering the chemical and ambient parameters it is possible to manipulate the pore size of the fibres (Stoilova, 2010). The ability to control the composition of the fibres to acquire certain properties and functionality has stimulated a lot of interest and research in this field (Bhardwaj and Kundu, 2010).

Electrospinning is considered a simple and effective technique for the fabrication of polymer, organic and composite fibres. By incorporating inorganic nanoparticles into the sol-gel functional composite fibres can be synthesized. Different types of polymer composites have been synthesized by incorporating nanoparticles into the polymer matrix (Bai *et al.*, 2011). Polymer melts containing

titanium precursors have been subjected to an electric potential to produce titanium fibres. As the applied potential exceeded the surface tension of the nano polymer composite it extruded from the spinneret in fibrous fashion. By manipulating the spinning parameters, the morphology and diameter of TiO<sub>2</sub> nanofibres that were produced could be optimised (Li and Xia, 2003).

Electrostatic forces are used to spin fibres from a polymer melt with a thinner diameter and larger surface area than normal fibres. There are standard vertical and horizontal setups for electrospinning. In the vertical setup the electrical field is perpendicular to the floor and in the horizontal setup; the electrical field is horizontal to the floor (Bhardwaj and Kundu, 2010).

An electrospinning system has three critical components, a high voltage power supply, a spinneret and a grounded collecting plate. Electrospinning is performed at room temperature to spin the melt into fibres under atmospheric conditions. Once dissolved, the melt is introduced to a capillary tube before electrospinning commences. The melt is then subjected to the electric field. During electrospinning the high voltage power supply passes a current through the melt, the dissolved polymer composite. Once the applied potential reaches the critical value and the repulsive force is greater than the surface tension, the melt is forced to extrude from the spinneret (Lyons *et al.*, 2004). The jet is electrically charged, causing the extruded fibres to bend in a chaotic fashion. Each time the fibre loops, the diameter is reduced until it is collected on a grounded collector (Ramakrishna *et al.*, 2006). Electrospinning has actively been studied for its application with polymers. Recently, electrospinning has been employed to electrospin polymer sol-gels loaded with photocatalysts (Prahsarn *et al.*, 2011). These fibres have relatively large surface to volume ratios and can serve as suitable structural supports for the photocatalysts. Previously PAN-based fibre webs containing TiO<sub>2</sub> have been successfully electrospun for the photodegradation of rhodamine B dye. The TiO<sub>2</sub> particles were dispersed on the fibres. SEM images showed the areas on the nanofibres where the TiO<sub>2</sub> nanoparticles were absent to be smooth with an average diameter of 800 nm. The fibres successfully degraded the organic dye with a maximum of 80% dye removal over 38 hours (Im *et al.*, 2008). TiO<sub>2</sub>

nanofibres have also been utilised as photocatalysts for hydrogen evolution. These fibres were electrospun from a polyvinylpyrrolidone (PVP) sol-gel doped with a titanium precursor, titanium butoxide. TiO<sub>2</sub> nanofibres, 260 – 355 nm in diameter, were obtained from calcination at temperatures ranging from 300 to 700°C (Chuangchote *et al.*, 2009). A study by Zhao *et al.* (2007) reported the successful fabrication of photoluminescent TiO<sub>2</sub>/PVP composite nanofibres with an average fibre diameter of 40 nm. The fibres were subjected to a high electric field strength. After spinning the composite fibres were left in air for 24 hours to allow for the complete hydrolysis of the titanium dioxide precursor. The fibres were then calcined in air for 3 hours at different temperatures. All these studies were attempts to maintain photocatalytic activity whilst supporting the active TiO<sub>2</sub> components on a suitable support.

## 1.2 Problem statement

The use of nanoparticles in consumer products is increasing rapidly. In this economy driven society nanotechnology based products are increasing at a pace where the assessment regarding the toxicity of these materials is lagging (Rejeski and Lekas, 2008). The release of nanoparticles into aquatic systems can expose humans to bioaccumulation effects. Currently existing water treatment and purification methods are not designed to remove nanopollutants. Nanoparticles may facilitate the transport of chemicals into treated waters via adsorption and other chemical reactions (Roux, 2008).

Presently there are several issues associated with TiO<sub>2</sub> in particulate form. When used as photocatalysts, TiO<sub>2</sub> nanoparticles can cause a shadowing effect which relates to reducing light penetration during catalyst loading. This adversely affects its photocatalytic efficiency by decreasing the penetration depth of solar radiation (Xiao *et al.*, 2008). Due to its large band gap, TiO<sub>2</sub> is only functional in the UV range of the solar spectrum and can only use about 4% of sunlight. The particulates can also not be used in the free particulate form as it is difficult to remove from water. TiO<sub>2</sub> nanoparticulates are often phototoxic to cells in vitro and can intoxicate marine phytoplankton (Hamzeh and Sunahara, 2013). TiO<sub>2</sub> can also mediate the diffusion of reactive oxidizing species onto the cell wall of

organisms. An increase in concentration of oxidizing species can increase the oxidative stress in seawater contaminated with TiO<sub>2</sub> (Miller *et al.*, 2012). To overcome these problems TiO<sub>2</sub> needs to be fixed on supporting materials (Nikazar *et al.*, 2007), to prevent contamination.

By supporting TiO<sub>2</sub> on electrospun nanofibres, with their large surface to volume ratio, the limitations of TiO<sub>2</sub> such as solution fouling, light scattering and loss of active surface can be eliminated (Woan *et al.*, 2009). This study is aimed at supplementing the electrospun fibres with TiO<sub>2</sub> nanoparticles by sol-gel doping with TiO<sub>2</sub> or thermal oxidation of titanium precursors onto the electrospun fibre surface in an attempt to support the catalyst and maintain the active surface area of the catalyst. In the interest of achieving the proposed objectives, the research focused on the synthesis of polymer nanofibres in composite form with an active photocatalytic phase.

PAN fibres are acrylic fibres with molecular formula [C<sub>3</sub>H<sub>3</sub>N]<sub>n</sub>. The functional groups can become the subject of radical interactions (Yusof and Ahmad, 2010). The oxidative stabilisation and carbonisation of electrospun polymer fibres are steps implemented to stabilise the fibres by eliminating the potential vulnerable functional groups. The post electrospinning steps are however energy consuming and complicated. The study also attempted to eliminate the thermal stabilisation steps used by Yusof and Ismail, (2012) after the electrospinning process.

### **1.3 Motivation and objectives**

The reported application of TiO<sub>2</sub> as photocatalyst for the removal of cyanide from water in 1977 stimulated meaningful interests in the environmental applications of photocatalysis. TiO<sub>2</sub> is ideal for this application due to its chemical stability. It is also inexpensive (Fujishima and Zhang, 2006). Over the past years various studies by Torimoto *et al.*, (1996); Gao *et al.*, (2007); Konganand *et al.*, (2007) to name but a few have shown that mounting TiO<sub>2</sub> onto structural supports significantly enhances the photocatalytic ability of TiO<sub>2</sub> nanoparticles. There have been few reports on the stability of the support materials, in specific nanofibres, when subjected to radical environments. More investigations are required into the

stability of the polymer nanofibres. This is because PAN is quite a robust polymer and the post electrospinning stabilisation steps might not be required. There have also been few reports on the different methods of fabricating photocatalytic nanofibres, to determine whether TiO<sub>2</sub> should be coated onto the surface of the fibre or whether it should be embedded in the fibre.

The aim of this study was to enrich electrospun fibres with the active mineral phase TiO<sub>2</sub> nanoparticles and to evaluate how well the fibres performed in the photocatalytic degradation of methylene blue (MB). The objectives of this study therefore are:

- i. To synthesize a sol-gel formulation viscous enough to allow for electrospinning of continuous fibres with the narrowest diameter
- ii. To electrospin nanofibres supplemented with TiO<sub>2</sub> nanoparticles
- iii. To coat commercial electrospun PAN fibres with TiO<sub>2</sub> using a drop coating and thermal oxidation method
- iv. To implement a more streamlined process by omitting both calcination and carbonisation steps in the production of functional TiO<sub>2</sub> containing polymer nanofibres
- v. To characterize the fibres made and gain insight into the morphology and composition of the fibres using XRD, FTIR, Raman, SEM and TEM
- vi. To study the TiO<sub>2</sub> containing fibre efficiencies in photocatalytic degradation of methylene blue (MB)

#### **1.4 Hypothesis**

H1: Supported TiO<sub>2</sub>, on or inside, the electrospun polymer or carbonised nanofibres for their use in photocatalytic degradation of organics eliminate the problems associated with free floating TiO<sub>2</sub> nanoparticles in particulate form

HO1: Supporting TiO<sub>2</sub> on the nanofibres still results in leaching of the catalyst

H2: The supported catalysts exhibit improved photocatalytic efficiency

HO2: Supporting the TiO<sub>2</sub> photocatalyst upon the PAN nanofibres negatively affected the photocatalytic efficiency of the catalyst

H3: The fibres display unimpaired stability

HO3: The composite fibres display poor stability due to free radical attack resulting in fibre degradation

## 1.5 Research Questions

1. Electrospun TiO<sub>2</sub> containing nanofibres or surface coating of electrospun TiO<sub>2</sub> nanofibres, which is more functional?
  - Are these fibres stable under the simulated photocatalytic conditions?
  - Do thermal treatment steps affect the fibre performance in any way?
2. Are there any improvements to the supported TiO<sub>2</sub> catalyst compared to the commercial particulate TiO<sub>2</sub> catalyst?
3. Do these TiO<sub>2</sub> nanofibres display any thermal stability?
4. Do these TiO<sub>2</sub> nanofibres display any chemical stability?
5. Can the omission of both calcination and carbonation steps still produce functional nanofibres?
6. Does the photocatalytic efficiency of the fibres improve by increasing TiO<sub>2</sub> catalyst loading?
7. Does the catalyst modification to the polymer fibre impart any additional stability to the fibre?

## 1.6 Research approach

In the interest of achieving the objectives, the research focused on the synthesis of composite TiO<sub>2</sub> containing PAN polymer nanofibres and investigated if it was possible to eliminate the thermal stabilisation steps after the electrospinning process. Polymer nanofibres served as structural support for nano TiO<sub>2</sub> photocatalysts. The schematic of the research approach is presented in Fig. 1.1.

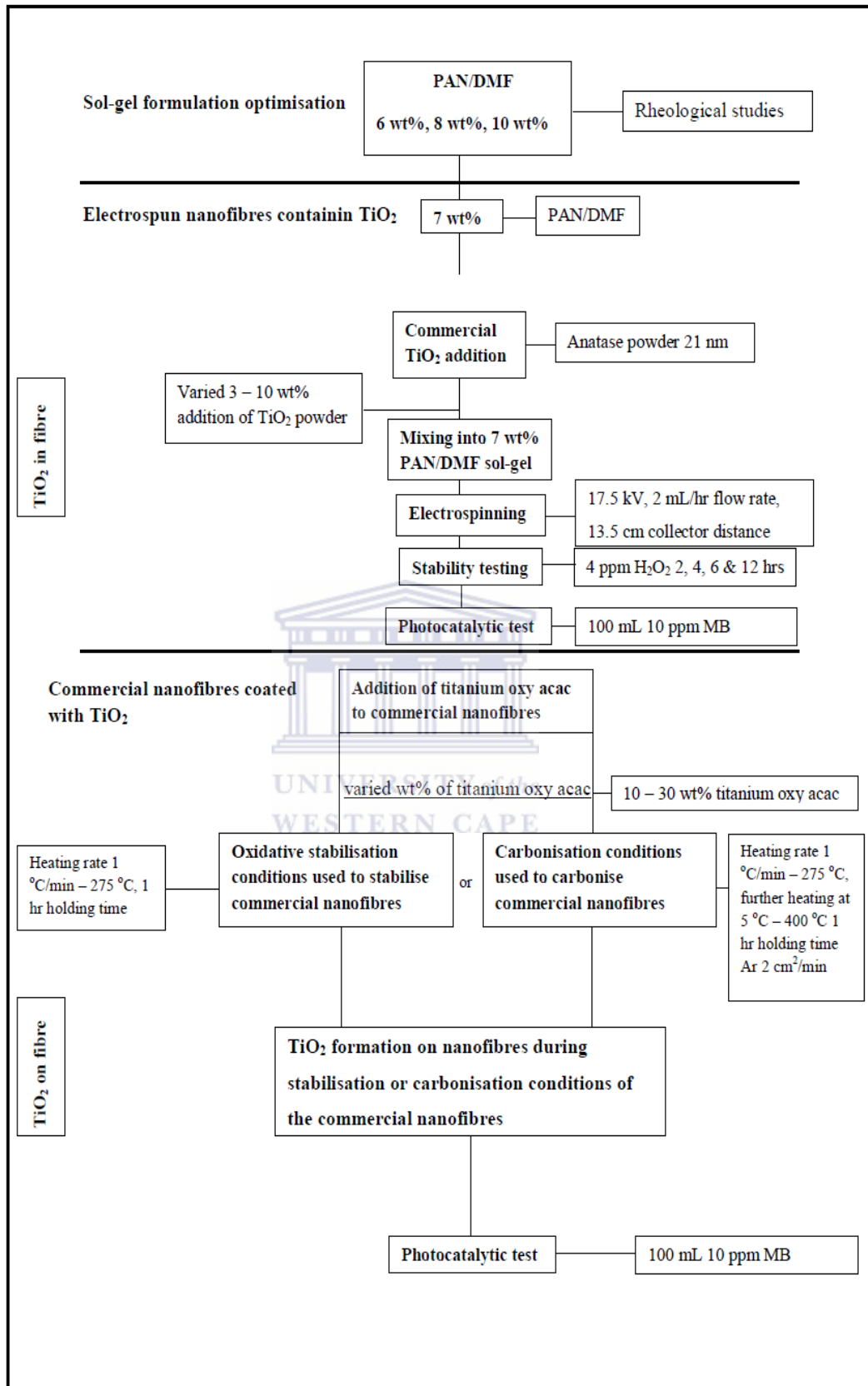


Figure 1.1: Schematic of research approach

To synthesize the PAN nanofibres, the PAN/DMF sol-gel formulation was first optimized to achieve the desired viscosity for electrospinning. Once the optimum polymer concentration and viscosity was determined the PAN/DMF sol-gel was loaded with commercial TiO<sub>2</sub> nanoparticles and electrospun.

On the other hand commercial electrospun PAN nanofibres were subjected to various thermal stabilisation processes to validate the necessity for the thermal steps and how it impacts the fibre stability. The fibres were coated with titanium oxy acetylacetonate and stabilised at 275 °C for 1 hour. The optimum loading was determined by varying the amount of titanium oxy acetylacetonate drop-coated upon the commercial PAN fibres. During the thermal stabilisation process of the commercial nanofibres the titanium oxy acetylacetonate decomposed to TiO<sub>2</sub> on the surface of the fibres. The commercial PAN nanofibres were also coated and carbonised using the same conditions as with the stabilised fibres except an additional heating step was added. The fibres were heated to 275 °C at 1 °C/min in air and the temperature was then ramped to 400 °C. The temperature was maintained at 400 °C for 1 hour. As previously stated, the optimum loading was determined by varying the titanium oxy acetylacetonate loading. The fibres were subjected to various characterization techniques. High Resolution Scanning Electron Microscopy (HRSEM) and Transmission Electron Microscopy (TEM) were used for the surface morphology investigations of the fibres. X-Ray Diffraction (XRD) was used for the identification of the crystal phases of TiO<sub>2</sub>, Raman spectroscopy and Fourier Transform Infrared (FTIR) spectroscopy were used to identify bonding interactions between TiO<sub>2</sub> and the fibre surface. Energy Dispersive Spectroscopy (EDS) was used to determine the average catalyst loading of the fibres.

All the prepared fibre samples were compared in the photocatalytic degradation of MB study to determine the photocatalytic activity of the composite fibres. The fibres were submerged in a 100 mL of an aqueous 10 ppm MB solution. The study was performed under UV light for 8 hours (UV illumination wavelength of 254 nm and 1.242 W/m<sup>2</sup> UV intensity).

## 1.7 Scope and delimitations of the thesis

This study investigated the electrospinning of polymer nanofibres for application as support structures for TiO<sub>2</sub>. No extended studies were performed on the impact of each parameter on the resultant fibre integrity. MB degradation is the standard method used to simulate organic pollutants and was used to assess and compare the photocatalytic potential of the TiO<sub>2</sub> containing polymer fibres, the TiO<sub>2</sub> coated stabilised fibres and the TiO<sub>2</sub> coated carbonised fibres by means of solution decolouration over time. Further manipulation of experimental conditions, doping of the fibres and metal ligand coordination to the surface of the catalyst for bandgap manipulation did not form part of the scope and was excluded from this study. It should also be mentioned that the objective of the study was to assess the efficacy of electrospun nanofibres only as catalyst support structures and influence on solution turbidity.

## 1.8 Thesis structure

This thesis is organised into 7 chapters and is structured as follows.

Chapter two presents the literature review which covers relevant aspects of electrospinning and TiO<sub>2</sub>. The different methods of nanofibre fabrication are also discussed. A review of advanced oxidation processes (AOP) is outlined where composite photocatalysts can be utilized.

Chapter three gives an account of the methodology, details of the actual methodology and experimental equipment as well as instruments used to characterise materials. The section also provides information about the materials and chemicals that were required in the synthesis steps and also gives an account of the photocatalytic study.

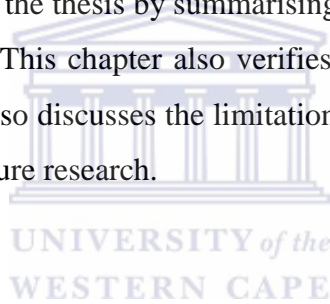
Chapter four describes the baseline characteristics of the PAN polymer sol-gel and electrospun fibres made using the methods described in chapter three. It is organized in manner to showcase the electrospinning parameters as well as the characteristics of the bare PAN polymer fibres. The section discusses the results

of the PAN polymer sol-gel rheology analysis and the findings of the optimum conditions for electrospinning of nanofibres are highlighted.

Chapter five presents the results and discussion of the PAN fibres modified with TiO<sub>2</sub> with relevant references to literature. The results are organized in a manner to showcase the deposition of the TiO<sub>2</sub> photocatalyst both inside and on top of the fibres, as well as the composite fibre characteristics. Significant findings are highlighted.

Chapter six presents the results of the photocatalytic activity of TiO<sub>2</sub>, TiO<sub>2</sub> containing PAN fibres, TiO<sub>2</sub> coated stabilised fibres and TiO<sub>2</sub>-coated carbonised fibres. The results are compared to literature and significant findings are highlighted.

Chapter seven concludes the thesis by summarising the findings and highlights the novelty of the research. This chapter also verifies the hypothesis of the research based on the results. It also discusses the limitations of the study as well as makes recommendations for future research.



## **Chapter 2**

### **2. Literature Review**

The following chapter is intended to give a brief introduction to electrospinning, polyacrylonitrile (PAN) nanofibres, AOP, and environmental catalysis. A brief introduction will be afforded to the polymer, polyacrylonitrile. Thereafter, an in depth discussion of advance oxidation processes, heterogeneous photocatalysis, and titanium dioxide (TiO<sub>2</sub>) will follow. This section will also describe various photocatalyst supports as well as some of the forerunners of titanium nanofibres. To conclude the review the applications of titanium nanofibres will be presented and a gap analysis given showing why this study was needed.

#### **2.1 Electrospinning**

Electrospinning is governed by a consortium of parameters that directly impact the outcome of the experiment. Therefore, it is necessary to discuss the effect of each parameter has on the electrospinning process. However, electrospinning only makes up part of the study and also nanofibre synthesis is not just restricted to electrostatic polymer drawing only. There has been substantial research devoted to the engineering of nanoscale materials by industry. One of the industries devoted to the cause is the fibre industry. Nanofibres display diameters of 100 nm or less, which is a feature that imparts unique characteristics to these fibres. Due to process limitations current fibre technologies have been unable to produce robust fibres smaller than 2 microns. Electrospinning is the most widely used for the fabrication of nanofibres. Extensive research has been conducted on the electrospinning process to increase the productivity. Research has seen several modifications to the electrospinning setup from single needle systems to multi needle multi jet systems. Section 2.1.1 discusses the basic principles of electrospinning and will give an overview of the single needle electrospinning process and the influential parameters associated with it.

### 2.1.1 Single needle electrospinning

Electrospinning is a technique that has been used for some time to produce fibres. In the late 1500s Sir William Gilbert described the behaviour of the known magnetic and electrostatic phenomenon when a charged piece of amber was brought near a droplet of water. What he observed was small water droplets being ejected from the tip of a cone when in close proximity to the amber. This was the first recorded observation of electrospraying (Stanger, 2009). Electrospinning is unique in that it uses electrostatic forces to produce fine fibres from a polymer solution that are thinner in diameter and have a larger surface area compared to conventionally spun fibres (Bhardwaj and Kundu, 2010).

The history of electrospinning is quite extensive. 1929 saw the first application of electrospinning and in 1934 the process went global. Anton Formhals had the idea to make synthetic nylon fibres from cellulose acetate that closely resembled silk. The first patent by Formhals using the electrospinning was issued in 1934 for the fabrication of textile yarns, the setup used 57 kV to electrospin cellulose acetate dissolved in acetone and monomethyl ether. A spinning collector drum type of device was used to collect the threads in a stretched position (Bhardwaj and Kundu, 2010).

There are two standard types of electrospinning setups, vertical and horizontal. The basic electrospinning setup has three major components, a high voltage power supply creating a potential difference between the spinneret and a grounded collector plate. In a basic electrospinning setup the spinneret containing the polymer sol-gel has an opposite charge to the collector plate. The potential difference between the two terminals gives rise to an electrostatic field. The high voltage source injects a charge into the melt which jets from the spinneret and collects on the charged collector plate. In electrospinning, the innate surface tension of the polymer holds the droplet at the tip of the capillary tube forming the Taylor cone. Once the repulsive electrical forces overcomes the surface tension forces, the critical value, the charged polymer jets from the Taylor cone in a chaotic fashion and collects on the grounded plate (Chew *et al.*, 2006).

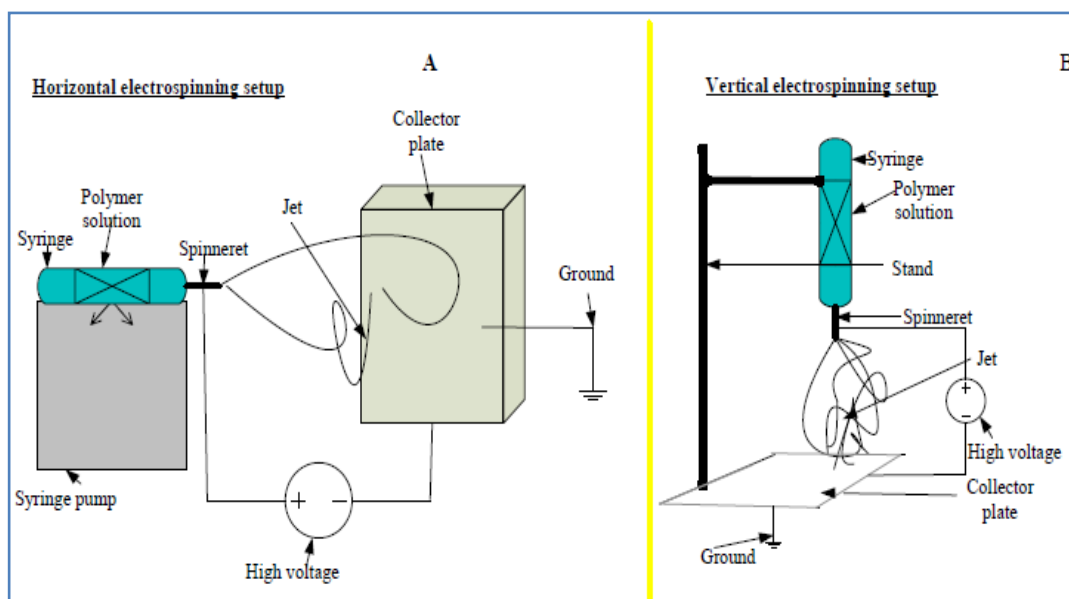


Figure 2.1: Schematic diagram of the two standard types of electrospinning setups (a) vertical setup and (b) Horizontal setup (Bhardwaj and Kundu, 2010)

Electrospinning can produce fibres within the submicron range as well as nano range with a wide range of polymers (Chong *et al.*, 2007). Electrospinning is governed by parameters that can be categorized into solution parameters, physical parameters and ambient parameters. The solution parameters can be subdivided into viscosity, concentration, molecular weight and surface tension. The physical parameters are tip to collector distance, applied electric field and flow rate. These parameters have a significant impact on the morphology of the fibres. By optimizing these parameters, nanofibres with the desired diameter and morphology can be synthesized (Bhardwaj and Kundu, 2010).

Electrospinning can be classified into confined and unconfined feed systems. In confined feed systems (CFS) the polymer melts are subjected to controlled feed rates whereas in unconfined systems (UFS) the polymer melts flow unconstrained over other materials (Nayak *et al.*, 2011). Figures 2.2-2.5 are schematic diagrams which illustrate various techniques used for nanofibre fabrications.

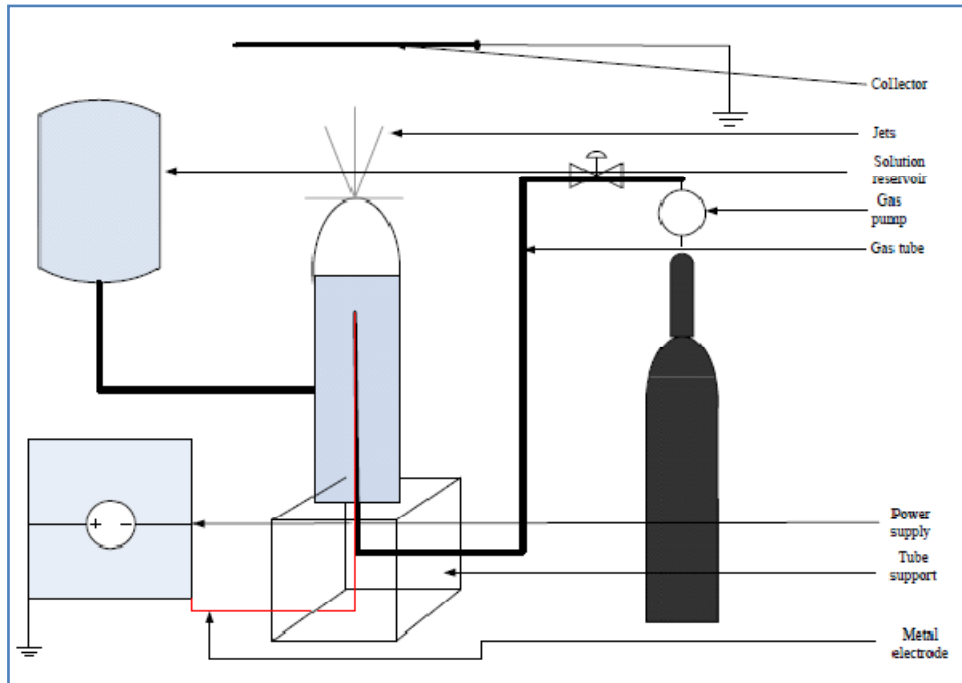


Figure 2.2: Schematic description of a bubble electrospinning setup (Yang *et al.*, 2009)

The bubble electrospinning setup is shown in Figure 2.2. In bubble electrospinning a bubble is made of a polymer solution under voltage. This particular technique can prepare nanofibres within the 50 nm range (Yang *et al.*, 2009).

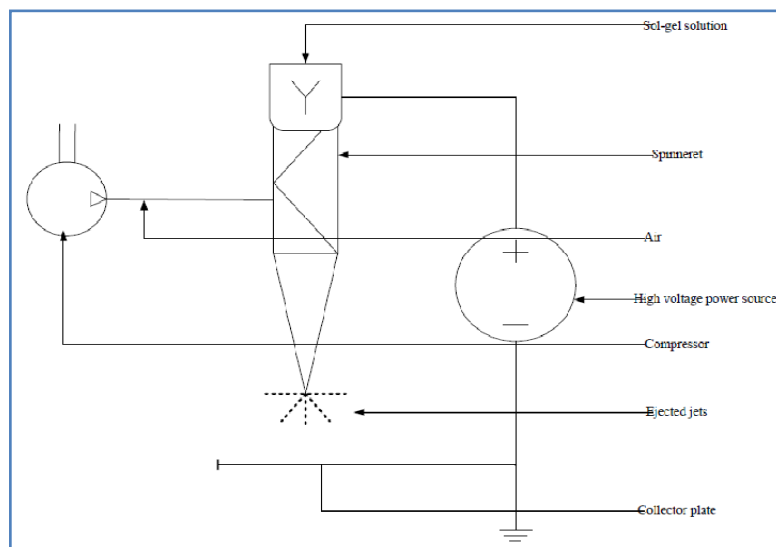


Figure 2.3: Schematic description of an electroblowing setup (Kong *et al.*, 2009)

Figure 2.3 shows a blowing-assisted electrospinning process where air blows around the spinneret. The blowing assists in overcoming the high surface tensions of the polymer solution and assists in solvent evaporation (Kong *et al.*, 2009).

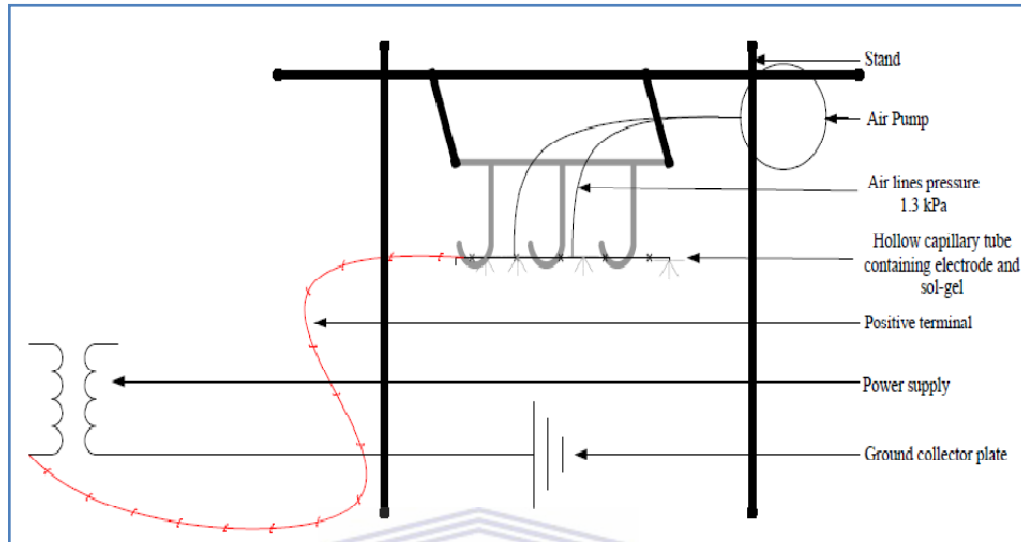


Figure 2.4: The framework of a porous hollow tube electrospinning setup (Varabhas *et al.*, 2008)

A porous hollow tube electrospinning setup can be seen in Figure 2.4. A wire mesh electrode is inserted inside the tube with the tips of the wires positioned inside the tube closest to the holes to maintain equal electrical potential at the drilled holes in the tube. The polymer solution passes under 1.3 kPa pressure through the wall of the capillary tube and emerges from the holes that are randomly distributed across the surface of the tube and collects as fibres on the grounded aluminium foil. This type of setup is an improvement on the conventional setup to improve the production rate (Varabhas *et al.*, 2008).

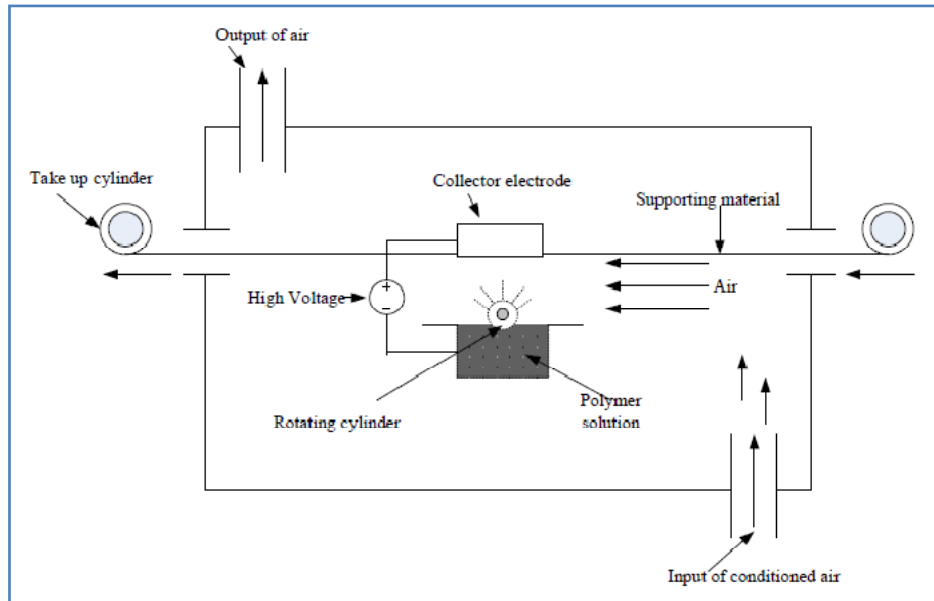


Figure 2.5: Schematic description of roller electrospinning (Nayak *et al.*, 2011)

Figure 2.5 illustrates a rotational electrospinning setup. A rotating cylinder is used to spin nanofibres by partially submerging the aluminium roller in the polymer solution contained in a polypropylene dish (Nayak *et al.*, 2011)

### 2.1.2 Electrospinning parameters

Electrospinning is governed by a range of various parameters and considering the complexity of the process it is difficult to isolate the influence of each parameter on the process. By virtue of theoretical modelling Thompson *et al.*, (2007) were able to identify the parameters that had the most considerable effects on the fibre diameters. The most influential parameters were volumetric charge density, tip-to-collector distance, initial jet radius which is linked to syringe diameter, relaxation time and elongation viscosity. The other parameters such as polymer concentration, density, electrical potential, perturbation frequency and solvent vapour pressure were found to moderately affect the fibre diameter. Relative humidity, surface tension and vapour diffusivity were considered trivial in their effects on fibre diameter (Thompson *et al.*, 2007).

Yordem *et al.*, (2008) investigated the effects of material and process parameters on the diameter of electrospun polyacrylonitrile fibres. The objective of the study was to investigate the electrospinning related material, process parameters,

solution concentration, applied voltage and collector distance. Both the individual and interactive effects of these parameters on the diameter of the electrospun PAN fibres were investigated within the context of response surface methodology. In their work a PAN polymer sol-gel was electrospun to produce nanofibres. Their study found the parameters to be interdependent on one another. The fibre diameter was also responsive to voltage but the effects were dependent on solution concentration and collector distance. They found the diameter to be unaffected by higher voltages at the collector distance at which the experiments were performed. For nano-scale fibre production the following parameters; concentration, collector distance and voltage were found by Yordem *et al.*, (2008) to be imperative in nano-scale fibre production. Although their study could not make precise predictions of nano-scale ranges it was useful in the determination of the parameter domains. Their data plots suggested voltage and concentration ranges of 10 - 20 kV and 8 – 10 wt% polymer concentrations respectively using polymers with molecular weights of about 75,000 g/mol.

Fridrikh *et al.*, (2003) proposed a model for the stretching of a viscous charged fluid in an electric field in a study to control the fibre diameter during electrospinning. By using polymers with known surface tension values they were able to construct a model that suggested the existence of a limiting diameter for the fluid jet during electrospinning. The model proposed the final diameter of the electrospun fibres to be a product of the resultant force between surface tension and electrostatic charge balance.

The molecular weight of the polymer is one of the major parameters in electrospinning. Not only does it affect the viscosity of the sol-gel but the conductivity as well and has a direct impact on the morphology of the fibres. Similar to polymer concentration, too low a viscosity results in bead formation whilst higher viscosities give thicker fibres (Koski *et al.*, 2004). However, for viscosity even at low polymer concentration the polymer solution must just be able to maintain sufficient entanglements of the chain to produce a uniform jet during electrospinning. As long as the intermolecular reactions on the polymer

can negate the effects of surface tension, high molecular weight polymers are not such a necessity (Tan *et al.*, 2005).

Yordem *et al.*, (2008) reported fibre diameter to be directly related to polymer concentration. For proper fibre formation to occur a minimum polymer concentration was required. Studies have shown that too low solution concentrations resulted in a mixture of fibre and bead formation but as the concentration increased more uniform fibres with increased diameters were formed (Yordem *et al.*, 2008). Solution concentration is a very important aspect of electrospinning. Several publications have shown concentration to be vital in fibre diameter. Lin *et al.*, (2005) investigated the effect of polymer concentration on surface morphology. Their aim was to assess bead formation at lower polymer concentrations. There are several methods that can be used to reduce fibre diameter, some of which include adjusting the parameters such as the applied potential and lowering the polymer concentrations. However, reports by Lin *et al.*, (2005) and He *et al.*, (2008) suggested reducing the fibre diameter by decreasing the polymer concentration to affect the uniformity of the fibres (Lin *et al.*, 2005). If the viscosity was too low it resulted in beads-on-string structures. As the droplet size became smaller, at lower polymer concentrations, the charge density increased on the surface of the polymer. However, in polymer chains with higher molecular weights this did not occur instead the jets did not break up but stabilized to form an array of beads connected by the fibre (Gu *et al.*, 2005). This was attributed to the lower charge density on the jet that facilitates the stretching of the filament into homogeneous fibres.

For lower polymer concentration sol-gels, beads-on-string formations can be prevented by simply adding a surfactant. The role of the surfactant is to lower the surface tension of the sol-gel and to facilitate the formation of homogeneous fibres. To monitor and assess the impact surfactants had on fibre morphologies Lin *et al.*, (2005) electrospun several sets of fibres from various polymer concentrations. Several sets of fibres were also electrospun with different concentrations containing the surfactant dodecyltrimethylammonium (DTAB). The electrospinning experiments were conducted under ambient temperature, a

1.5 kV/cm applied electrostatic field and 1 mL/hr flow rate. The fibre morphology of the spun fibres was observed under a scanning electron microscope. They found the fibre morphology to be inconsistent instead a series of beads and bead assemblages were present. As the concentration of the polymer increased the number of beads decreased and transformed to beads-on-string structures. This continued up till a 5 % (w/v) PAN/DMF concentration. Thereafter thicker homogenous fibres were observed. As the polymer concentration increased so did the fibre diameter. Polymer concentrations between 6 – 8 wt% delivered fibres with relatively narrow diameters. Gu *et al.*, (2005) found PAN concentrations lower than 6 wt% resulted in bead formation under the applied voltage. The addition of surfactant DTAB, as low as 5 mg/mL added to PAN polymer solutions, could bring about significant changes to the fibre morphologies. Lin *et al.*, (2005) found dilute PAN/DMF solutions up to 1 % (w/v) mixed with DTAB produced fibres with morphologies similar to pure PAN/DMF concentrations in the 2 – 5 wt% (w/v) range. Polymer concentration was reported by Van der Schueren *et al.*, (2011) to be the determining factor for the average electrospun fibre diameter. Although the beads-on-string was not eliminated the bead size was reduced considerably as well as the fibre diameter. Lin *et al.*, (2005) found the conductivity of the polymer solution to increase significantly when the surfactant was added. However, the conductivity of the PAN/DMF solution was found to decrease as the concentration of the polymer increased.

Viscosity is important when electrospinning fibres from a sol-gel. Solution viscosity is paramount as too low a viscosity impedes continuous fibre formation. When the viscosity is too high problems are encountered during melt ejection. Studies have found that optimum viscosities for electrospinning is polymer-specific, polymer solutions with very high viscosities exhibited longer stress relaxation times reducing fracturing of ejected jets. At lower viscosities below the critical concentration, surface tension dominates forming beads or beaded fibres (Bhardwaj and Kundu, 2010). A report by Lin *et al.*, (2005) also suggested too low a solution viscosity would result in beads-on-string structures.

Surface tension, the ability of a liquid to resist influences from an external force, is a function of polymer composition and reducing the surface tension of the sol-gel can lead to bead free fibres. As the polymer concentration of the sol-gel increases cohesive forces between the molecules increases as well. Generally high surface tension solutions impede electrospinning because of instability of the jets and generation of sprayed droplets (Hohman *et al.*, 2001). Surface tension of solutions regulates bead, droplet and fibre formation as well as the electrical potential required for electrospinning. In essence surface tension establishes the upper and lower boundaries of the electrospinning window provided other variables are kept constant (Zhang *et al.*, 2005).

Polymers are mostly conductive materials. The charged ions are highly influential in jet formation, excluding the few exceptions of dielectric materials. Solution conductivity is governed by the solvent used, polymer type and the availability of ionisable salts such as LiCl, NaNO<sub>3</sub>, CaCl<sub>2</sub> and NaCl (Qin and Wang, 2008). The general trend for smaller diameter fibres has been to use high solution conductivity, although highly conductive solutions became extremely unstable in the presence of strong electric fields. The addition of ionic salts has been reported to produce bead-less fibres with smaller diameters by enhancing the conductivity of the electrospinning solution (Bhardwaj and Kundu, 2010; Qin *et al.*, 2004)

### **2.1.3 Processing Parameters**

According to Jalili *et al.*, (2005) different polymers display different behaviour towards alteration of operating parameters. In a 15 wt% PAN/DMF solution the average diameter of the electrospun nanofibres decreased from 385 to 310 nm by increasing the applied voltage from 10 to 20 kV. At an applied voltage of 10 kV a flow rate of 2 mL/hr yielded uniform nanofibres. When a tip collector distance of 5 and 7.5 cm were applied the fibres were mostly wet; however, a tip collector distance of 15 cm yielded stabilised and dry nanofibre structures. The reviews of previous literature revealed the effect of electrospinning parameters on fibre morphology to be polymer specific. Zhang *et al.*, (2005) found the fibre diameter of electrospun polyvinyl alcohol fibres to decrease only slightly when the applied electrical potential was increased whilst the distribution of the fibre diameter

increased concurrently. Variation in tip-to-collector distance had no significant impact on the fibre morphology.

Applied voltage is probably the most crucial element in the electrospinning process. It is only when the threshold voltage is exceeded does the fibre formation occur. This current injection provides the necessary energy to overcome the critical forces to initiate electrospinning. Some researchers have reported that when higher voltage than required is applied to a melt it can increase polymer ejection, forming fibres with larger diameters. Other researchers again reported findings of higher voltages decreasing the fibre diameter of electrospun fibres. In most cases the higher voltages caused greater stretching of the fibres by increasing the electrostatic repulsive forces on the jet. These conflicting reports can be attributed to the different properties displayed by various polymers (Bhardwaj and Kundu, 2010). Gu *et al.*, (2005) were able to establish a relative parameter range for uniform PAN nanofibre formation. Their results proposed the optimum conditions to be a concentration range of 8 – 10 wt% and a voltage range of 10 – 20 kV, however, the voltage range had no significant impact on the fibre morphology (Gu *et al.*, 2005).

The flow rate of a polymer solution is a very important parameter as it influences jet velocity and facilitates solvent evaporation. If the flow rate is too high it can affect the morphological structure of the spun fibre increasing the fibre and pore diameter therefore it is important to establish the minimum flow rate of the spinning solution (Bhardwaj and Kundu 2010). Jalili *et al.*, (2005) reported flow rates of 2 mL/hr for a 15 wt% PAN/DMF solution over a tip collector distance of 15 cm with an applied voltage of 10 kV to yield stabilised nanofibre structures. Flow rates of 1 mL/hr and 4 mL/hr at an applied voltage of 10 kV yielded beaded nanofibres.

The tip-to-collector distance has been investigated as another approach to controlling fibre diameter and morphology. Although the tip-to-collector distance is considered not to be as significant as the other parameters, it is still important to establish a minimum distance that allows for effective drying of the fibres before reaching the collector. If the collector is too close to the tip, the possibility of bead

formation exists. Smaller polystyrene (PS) fibres have been spun at closer distances as long as the tip-to-collector distance is optimized to favour solvent evaporation (Bhardwaj and Kundu, 2010). For nano-scale fibre production tip-to-collector distance is one of the more influential parameters for nano-scale fibre fabrication. Collector distance was reported by Yordem *et al.*, (2008) to directly impact nano-scale fibre formation range, using PAN/DMF solutions with concentrations between 8 – 10 wt% and voltage ranges of 10 – 20 kV. Tip to collector distance was reported to affect the jet's behaviour as well. Tuck *et al.*, (2012) reported a change in the polymer jet whipping as the collector distance increased.

The selection of a proper solvent is an indispensable step in the electrospinning process as it is used in the polymer preparation and has a significant influence on the spinability of the melt. In a quest to find the ideal solvent, Wannatong *et al.*, (2004) studied the effect of various solvents on electrospun polystyrene fibres. In their study the effect of solvents on the productivity and morphology of PS fibres was investigated. Solvent scrutinizing was centred around establishing relationships between solvent properties and their impact on the fibre properties. Findings by Wannatong *et al.*, (2004) suggested the knowledge of the solvent properties eg. boiling point, density, solubility parameter, dipole moment and dielectric constant to be influential in the prediction of the outcome of the fibres. By simply increasing solvent boiling point and density using different solvents, *m*-Cresol and DMF, a decrease in the diameter of the electrospun polystyrene fibres was observed. The impact of solvent boiling point was found to be somewhat significant on fibre productivity (Fryczkowski *et al.*, 2013). Solvents with higher boiling points such as *m*-Cresol required higher electrospinning temperatures and increased polymer loading but had the highest productivity compared to dimethylformamide (DMF), tetrahydrofuran (THF) and toluene (Wannatong *et al.*, 2004).

Beads-on-string formation was observed when the variation in the solubility parameter and dielectric constant of polymer and solvent was too large. This could possibly be ascribed to retraction between the polystyrene molecules due to

poor interaction between polymer and solvent. Wannatong *et al.*, (2004) also found solvents with higher dielectric constants and dipole moments to enhance fibre productivity. By counting the electrospun fibres produced per minute per unit area Wannatong *et al.*, (2004) found the productivity of DMF and m-Cresol to be higher than the results for toluene and THF yielding denser mats. DMF and m-Cresol solvents gave the highest electrical susceptibility of the solutions when subjected to an electric field (Wannatong *et al.*, 2004). Changes in solvents can bring about improvements in solution conductivities which in turn can affect the jet elongation potentials (Liu *et al.*, 2011). Solvent properties such as dielectric constant and evaporation rate were also reported to be instrumental in determining the behaviour of solution jets during electrospinning (Eda *et al.*, 2007). Eda *et al.*, (2007) in their study of the jet evolution of PS with various solvents were able to investigate the jet evolution as it emerged from the capillary by using a high speed camera.

Hohman *et al.*, (2001) developed a qualitative method for predicting when electrospinning occurs. They found the chemical and physical parameters to be a function of viscosity and fluid conductivity. Their results showed whipping to be the essence of electrospinning. Fluid whipping was found to be initiated by instability in the fibre spin-line when the charge on the jet interacted with the external field resulting in fibre whipping and stretching into the nano region (Hohman *et al.*, 2001).

Electrospinning can be quite a complex process in spite of its simplistic principle. Electrospinning is plagued by influences that directly affect the morphology of the electrospun fibres. The phenomenological relationship to fibre diameter has been polymer concentration, viscosity, conductivity, surface tension and dielectric constant of the polymer solution (Costolo *et al.*, 2008). By using a simulator, Costolo *et al.*, (2008) were able to study the effects of physical parameters and chemical composition on the electrospun fibre diameter. Their work stipulated the importance of relative humidity and ambient temperature control in creating fibres that were in the sub 25 nm domains. In dry ambient air, (relative humidity = 14 %), they were unable to electrospin using identical formulations and conditions.

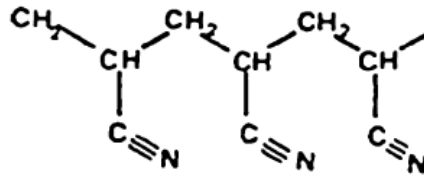
Ambient humidity affected the fibres. This is due to moisture absorption in the sol-gel, which either enhanced the conductivity or affected the fibre formation ability.

Humidity has been found to be quite influential in the formation of nano diameter electrospun fibres. Higher sol-gel temperatures are known to generate thinner fibres due to decreased viscosity but there appears to be a lack of research on the effect of surrounding temperatures on electrospun fibres (De Vrieze *et al.*, 2009). In order to determine the effect of temperature and humidity on electrospun fibres, De Vrieze *et al.*, (2009) electrospun both cellulose acetate and polyvinylpyrrolidone (PVP) in a humidity and temperature controlled environment. The effect of temperature on the fibre diameter was determined at 283 K, 293 K and 303 K. The experiments to determine the effect of RH on fibre diameter were performed at RH 30 %, RH 45 % and RH 60 %. At higher humidity water absorption was much easier which resulted in the formation of a film of transparent fibres on the collector. The presence of the excess water inhibited adequate drying of the jet to occur. At lower temperatures the time of flight distance did not allow for proper fibre formation. Higher humidity retarded solidification of the fibre jet and allowed elongation of the fibres to continue for longer resulting in thinner fibres. The effect of temperature was reported as follows: Lower temperature decreased the rate of solvent evaporation, exponentially increasing the solidification time; at higher temperatures the rigidity of the polymer chain changed, the lower solution viscosity produced a higher stretching rate.

## **2.2 Polyacrylonitrile**

Polyacrylonitrile (PAN) is a polymer that exhibits good stability and mechanical properties and has been widely used in the production of carbon nanofibres. PAN is a form of acrylic fibre with a chain of carbons connected to each other (see Figure 2.6). It is a synthetic semicrystalline polymer and has demonstrated superior performance in membrane applications and has also been established to be the best precursor for the production of high performance carbon fibres (Rahaman *et al.*, 2007; Scharnag and Buschatz, 2001). The polymer is hard,

relatively insoluble and has a high melting point. Due to its high melting point (317 °C) and carbon yield (56 %) PAN is used for the production of high performance carbon fibres (Rahaman *et al.*, 2007).



**Polyacrylonitrile**

Figure 2.6: Molecular structure of PAN (Rahaman *et al.*, 2007)

To produce polyacrylonitrile based carbon nanofibres the PAN polymer needs to be electrospun into fibres. To produce the nanofibres the PAN has to be dissolved in a solvent and electrospun. PAN is soluble in polar solvents like dimethyl sulfoxide (DMSO), DMF, dimethylacetamide (DMAc), dimethylsulfone, tetramethylsulfide and aqueous solutions of ethylene carbonate. PAN has the highest solubility in DMF (Nataraj *et al.*, 2012). To electrospin nanofibre precursors, Costolo *et al.*, (2008) modeled a series of solution properties and process parameters that they used in their study to electrospin PAN nanofibres with fibre diameters in the range of 25 – 100 nm (see Table 2.1) .

Table 2.1: Solution properties for process parameters for PAN nanofibre fabrication (Costolo *et al.*, 2008)

<b>Property</b>	<b>Range</b>
<b>Solution Properties</b>	
PAN wt%	1.5 - 6.25 wt%
Viscosity	12 - 117 cP
Conductivity	3.9 – 1149 $\mu\text{S cm}^{-1}$
Surface tension	27.3 - 37.1 $\text{mN m}^{-1}$
<b>Electrospinning conditions</b>	
Ambient relative humidity	22.0 - 61.7 %
Ambient room temperature	21.9 - 25.1 $^{\circ}\text{C}$
Flow rate	0.1 - 9.0 mL/hr
Applied Voltage	4.0 - 30.0 kV
Tip collector distance	5.0 - 11.0 cm
Applied electric field	0.8 - 5.5 kV/cm

Costolo *et al.*, (2008) used a vertical electrospinning setup in their study to electrospin PAN polymer fibres with average fibre diameters that ranged from 10 – 320 nm.

The second step in the transformation of PAN precursor fibres into carbon nanofibres involves the oxidative stabilisation of the polymer nanofibres. During this step the polymer is converted into a more stable ladder structure where the nitrile groups are converted to C=N bonds and crosslinks are developed between the PAN molecules (Rahaman *et al.*, 2007; Farsani *et al.*, 2007). Figure 2.7 illustrates the two important reactions that occur during stabilisation.

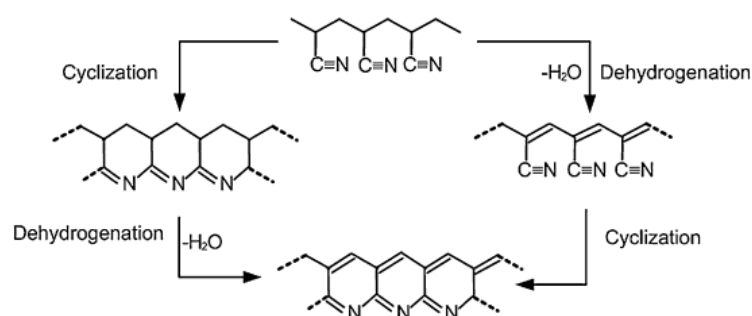


Figure 2.7: Cyclisation and dehydrogenation of PAN polymer during stabilisation (Rahaman *et al.*, 2007)

During the dehydrogenation step double bonds form that stabilise the carbon chain and during cyclisation the rings are formed. Cyclisation is the most important reaction in the stabilisation process. The nitrile groups react with adjacent groups to form a stable ladder polymer (Yusof and Ismail, 2012). Farsani *et al.*, (2007) reported that by modifying the stabilisation procedures of commercial PAN nanofibres it was possible to synthesize carbon fibres with modified chemical compositions. In their study commercial PAN fibres were converted into carbon fibres in two stages. Stabilisation of the fibres was performed at temperatures ranging from 180 – 270 °C in air; different thermal cycles were used for the stabilisation process. Their study found that when manipulating the stabilisation procedures the fibres stabilised more completely and produced carbon fibres with desirable tensile strength. The fibres also carbonised at higher temperatures during the carbonisation cycle (Farsani *et al.*, 2007).

Zhang *et al.*, (2007) investigated the effect of solution concentration and applied voltage on the morphology and sizes of nanofibres. PAN/DMF polymer solutions with concentration of 8 wt%, 10 wt% and 12 wt% were used to electrospin nanofibres. The applied voltages at which the fibres were electrospun were 10, 15 and 20 kV. The electrospun fibres were stabilised by heating the fibres from room temperature at a heating rate of 1 °C/min to heating temperatures of 250, 280, 300 and 310 °C respectively. Figure 2.8 shows the FTIR spectra of the nanofibres at different heating temperatures.

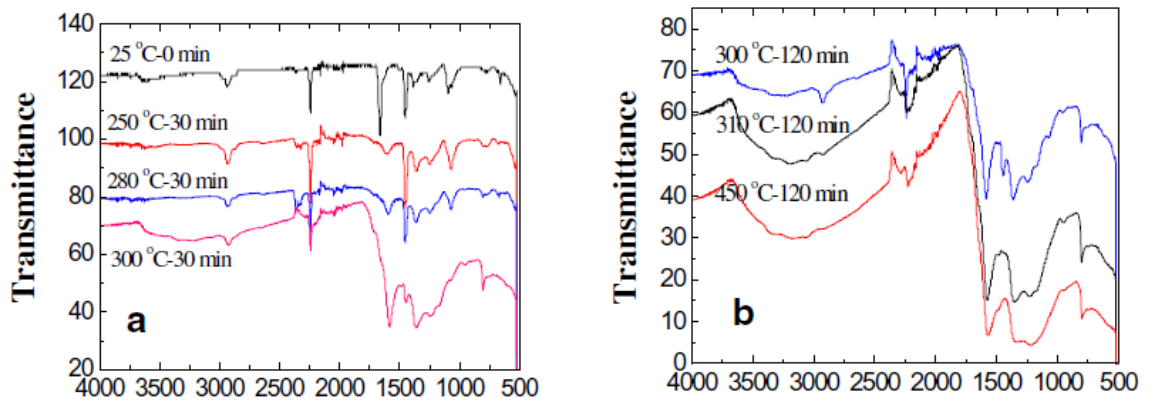


Figure 2.8: FTIR spectra of PAN fibres at different heating temperatures (Zhang *et al.*, 2007)

The major changes that occurred as the heating temperatures increased were the decrease in the intensity of the nitrile groups ( $2243 - 2241 \text{ cm}^{-1}$ ) and the aliphatic CH groups ( $1270 - 1220 \text{ cm}^{-1}$ ). Figure 2.9 shows the Raman spectra of the nanofibres at different heating temperatures.

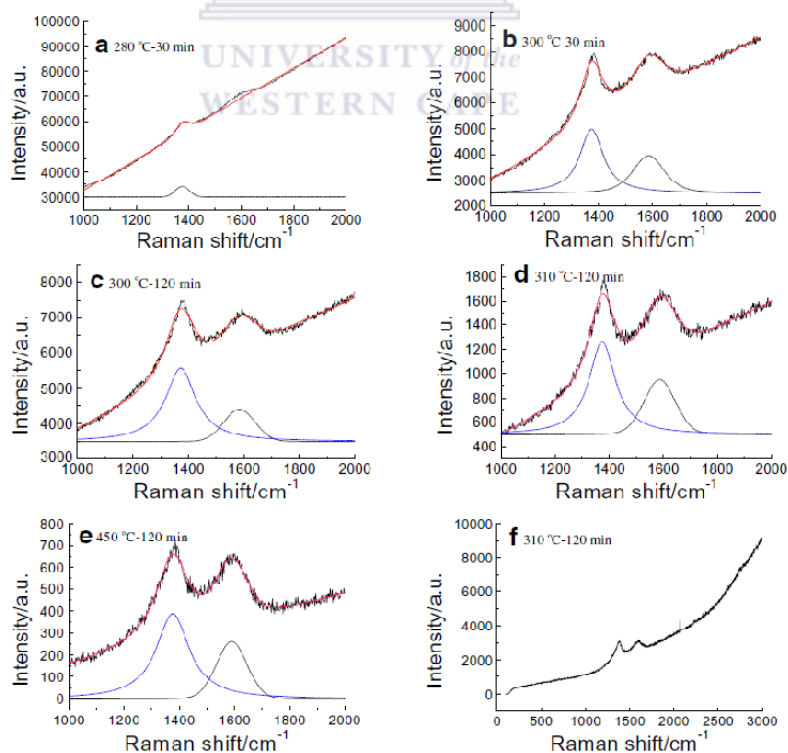


Figure 2.9: Raman spectra of the nanofibres at different heating temperature times (Zhang *et al.*, 2007)

The Raman spectra showed the characteristic D and G bands of carbon materials at  $1370$  and  $1580\text{ cm}^{-1}$  to become more predominant as the heating temperatures increased. The spectrum on the left in Figure 2.10 shows the XRD spectra of pure PAN and its stabilised fibres and on the right the carbonised fibres.

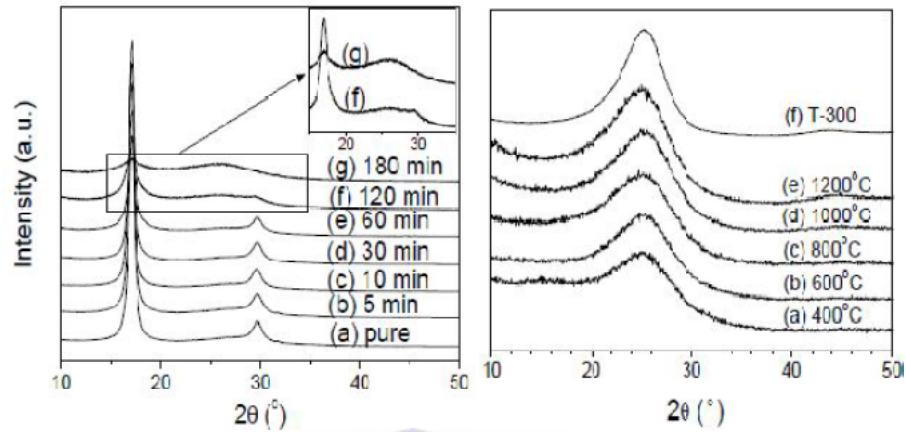


Figure 2.10: XRD spectra of PAN fibres, stabilised fibres (left) and carbonised fibres (right) (Lee *et al.*, 2012)

For the XRD spectra of pure PAN fibres a peak appeared at  $17^{\circ} 2\theta$  that was ascribed to the (100) plane of a hexagonal structure. Another peak was observed at  $29.3^{\circ} 2\theta$ . As the stabilisation time increased the intensities of the peaks became lower which was ascribed to the disruption and orientation of the crystalline structure. For the carbonised fibres the peak associated with pure PAN disappeared with all the carbonised fibres. The peak at  $25.5^{\circ}$  was ascribed to the (002) planes of the pre-graphitic structure. From the spectra it is clear that the heat treatment has a significant impact on the PAN structure (Lee *et al.*, 2012).

### 2.3 Advanced Oxidation Processes

The past decade has seen a lot of research devoted to environmental protection and regulations have been more stringently applied. These regulations are especially aimed at substances exerting toxic effects on the biosphere. The conventional technologies assigned to the removal of these pollutants and some harmful biological compounds consisted mainly of phase separation techniques and methods that destroy chemical contaminants. The chemical degradation methods are highly effective in their application when properly developed.

Chemical oxidation, which is a process that forms part of the methods that destroy contaminants, aims at mineralization of the compounds to CO<sub>2</sub>, water and inorganics so that contaminants can be easily degraded to harmless products. Frequently, pollutants exist that display exceptional chemical stability and are very difficult to completely mineralize. Prompted by this challenge, researchers developed a special class of oxidation techniques defined as advanced oxidation techniques.

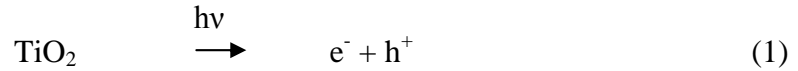
Andreozzi *et al.*, (1999) did a survey on the different advanced oxidation processes (AOP) and found these processes to be powerful in the degradation of refractory and toxic pollutants. Although these processes make use of different reacting systems they are characterized by the production of OH radicals. These radicals are highly reactive species and can attack most parts of the organic molecules quite rapidly.

Munoz *et al.*, (2005) performed a comparative assessment on the different AOPs. Two energy scenarios, solar electricity and solar energy were utilized to perform a life cycle assessment to quantify the environmental impacts of the AOPs. The treatment techniques used in the assessment were heterogeneous photocatalysis, photo-Fenton reactions, coupling of heterogeneous photocatalysis and photo-Fenton. To assess the AOPs from an environmental perspective the AOPs driven by two different energy sources, i.e. direct solar energy and electricity, were compared using a life cycle assessment (LCA). In the solar energy scenario, the environmental impacts of AOPs were drastically reduced due to the avoidance of electricity. The environmental impact was reduced by more than 90 %. In their studies heterogeneous photocatalysis and photo-Fenton processes appeared to be the best alternatives.

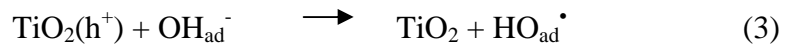
### **2.3.1 Heterogeneous photocatalysis**

This is an AOP that uses semiconductor metal oxides as catalysts and oxygen as oxidizing agent. In photocatalysis, the process is initiated by absorption of photon energy upon solar irradiation of the catalyst surface.

The dose of energy causes the formation of an electron-hole pair where the valence band electron is excited to the conduction band (Eq. 1).



The electron has a very high reducing power that enables it to reduce some metals and dissolved oxygen to form a superoxide radical. The remaining hole is capable of oxidizing adsorbed  $\text{H}_2\text{O}$  and  $\text{OH}^-$  to highly reactive OH radicals (Eq. 2 and 3).



These reactions and products are very important in oxidative degradation processes (Fujishima *et al.*, 2007). The quantum yield of this process is however crippled by the electron-hole recombination rate (Andreozzi *et al.*, 1999).

Herrmann, (1999) in a review on heterogeneous photocatalysis discussed the fundamental principles of photocatalysis and went on to describe the effects of the major parameters on the reaction kinetics. Heterogeneous photocatalysis was found to consist of five steps.

- Transfer of reactants in fluid phase to the surface
- Adsorption of at least one of the reactants
- Reaction in the adsorbed phase
- Desorption of the products
- Removal of product from the interface region

The reactions associated with heterogeneous photocatalysis have been reported to occur in the third step (see Eq. 3). The only difference in heterogeneous photocatalysis to conventional systems was ascribed to the form of activation energy. In heterogeneous photocatalysis thermal energy was replaced by photonic energy.

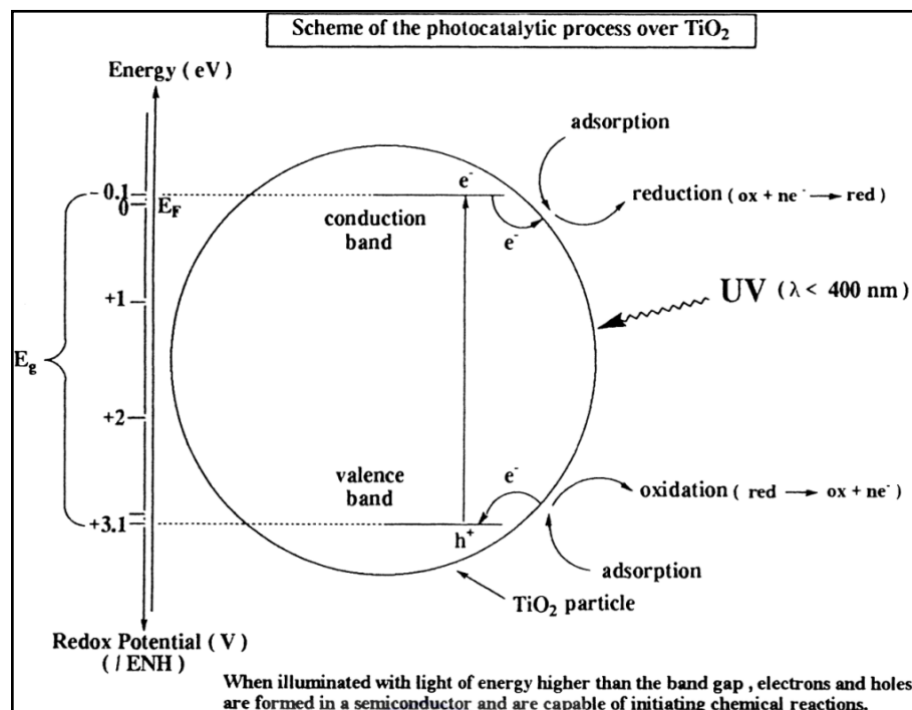


Figure 2.11: An energy band gap diagram of  $\text{TiO}_2$  (Herrmann, 1999)

Figure 2.11 depicts the photocatalytic process over a  $\text{TiO}_2$  catalyst. When a catalyst is illuminated by photons and the energy of the incident light is equal or greater than the band gap energy,  $h\nu \geq E_g$ , photons are absorbed. The absorption of photons creates electron-hole pairs forming photoelectrons in the conduction band and photoholes in the valence band (Herrmann, 1999). Photocatalytic reactions occur mainly at or close to the illuminated surface of the photocatalyst. However, recent studies have shown that photocatalytic reactions can also occur at distances from the catalytic surface through diffusion of the reactive species on the surface (Fujishima *et al.*, 2007).

### 2.3.2 The Fenton process

This is an old classic reaction (Eq. 4), it involves the addition of  $\text{H}_2\text{O}_2$  to  $\text{Fe}^{2+}$  salts to destroy toxins like phenols and herbicides.



This process is very attractive considering the availability of iron and the safety of both iron and hydrogen peroxide. However, in spite of being a very simple way of

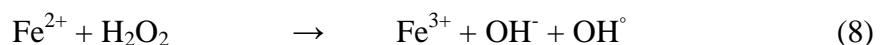
generating OH radicals the system is vulnerable to strict pH control. The photoassisted Fenton process, an extension of the Fenton process that also makes use of UV-Vis light to accelerate the rate of degradation of organic pollutants has not had success in industrial applications. This is due to the strict pH control requirements of the Fenton process and possibility of sludge formation. UV-VIS/ Ferrioxalate/H<sub>2</sub>O<sub>2</sub> is another oxalate system for the removal of organic pollutants. This system is more efficient than the Fenton processes as it has a broader photoactive region as well as a higher quantum yield and is more efficient (Andreozzi *et al.*, 1999).

### 2.3.3 Electrochemical methods

Electrochemical methods have been applied to remove organic pollutants from wastewater. A study by Godini *et al.*, (2013) investigated the efficiency of anodic oxidation (AO) and electro-Fenton (EF) processes on waste sludge treatment. In AO processes, organic matter is either oxidized directly on metal oxides or by adsorbed OH radicals. The mechanism for the process is given in Equations 5-7.



In EF OH<sup>°</sup> is generated from hydrogen peroxide catalysed ferrous ion



The results indicated that either AO or EF can be used to remove waste water sludge. Despite AO displaying more efficiency both AO and EF processes rendered similar deliverables (Godini *et al.*, 2013).

## 2.4 Environmental catalysis

A review by Manuel and da Silva, (2009) on the development of suitable materials on the nanoscale for macro-scale application highlighted some key steps

involved in environmental catalysis engineering. Their review found catalyst activity to be dependent on operating parameters such as catalyst loading, pH and substrate concentration in AOPs. They found other parameters to be process specific. For example, ozonolysis is pH specific, variation in pH was accompanied by changes in the order of the pollutant degradation reactions by molecular ozone. Photocatalysis was dependent on light intensity. The reaction rate regarding photocatalysis was reported by Manuel and da Silva (2009) to be proportional to radiant flux and mass of catalyst. However, catalyst loading was found to be regulated by particle illumination where scattering effects can impact the process efficiency. Photocatalyst composition was reported to also be process specific. For photocatalysis, adequate illumination of the catalyst is paramount and powdered catalyst was found most suitable. To eliminate additional filtration steps and to ensure catalyst integrity it was suggested that photocatalysts should be immobilized on support materials (Manuel and da Silva, 2009).

The degradation of MB in contact with a catalyst is internationally considered a standard method used for solutions in contact with a photocatalyst to measure the performance of the photocatalytic coatings. Tschirch *et al.*, (2008) investigated the photocatalytic bleaching of MB and went on to discuss the reaction mechanisms and some shortcomings of the method. From their results they were able to ascribe a protocol for this method to address vital junctions. MB did not only adsorb onto the catalyst surface but onto any medium in contact with the aqueous solution. Photolysis of MB was stagnant at wavelengths that were in the range of 350- 480 nm, wavelengths above or below this range initiated photolysis of MB. For specific photoactive surfaces, the system displayed zero-order kinetics below a specific maximum irradiation energy. Increased illumination did not enhance photolysis, however, the rate of reaction was influenced by the diffusion controlled transport of MB (Tschirch *et al.*, 2008)

#### **2.4.1 Titanium Dioxide (TiO<sub>2</sub>)**

TiO<sub>2</sub> occurs primarily in minerals like rutile, anatase, brookite, ilmenite, leucosene and a few other minerals. TiO<sub>2</sub> is also found in coal, ash, plants and even the human body (Carp *et al.*, 2004). TiO<sub>2</sub> has emerged as one of the most

excellent photocatalytic materials for environmental purification ever since the discovery of its ability to split water.  $\text{TiO}_2$  is highly chemically stable and produces highly oxidizing species, it is almost the ideal photocatalyst.  $\text{TiO}_2$  was first used for photo-electrochemical solar energy conversion, then the shift was to photo-induced photocatalysis and superhydrophilicity (see Fig. 2.12) to current  $\text{TiO}_2$  based commercialised products (Fujishima and Zhang, 2006).

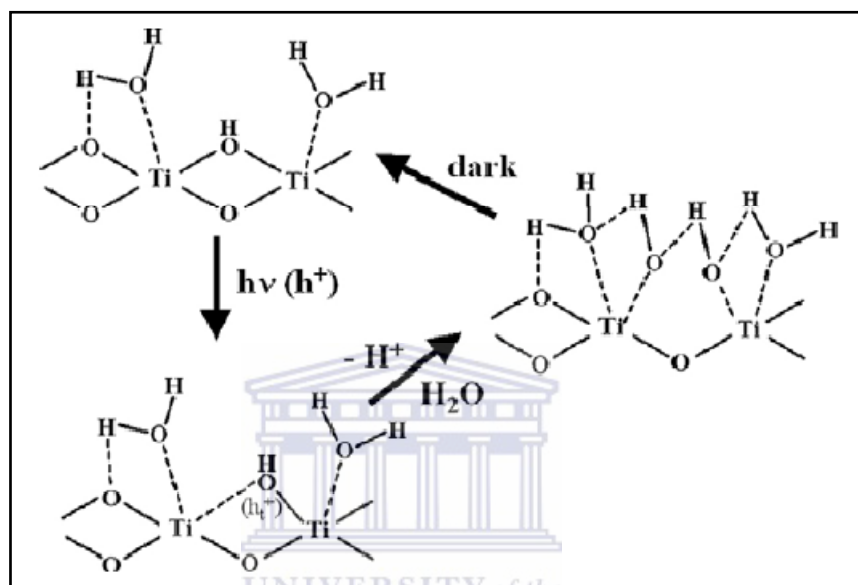


Figure 2.12: The mechanism for photo-induced superhydrophilicity on  $\text{TiO}_2$  surfaces (Fujishima and Zhang, 2006)

In Figure 2.12 photoexcited electrons are captured by molecular oxygen, while the holes diffuse to the  $\text{TiO}_2$  surface, being trapped at the lattice oxygen atoms. This trapping of the holes weakens the binding between the Ti atom and lattice oxygen. A water molecule then breaks the bond to form new hydroxyl groups. In the dark the hydroxyl groups desorb from the Ti surface in the form of  $\text{H}_2\text{O}_2$  or  $\text{H}_2\text{O} + \text{O}_2$ . One of the major drawbacks of  $\text{TiO}_2$  is the activation energy required as this catalyst is only active in the UV region. Much effort has been devoted to overcoming this obstacle (Fujishima and Zhang, 2006).

Semiconductors can be activated by light exhibiting higher energy than the energy with which electron hole-pairs are formed. The energy of photo-induced processes can be used electrically, chemically or even to change the catalyst surface. Many

chalcogenides semiconductors such as TiO<sub>2</sub>, ZnO, ZrO<sub>2</sub>, CdS, MoS<sub>2</sub>, Fe<sub>2</sub>O<sub>3</sub> and WO<sub>3</sub> have been examined but the anatase form of titania produces the best photoactivity and photostability. The transfer of electrons that occur over the semiconductor photocatalysts depends on the band-edge position of the semiconductor and the redox potentials of the adsorbents (Gaya *et al.*, 2008). What this means is that the activation energy is required for the valence band electron of the semiconductor to be excited to the conduction band (Matsumoto, 1996). The elementary reactions for degradation of organic compounds over TiO<sub>2</sub> surface have been reported repeatedly in literature.

Table 2.2 outlines the primary processes involved in the photocatalytic mineralization of organic compounds by TiO<sub>2</sub> and the time domain for each step.

Table 2.2: The primary processes and time domains in the mineralization of organic compounds by TiO<sub>2</sub> (Gaya *et al.*, 2008)

<b>Photocatalytic mineralization of organic compounds</b>	
<b>Primary process</b>	<b>Characteristic time</b>
Charge carrier generation	
$\text{TiO}_2 + h\nu \rightarrow e^- + h^+$	fs (very fast)
<b>Charge carrier trapping</b>	
$h^+ + >\text{Ti}^{\text{IV}}\text{OH} \rightarrow \{>\text{Ti}^{\text{IV}}\text{OH}^{\bullet+}\}$	10 ns (fast)
$e^- + >\text{Ti}^{\text{IV}}\text{OH} \leftrightarrow >\{\text{TiOH}^{\text{III}}\}$	100 ps (shallow trap; dynamic eq <sup>m</sup> )
$e^- + >\text{Ti}^{\text{IV}} \leftrightarrow \text{Ti}^{\text{III}}$	10 ns (deep trap)
<b>Charge carrier recombination</b>	
$e^- + \{\text{Ti}^{\text{IV}}\text{OH}^{\bullet+}\} \rightarrow \text{Ti}^{\text{IV}}\text{OH}$	100 ns (slow)
$h^+ + >\text{Ti}^{\text{III}}\text{OH} \rightarrow \text{Ti}^{\text{IV}}\text{OH}$	100 ns (fast)
<b>Interfacial charge transfer</b>	
$\{>\text{Ti}^{\text{IV}}\text{OH}^{\bullet+}\} + \text{organic molecule} \rightarrow >\text{Ti}^{\text{IV}}\text{OH} + \text{oxidized molecule}$	100 ns (slow)
$\{\text{Ti}^{\text{III}}\text{OH}\} + \text{O}_2 \rightarrow >\text{Ti}^{\text{IV}}\text{OH} + \text{O}_2^{\bullet-}$	ms (very slow)

A conceptual diagram of the mineralization of organic compounds by  $\text{TiO}_2$  is shown below in Figure 2.13.

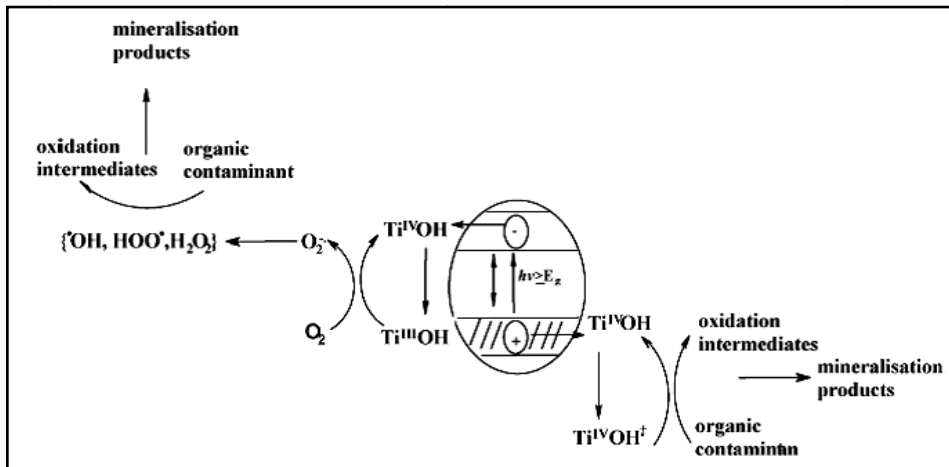


Figure 2.13: Primary process involved in mineralization of organic compounds (Gaya *et al.*, 2008)

Depending on the value of the Gibbs free energy reaction, a semiconductor reaction can either be an example of photocatalysis or photosynthesis. For an efficient semiconductor induced photocatalytic reaction the interfacial electron processes must effectively compete with the deactivation process and the electron hole-pair formation ( $e^-$ ,  $h^+$ ) must compete with the recombination processes. Both anatase and rutile are used as photocatalyst, anatase having the more superior photocatalytic activity (Carp *et al.*, 2004). Figure 2.14 below depicts the crystalline structures of  $\text{TiO}_2$

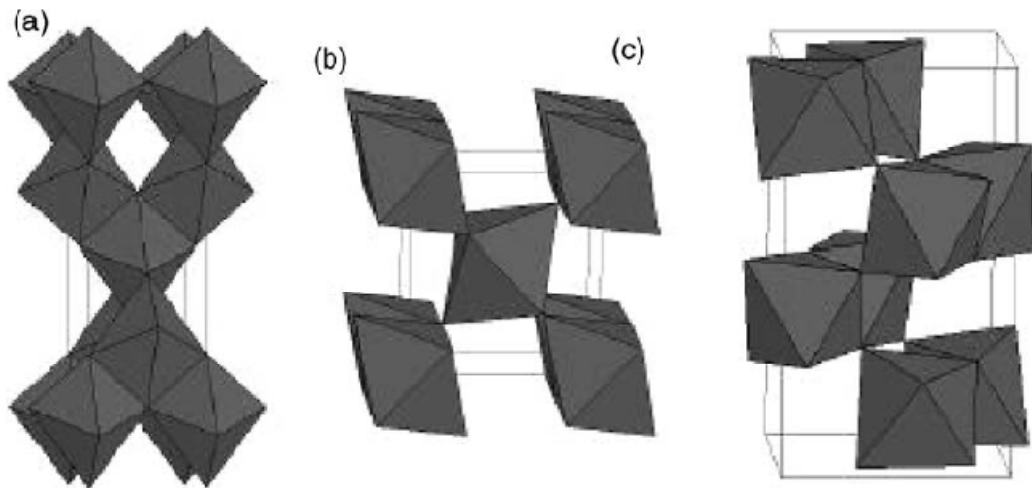


Figure 2.14: The crystalline structures of (a) anatase, (b) rutile and (c) brookite (Carp *et al.*, 2004)

The properties of titania are largely determined by its crystal phases anatase (tetragonal), brookite (orthorhombic) and rutile (tetragonal). There are many methods for preparing  $\text{TiO}_2$  nanoparticles for instance sol-gel method, chemical and physical vapour deposition, hydrolysis and colloidal chemistry methods. In many of these methods the resultant materials are in the amorphous phase and require thermal annealing to induce nanocrystalline phase formation.  $\text{TiO}_2$  phase formation is influenced by the method used. When preparing  $\text{TiO}_2$  using hydrolysis anatase to rutile phase transitions starts at  $600\text{ }^\circ\text{C}$  while phase transition using the sol-gel method only starts at  $800\text{ }^\circ\text{C}$ . Kholmanov *et al.*, (2003) produced nanostructured  $\text{TiO}_2$  thin films by supersonic cluster beam deposition. The titania clusters were produced by a pulsed microplasma cluster source (PMCS). The process involved sputtering of a titanium rod by helium plasma ignited with a pulsed electric discharge. After each pulse the removed material inside the source condensed to form clusters. The inert-gas and cluster mixture exited the source through a nozzle and collected on a substrate at room temperature. The samples were collected on a silicon substrate and were annealed for 4 hours at  $400$ ,  $600$  and  $800\text{ }^\circ\text{C}$ . They found that anatase nanocrystallites grew up to a crystal size where further growth was energetically unfavourable whereafter anatase transforms to rutile phase. Based on their findings they concluded that size-dependant effects in grain growth kinetics affect the morphology of

nanostructured TiO<sub>2</sub> thin films (Kholmanov *et al.*, 2003). Figure 2.15 shows the XRD spectra of the deposited nanostructured TiO<sub>2</sub> thin films

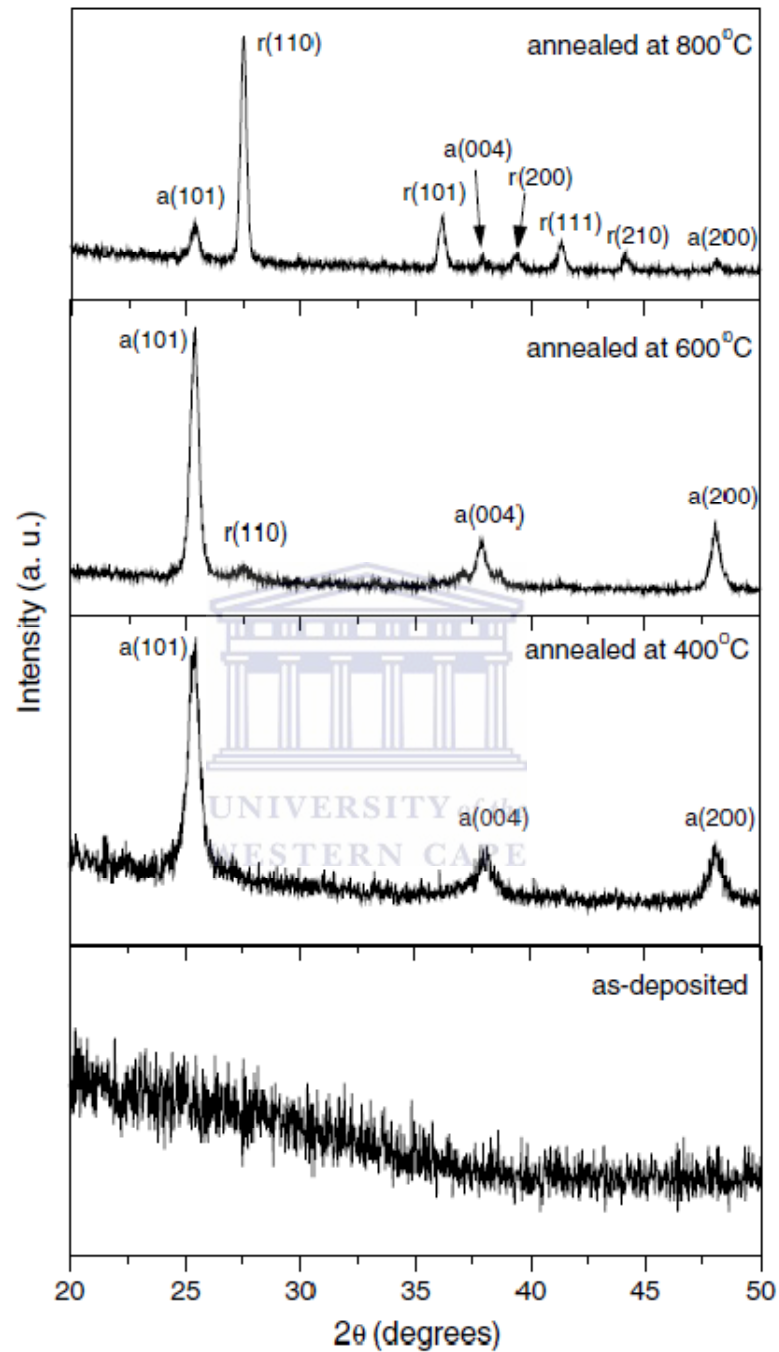


Figure 2.15: XRD spectra of nanostructured TiO<sub>2</sub> films (Kholmanov *et al.*, 2003)

The spectra show the structural transformation from amorphous titania to anatase (a) to rutile (r) under thermal annealing conditions. Annealing at 400 °C caused the crystallization from amorphous phase to anatase. As the temperature increased

to 600 °C low intensity rutile peaks started to appear, after 800 °C the crystalline phases were mainly rutile.

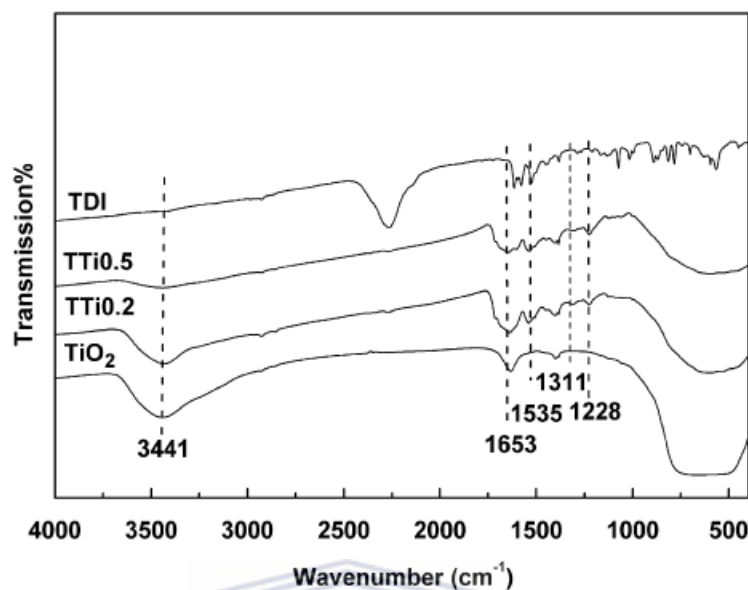


Figure 2.16: FTIR spectra of TiO<sub>2</sub> (P25) and modified TiO<sub>2</sub> (Jiang *et al.*, 2007)

Figure 2.16 shows the FTIR spectra of TiO<sub>2</sub> P25 along with modified TiO<sub>2</sub>. The peaks at 3441 and 1653 cm<sup>-1</sup> correspond to chemically adsorbed H<sub>2</sub>O onto the surface of TiO<sub>2</sub>. The broad peak in 750 – 500 cm<sup>-1</sup> region corresponds to Ti-O-Ti vibrations (Jiang *et al.*, 2007).

#### 2.4.2 Challenges associated with TiO<sub>2</sub>

One of the major challenges associated with TiO<sub>2</sub> is to increase the photocatalyst sensitivity to visible light. Anatase is the most photoactive phase but is only active in wavelengths shorter than 380 nm. There have been various attempts in research to overcome this limitation with little success (Aman *et al.*, 2012). The use of semiconductors other than TiO<sub>2</sub> that are active in the visible light region were unsuccessful, none of the semiconductors could meet the prescribed requirements (Umar and Aziz, 2013, p. 195). One catalyst, InTaO<sub>4</sub>, was reported to split water under visible light but with very low efficiency. Doping of the catalysts with metal ions also proved to be fruitless. However, when doping with non-metals such as nitrogen, sulphur and carbon, Fujishima and Zhang, (2006) reported significant red shifts up to 540 nm of the spectral limit of TiO<sub>2</sub> and this discovery

lead to the development of visible light TiO<sub>2</sub> (VL-TiO<sub>2</sub>) (Fujishima and Zhang, 2006). Mekprasart *et al.*, (2013) also found doping TiO<sub>2</sub> with nitrogen resulted in an absorption spectrum shift to the visible region.

Doping with non-metal elements proved to be quite successful in increasing the sensitivity of TiO<sub>2</sub> to sunlight. Xiao *et al.*, (2008) synthesized carbon-doped TiO<sub>2</sub> nanoparticles via sol-gel auto-combustion. The photocatalytic ability of the nanoparticles was evaluated on the rate of MB degradation under solar irradiation. The carbon doped catalyst showed increased activity in the visible light range which was attributed to the presence of an oxygen vacancy state between the valence and conduction bands. Albeit successfully improving catalytic efficiency, active surface area was the limiting factor. Increasing catalyst loading was effective in improving catalytic efficiency but was limited with an end point concentration where after light shielding impeded adequate irradiation.

There have been many attempts to enhance the photocatalytic efficiency of TiO<sub>2</sub>; dopants have been primarily used to enhance the absorbance of visible light. Yu *et al.*, (2012) investigated the effect of cerium doped SiO<sub>2</sub>/TiO<sub>2</sub> nano fibres. Cerium, amongst the lanthanides is the most favoured dopant and SiO<sub>2</sub> has been reported to enhance photocatalytic activity in the visible light region. The Ce-doped SiO<sub>2</sub>/TiO<sub>2</sub> fibre's degradation ability was assessed for its ability to degrade MB. The composite fibres showed higher photocatalytic ability for degrading MB compared to Degussa P25 and samples doped with only Ce or SiO<sub>2</sub>. Hydroxyl radicals are known to be powerful oxidants consequently the dominating photo oxidants were the hydroxyl groups. Limiting the electron acceptors, that would act as scavengers of OH<sup>•</sup>, proved to increase the photocatalytic efficiency (Liu *et al.*, 2012).

### **2.4.3 Catalysis from nano to macro scale**

For photocatalysis, the use of pellets is impractical. Semiconductor catalysts have to be fully irradiated. Therefore, most systems use fine powder catalyst dispersions which require a final filtration step. In photocatalysis, it is well established that the reaction rate is dependent on the radiant flux and catalyst mass

under slurry conditions. Adequate illumination of the catalysts requires a maximum loading range usually between 0.6 – 2.5 g/L. Higher loading capacities can result in light scattering. To extort the maximum potential from these photonic materials immobilization of these materials are crucial (Manuel and da Silva, 2009). Ballari *et al.*, (2008) reported the concentration profile of photocatalyst loading within a reactor to be dependent on the turbulent flow of a system. Their simulation was based on the mass transfer limitations in slurry photocatalytic reactors. It was a physical study that employed parameters based on an existing operating reactor. They found concentration of TiO<sub>2</sub> in powder form above 1 gL<sup>-1</sup> to obstruct the radiation path length and affect the opaqueness of the system.

#### **2.4.4 Catalyst support structures**

Research has seen a fair amount of studies performed on light induced mineralization of organic pollutants using the photocatalyst TiO<sub>2</sub> in the quest to develop new technologies for the remediation of water and air. Torimoto *et al.*, (1996) investigated the role of a photocatalyst support on the degradation of propyzamide and its effects on the reaction intermediates. The catalyst supports that were used for TiO<sub>2</sub> loading were zeolites, silicon powders and activated carbon (AC). The performances of the supported catalysts were compared to that of naked TiO<sub>2</sub>. The use of adsorbent support was found to enhance the rate of mineralization of propyzamide and also reduced the concentration of solution-phase intermediates. It must be noted that the feat was not in the ability to mineralize propyzamide. Over 90% of propyzamide was mineralized by all the catalyst including the naked TiO<sub>2</sub>, but in the rate at which CO<sub>2</sub> was formed; CO<sub>2</sub> production was used as a mineralization measure. It was concluded that the supported catalyst performance was due to its capability to collect degradation intermediates from the solution phase allowing for complete mineralization to proceed (Torimoto *et al.*, 1996; Gao *et al.*, 2007).

Single wall carbon nanotubes (SWCNTs) possess unique electronic and electrical properties. There have been many attempts to improve the efficiency of light harvesting semiconductor particles. Carbon nanotubes (CNTs), also known as

organic semiconductors, have been found to enhance the performance of organic photovoltaics with their unique electronic properties, wide electrochemical stability window and high surface area. Kongkanand *et al.*, (2007) found CNTs as anchor support for TiO<sub>2</sub> to greatly enhance the charge transport properties of TiO<sub>2</sub>/SWCNTs and to improve the photocurrent generation in TiO<sub>2</sub> photoelectrochemical solar cells. Apart from the improved surface area, the electron-accepting ability of the semi-conducting materials is why CNTs were such fitting anchors for the photocatalysts (Kongkanand *et al.*, 2007).

There have been great advances in the TiO<sub>2</sub>/CNTs composite systems. Woan *et al.*, (2009) in their study on TiO<sub>2</sub>/CNTs composites addressed the photocatalytic activity and challenges posed by the composites. The addition of CNTs was found to increase the photocatalytic properties of TiO<sub>2</sub>. The addition of CNTs successfully retarded electron hole recombination due to its large electron storage capacity. CNTs facilitated greater surface areas for the catalyst and modification of the CNTs surface groups also improved the adsorption of specific species. However, these systems have been crippled by high yield synthesis techniques such as metal catalyst deposition through CVD exhibiting non-uniform or uneven product property issues affecting the photocatalytic activity of the CNTs. They also reported residual catalyst materials to cause fouling of the nanotubes (Woan *et al.*, 2009).

Gao *et al.*, (2007) synthesized hybrid catalysts by dipping CNTs in a titanium precursor sol-gel which was thermally treated to induce the phase transition to TiO<sub>2</sub>. They found the supported catalyst to have greater photocatalytic ability for the degradation of acridine dye than the naked TiO<sub>2</sub> particles. However it must be mentioned that this was only for the TiO<sub>2</sub>/CNTs sintered at 300 °C.

Bhattacharyya *et al.*, (2004) investigated the affect of inert mesoporous, microporous and pillared supports structures on the photocatalytic ability of TiO<sub>2</sub>. Orange II was used to evaluate the photocatalytic efficiency of the composites. Optimization of catalyst loading presented the best results at 50 wt%. The TiO<sub>2</sub> nanoparticles were synthesised by an acid catalysed sol-gel formation method using 30 mL of 1 M HNO<sub>3</sub> and 7.4 mL titanium tetra-isopropoxide. The titanium

isopropoxide was added to  $\text{HNO}_3$  under continuous stirring for 1.5 – 2 hours. The sol-gel was diluted with deionised water and the pH was readjusted to 3. Depending on the wt% loading the adsorbent was added to the suspension. The resultant mixture was stirred for 2 hours that was followed by centrifugation and washing with deionised water until the pH of the supernatant was 6. The composites effectively removed the azo-dye orange compared to bare  $\text{TiO}_2$ . The improved performance was attributed to enhanced surface area of the support as well as catalyst crystallinity. The supports used were MCM-41 a mesoporous support (surface area  $>900 \text{ m}^2/\text{g}$ ),  $\beta$ -zeolite (surface area 650 – 680  $\text{m}^2/\text{g}$ ) and Al-pillared montmorillonite (surface area 280 -350  $\text{m}^2/\text{g}$ ). The nature of the dye was found to be influential in the adsorption onto the adsorbent. The pure supports displayed poor adsorption capacity due to electrostatic repulsion caused by the acidity of orange II and its ionic character. Only at maximum catalyst loading of  $\text{TiO}_2$  did adsorption improve (Bhattacharyya *et al.*, 2004).

To assess the interaction between activated carbon (AC) employed as a catalyst support, Arana *et al.*, (2003) studied the use of different portions of AC mixed with  $\text{TiO}_2$ . The purpose of the study was to assess if matrix support structures can eliminate coagulation of the catalyst and enhance dispersion. Their results suggested that it is not just a case of contact between the two phases but the possibility of changes in the physico-chemical features of  $\text{TiO}_2$ . FTIR results indicated a shift in the hydroxylic group vibration compared to the bare  $\text{TiO}_2$ . Conglomeration was also found to only arise once the catalyst loading capacity exceeded the 13 wt% mark. Not only did the AC support structures improve the active surface area of the catalyst but consequently enhanced the catalyst photocatalytic ability as well (Arana *et al.*, 2003).

Menesi *et al.*, (2008) examined the catalytic properties of  $\text{TiO}_2$ /montmorillonite nanocomposites to determine the influence that silicate had on the catalytic degradation of organic pollutants. In their study a 0.5 mM aquatic phenol solution was used to simulate organic pollutants. Degussa P25  $\text{TiO}_2$  was used as the photocatalyst. The study was conducted in the liquid phase. The study revealed a

significant improvement in the photocatalytic ability of the nanocomposite material (Menesi *et al.*, 2008).

Qiu and Yu, (2008) were able to synthesise TiO<sub>2</sub> nanotubes with anatase structures. The tubes were synthesised by impregnating stabilised electrospun PAN nanofibres with TiCl<sub>4</sub> and calcining the composite fibres. The PAN fibres were electrospun from a 7 wt% solution with an applied potential of 20 kV. The fibres were stabilised in air for 2 hours at 250 °C as a pre-treatment step to improve the wetting properties of the PAN fibres. The TiCl<sub>4</sub> solution was prepared by dissolving 2 mL of TiCl<sub>4</sub> in a 100 mL 75:25 ethanol/water mixture. The stabilised electrospun PAN fibres were then impregnated with 5 mL of the TiCl<sub>4</sub>. This was followed by impregnation of the PAN fibres with a 0.5 mL 0.1 M ammonia solution. The fibres were then calcined at 550 °C from room temperature at a heating rate of 0.5 °C/min and maintained for 2 hours in air (Qiu and Yu, 2008).

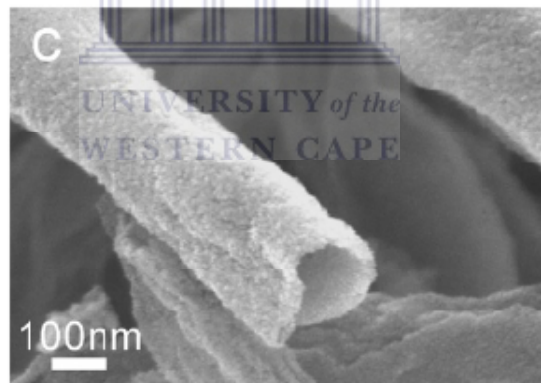


Figure 2.17: SEM image of TiO<sub>2</sub> nanotube (Qiu and Yu, 2008)

Figure 2.17 shows a SEM image of the structure of the TiO<sub>2</sub> nanotubes that had an average diameter of 220 nm.

Shrestha *et al.*, (2010) synthesised TiO<sub>2</sub> loaded with nickel oxide nanoparticles. The TiO<sub>2</sub> nanotubes were grown by anodising a titanium substrate in a 65 % glycerol-H<sub>2</sub>O electrolyte containing 0.27 M NH<sub>4</sub>F. The tubes were then annealed in air at 450 °C for 3 hours. The tubes were impregnated with nickel oxide nanoparticles by soaking the tubes in ethanol containing 0.2 M NiCl<sub>2</sub>.6H<sub>2</sub>O for 12

hours. This was followed by soaking the tubes in 0.2 M  $\text{NH}_4\text{OH}$  for 12 hours. The synthesised tubes were then subjected to photocatalytic tests using acid orange azo-dye. The photocatalytic decomposition of the azo-dye was carried out by illuminating the nanotubes surface with visible light. The photocatalytic activity of the tubes were compared to N-doped  $\text{TiO}_2$ , the nickel oxide loaded  $\text{TiO}_2$  nanotubes showed greater photocatalytic activity.

A study by Prahsarn *et al.*, (2011) investigated PAN fibres as support material for photocatalyst  $\text{TiO}_2$ . Commercial anatase with an average particle size of 25 nm was used. To synthesize the fibres containing the catalyst, the PAN/DMF/ $\text{TiO}_2$  solutions were electrospun. The concentration of  $\text{TiO}_2$  ranged between 0 – 3 wt% and was added to a 5 wt% PAN/DMF solution. The sol-gel solution was injected into a 1 mL syringe with a 24 gauge needle. The syringe was tilted  $60^\circ$  from horizontal to allow for gravitational flow, the flow rate was measured at 0.012 mL/min. The tip to collector distance was 12 cm. The system was connected to a 20 kV power supply. The average fibre diameter for the PAN/DMF/ $\text{TiO}_2$  solutions was in the range of 170 – 220 nm. The fibres that were spun from the PAN/DMF/ $\text{TiO}_2/\text{H}_2\text{O}$  solutions that were introduced were found to be larger in size ranging from 240 – 305 nm and 340 – 430 nm. MB degradation served as a model to measure the photocatalytic activity of the fibres. The results showed that the electrospun fibres with higher catalyst concentration displayed the highest photocatalytic rate, after 24 hrs almost 80% of the dye was degraded. The PAN/DMF/ $\text{TiO}_2/\text{H}_2\text{O}$  nanofibre webs exhibited even greater activity (Prahsarn *et al.*, 2011).

Im *et al.*, (2008) electrospun PAN nanofibres containing  $\text{TiO}_2$  to test the photodegradation effect of the nanofibres. Titanium (IV) oxide anatase powder was used as photocatalyst. The fibres were electrospun from a polymer solution that was prepared with a 1:1:9 PAN:  $\text{TiO}_2$ : DMF weight ratio. Rhodamine B was used to simulate organic pollutants for the photodegradation study. The fibres were electrospun under the following conditions 15 kV applied potential,  $1.5 \text{ cm}^3/\text{hr}$  flow rate and collector plate distance of 10 cm. The fibres were collected on a rotating collector plate with a rotation speed of 300 rpm. The photocatalytic

study was conducted under UV light with a 15 W light source (365 nm). The average fibre diameters were about 800 nm. The maximum dye degradation was achieved over 38 hours removing 80 % of the Rhodamine B dye.

## **2.5 Electrohydraulic discharge reactors**

The past decade has seen extensive research in developing pollution treatment methods. Plasma generating techniques are extremely energy efficient and along with the ambient conditions at which the oxidative processes occur has lead to substantial interest from industry.

Recent years have witnessed inventions that differ from standard plasma treatment techniques. The plasma reactor system is a highly pressurized in-line dielectric fluid system with simple, low cost, low energy capabilities to treat pressurized dielectric fluids such as carbon dioxide, nitrogen, compressed air and other high-pressure fluids. The system employs an advanced oxidation process wherein a continuous high voltage and high frequency electrical discharge is applied through a dielectric barrier to a flowing stream of high-pressure gaseous, liquefied or supercritical fluid to form high energy plasma. The high-pressure plasma directly oxidises or mineralises organic contaminants present in the high pressure fluid. Complex organic molecules are readily broken down into smaller oxygenated species or completely broken down to carbon dioxide, nitrogen and water. Metal organics are reduced to metal oxides or salts that can be precipitated from the treated fluid (Jackson, 2003).

Locke *et al.*, (1996) developed a system that is driven by corona induced reactions. This process used sources in addition to oxygen, such as transition metals, in a corona reactor to generate hydroxyl radicals produced by corona discharge to enhance its oxidation capabilities. The addition of the sources, such as iron or copper, to the corona reactor led to a decrease in exposure time and increase in efficiency of the corona discharge system.

Another more recent invention was the development of a water treatment apparatus that employs ultraviolet radiation and ozone to get rid of potential biological pathogens. The system has a water inlet and outlet that facilitates a flow

path for the water. The system houses multi-unit electrodes that are located across the flow path of the water. Once connected to the power supply electrodes generate UV radiation. The electrodes are housed in UV-transparent tubular housing designed in a manner to create an air gap that allows for corona creation. Unique to this system is the incorporation of supported photocatalysts to be used in the water treatment apparatus in conjunction with UV radiation to enhance the overall efficiency of the system (Okolongo *et al.*, 2011)

## 2.6 Characterisation of nanomaterials

There are a number of characterization techniques that can be used to gain insight into the size and morphology of nanomaterials. Continuous development in instrumentation especially microscopy allowed scientists to monitor phenomena at the angstrom-level. Scientists now have much greater insight of the inner workings of these nanomaterials.

Scanning electron microscopy (SEM) and transmission electron microscopy (TEM) are used to resolve images at the nanoscale. XRD is a very useful characterisation tool that can be used to, non-destructively, study the crystallographic structure, chemical composition and physical properties of materials and thin films. It can also measure the structural properties of the crystalline phases of crystalline materials (Sharma *et al.*, 2012). Raman spectroscopy is an excellent tool for assessing structural differences in nanomaterials as it provides important information about the connectivity in the materials (Santos *et al.*, 2010) to study the phase transitions on the fibres. Infrared spectroscopy is used to characterise the structure of matter at the molecular scale. FTIR spectroscopy is based on the infrared spectroscopy principle, over the past few years its application has extended to the study of nano-scaled objects. FTIR can display the various bonding in material, however, it has been reported by Baudot *et al.*, (2010) that the existing database might not cover all bonding information present in nanomaterials. Therefore to extend applicability of FTIR to nano-material Baudot *et al.*, (2010), in their study on the covalent grafting of epoxide molecules on CNTs, derived a theoretical method to derive FTIR

spectroscopy and compare it with their experimental results (Vinu and Madras, 2010; Lue and Nalwa, 2007; Chen and Mao, 2007; Baudot *et al.*, 2010)

## 2.7 Summary

This chapter discussed various aspects pertaining to nanofibres and photocatalysis and also reviewed the most influential parameters in electrospinning while discussing the parameters that influences the fabrication of nanofibres. According to Yorderm *et al.*, (2008), electrospinning nanofibres at lower polymer concentrations appeared to be more effective. Li and Xia, (2003) made electrospun TiO<sub>2</sub> containing PVP polymer nanofibres with fibre diameters in the range of 20 – 200 nm, however PVP is hydrophilic and is not suited for water systems and required further heat treatment steps to remove organic substances. Im *et al.*, (2008) successfully loaded TiO<sub>2</sub> onto electrospun PAN nanofibres, with a 10 wt% polymer concentration, and they were able to degrade Rhodamine B. The fibres synthesised by Im *et al.*, (2008) had an average diameter of 800 nm and were only able to degrade 80 % of the Rhodamine B dye over 38 hours. They reported the best photocatalytic degradation of MB was attained by floating the fibres on top of the solution and not submerging in the solution. According to Prasharn *et al.*, (2011), TiO<sub>2</sub> containing PAN polymer fibres with a 5 wt% polymer concentration can be electrospun with fibre diameters in the range of 170 – 430 nm. Water was added to the sol-gel to introduce the formation of porous structures on the fibre surface. In addition, the photo-decomposition of MB presented by the TiO<sub>2</sub> containing PAN fibres demonstrated a photocatalytic degradation of about 80 % over 24 hours.

PAN polymers contain functional groups that might be vulnerable to radical degradation have been heat-treated but are reported to have low breaking strain and significant brittleness (Budylna *et al.*, 1995). It is important to determine the stability of these fibres and the effectiveness of the heat treated PAN fibres with respect to enhancing support structures for TiO<sub>2</sub>.

Considering recent work reported in literature, this study sets out to accomplish an improvement in the electrospinning of hydrophobic TiO<sub>2</sub> PAN polymer nanofibres by utilising a better and more proficient electrospinning system aimed

to further decrease the fibre diameter. Also the hydrophobic polymer PAN will be used to electrospin nanofibres with greater physical and chemical stability that may not require additional thermal stabilisation steps. The photocatalytic ability of these TiO<sub>2</sub> containing fibres will be assessed for overall stability and improved rates of photocatalytic degradation of organic pollutants.

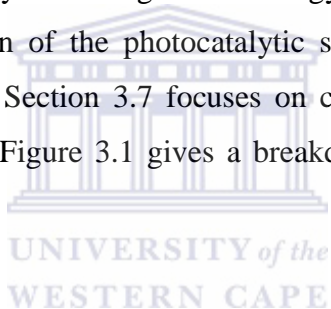
The next chapter introduces, sample preparation, experimental setup, sample material preparation and characterization techniques used.



## Chapter 3

### 3. Methodology

The following chapter outlines the methodology and the equipment that were used to achieve the goals for each section of the study. The section also provides information about the materials and chemicals that were required in the synthesis steps. The chapter is split into several subsections where each section is dedicated to an elemental step of the study. The first section of the chapter will list the chemicals and equipment that were used in the study. The next two sections of the chapter will be dedicated to the methodologies associated with the chemical and physical parameters of electrospinning in that order. Thereafter there will be focus on the ambient parameters of electrospinning and the subsequent monitoring thereof. Next, the catalyst loading methodology is described in section 3.5 followed by a discussion of the photocatalytic study and the key aspects that accompany the process. Section 3.7 focuses on characterization techniques that were used in the study. Figure 3.1 gives a breakdown of the macro plan of the study.



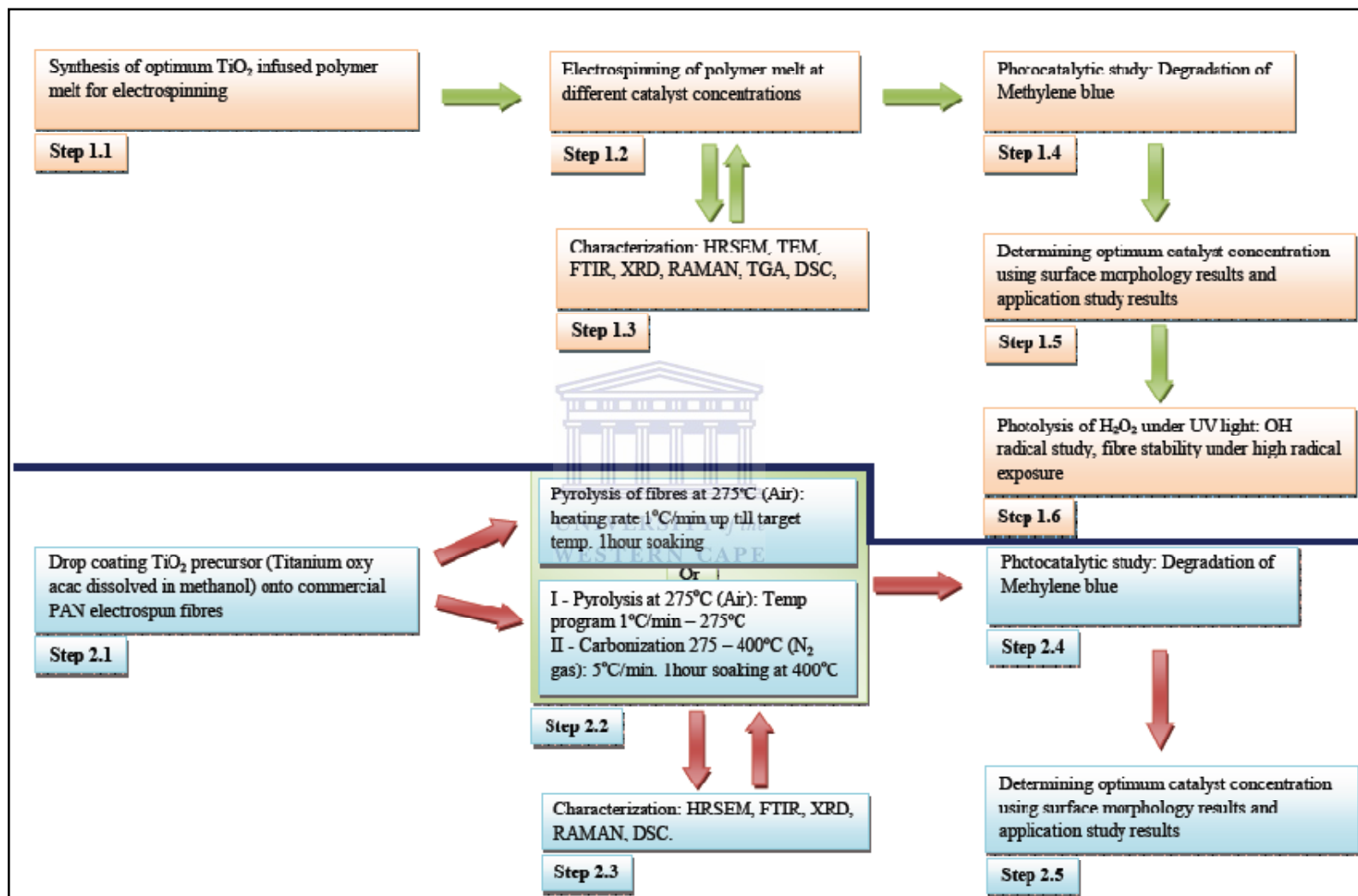


Figure 3.1: Research methodology of the photocatalytic study

### 3.1 Chemicals and Equipment

The list of chemicals and equipment that were used in the study is given in Tables 3.1 and 3.2

Table 3.1: List of chemicals

Chemical Name	Source	Specification
Polyacrylonitrile (PAN)	B&M Scientific	Mw. 150 g/mol
Dimethylformamide (DMF)	B&M Scientific	AR Grade
Commercial titanium dioxide (TiO <sub>2</sub> )	KIMIX Chemicals and Laboratory Suppliers, RSA	21 nm, ≥ 99.5% trace metals basis
Titanium (IV) oxyacetylacetone TiO[CH <sub>3</sub> COCH=C(O-)CH <sub>3</sub> ] <sub>2</sub>	Sigma Aldrich, RSA	90%
Polyacrylonitrile A3 size Nanofibres mats	Stellenbosch Nanofibre Company	15 g/m <sup>2</sup> 380 nm (47% variation)
Hydrogen Peroxide (H <sub>2</sub> O <sub>2</sub> )	MERCK Chemicals	AR Grade
Methylene Blue (MB) (C <sub>16</sub> H <sub>18</sub> N <sub>3</sub> SCl)	Sigma Aldrich, RSA	Basic Blue 9

Table 3.2: List of equipment

Equipment	Source
Needles Sterican 18 Gauge	KIMIX Chemicals and Laboratory Suppliers, RSA
Syringe Pack	KIMIX Chemicals and Laboratory Suppliers, RSA
Magnetic stirrer bar	KIMIX Chemicals and Laboratory Suppliers, RSA
Electrospinning power supply	Home built, 25 kV high voltage PSU
UV lamps 9 W 254 nm (Osram)	Starlight wholesale electrical suppliers
Digital Hygrometer (Hilitron Model No.:HT-8020)	CJ chemicals
Syringe pump 33	Harvard Apparatus

### 3.2 Electrospinning chemical parameters

Several publications have shown polymer concentration to be vital in fibre diameter. The optimum PAN polymer concentration range for nanofibre fabrication has been reported to be in the range of 8 to 10 wt% (Yordem *et al.*,

2008). Lin *et al.*, (2005) reported PAN polymer concentrations as low as 6 wt%. The process for the PAN polymer sol-gel synthesis was adopted from Gu *et al.*, (2005). Table 3.3 shows the PAN sol-gel formulations used for the different polymer concentrations.

Table 3.3: Formulation for polymer solutions

<b>Polymer Concentration wt%</b>	<b>Polymer weight (g)</b>	<b>Solvent weight (g)</b>
6 % PAN/DMF	3.0 g	47.0 g
7 % PAN/DMF	3.5 g	46.5 g
8 % PAN/DMF	4.0 g	46.0 g
9 % PAN/DMF	4.5 g	45.5 g
10 % PAN/DMF	5.0 g	45.0 g

The PAN sol-gel synthesis procedure was adopted from Yordem *et al.*, (2008). The only difference to the procedure was the molecular weight of the PAN polymer that was used. In this study the molecular weight of the commercial polymer was 150 g/mol instead of 75 g/mol. In the study by Yordem *et al.*, (2008) they synthesised their own PAN polymer that allowed for them to manipulate the molecular weight of the polymer. In this study the PAN sol-gel was prepared by adding known amounts of the commercial PAN polymer to the dimethylformamide (DMF) solvent as shown in Table 3.3. The polymer was admixed with the solvent, sealed for 24 to 48 hours at room temperature and stirred by an electromagnetically driven stirrer until the polymer was completely dissolved. The PAN/DMF solutions were prepared in 50 g aliquots. The weight fraction of polymer varied between 6 and 10 wt%, the weight fraction for the solvent varied between 90 and 94 wt% i.e.  $(DMF (g) = 50g - ([concentration] \times 0.50))$ . The polymer solution concentrations were represented as a mass fraction where the mass of the polymer made up a fraction of the total mass of the solution. The procedure was repeated for each solution concentration and was kept constant throughout the study.

### 3.3 Electrospinning Physical parameters

Numerous studies performed on electrospinning report on the physical, chemical and ambient parameters required for nanofibre fabrication. The physical parameters for electrospinning were adopted from Yordem *et al.*, (2008). Their study investigated the interactive effects of the process parameters on the fibre diameter. Their results proposed several parameter ranges that fall within the nanofibre domain. The process was slightly modified; horizontal setup was used instead of the reported vertical setup. The syringe and spinneret setup was adopted from Im *et al.*, (2008). The experimental conditions for the electrospun fibres are outlined in Table 3.4 and in Figure 3.2 the electrospinning setup is illustrated.

Table 3.4: Physical parameters used for electrospinning

Physical Parameter	Unit	Specification
Applied voltage	(kV)	17.5
Flow rate	(ml/hr)	2
Tip to collector distance	(cm)	13.5
Syringe	(cc)	20
Needle	(gauge)	18

Once the electrospinning set up was in place the syringe was loaded with 5 g of the sol-gel solutions prepared (see Table 3.3), and mounted on the pump. The positive terminal of the power supply was connected to the needle and the negative terminal was connected to the aluminium collector plate that was horizontally fixed at a collector plate distance of 13.5 cm. This created an electrostatic field across the interface. Once the sol-gel flow was initiated the charged solution jetted across the interface in a fibrous fashion and collected on the collector plate. Three preliminary sets of fibres, EF-01, EF-02 and EF-03, were electrospun from the 6, 8 and 10 wt% PAN/MDF sol-gels to determine the optimum polymer concentration. The electrospinning setup is illustrated in Figure 3.2.

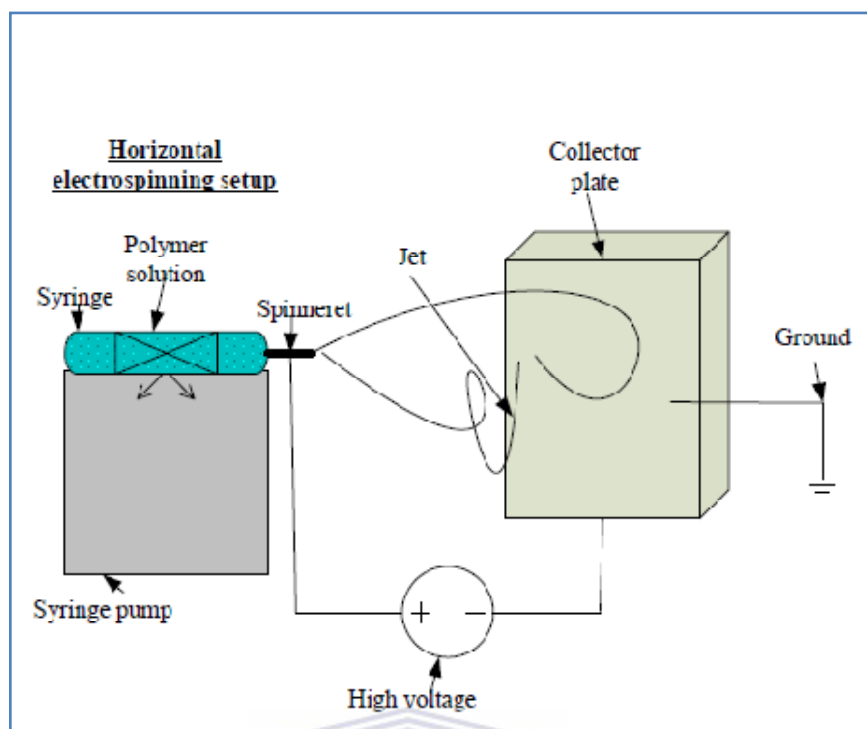


Figure 3.2: The horizontal electrospinning setup that was employed in the study (Bhardwaj and Kundu, 2010)

### 3.4 Ambient Parameters

Due to the physical setup of the laboratory it was not possible to control the ambient parameters. Instead the relative humidity was monitored by setting up a hygrometer inside the electrospinning setup.

### 3.5 Deposition of $\text{TiO}_2$ into and onto the electrospun nanofibres

The effects of catalyst loading percentage on structural support materials have been reported to be highly influential on the structural properties and photocatalytic effects of the catalyst. The following section discusses the procedures that were used to deposit the  $\text{TiO}_2$  photocatalyst both inside and on top of the electrospun nanofibres.

#### 3.5.1 Doping of the PAN sol-gel with $\text{TiO}_2$

To synthesise composite titanium PAN nanofibres, commercial  $\text{TiO}_2$  nanoparticles were added to the PAN/DMF polymers sol-gel solution. The

procedure for this study was adopted from Prahsarn *et al.*, (2011), however, only the 7 wt% PAN/DMF solution was utilized in this study. The catalyst loading procedure was a combination of two procedures adopted from Im *et al.*, (2008) and Prahsarn *et al.*, (2011). The TiO<sub>2</sub> containing fibres were prepared as specified in section 3.3.

For the study the TiO<sub>2</sub> loading concentrations for the 7 wt% PAN/DMF solution ranged between 3 to 10 wt%. For each catalyst concentration the wt% of TiO<sub>2</sub> nanoparticles were calculated to make up a wt% of the 5 g sol-gel solution as shown in Table 3.5. The wt% TiO<sub>2</sub> was calculated as follows eg. 3 wt% =  $5.0\text{ g} - (5.0\text{ g} \times 3\%)$ . The appropriate weight of TiO<sub>2</sub> was then admixed into the PAN sol-gel. To facilitate adequate dispersion of the TiO<sub>2</sub>, the catalyst was mixed with PAN/DMF solution by vortex vibration, adopted from Zhang *et al.*, (2010). The catalyst concentrations were represented as mass fractions where the mass of the catalyst made up a fraction of the total mass of the PAN/DMF solution. The preparation procedure for the polymer TiO<sub>2</sub> sol-gel can be seen in Table 3.5. The table identifies the wt% of TiO<sub>2</sub> that was added to the sol-gel solution for each concentration.

Table 3.5: Summary of the catalyst loading of the electrospun TiO<sub>2</sub> nanofibres

Sample	50 ml Sample Aliquot		7 wt% PAN/DMF solution (g)	TiO <sub>2</sub> (P25) (g)	TiO <sub>2</sub> Concentration (wt%)
	PAN Polymer (g)	DMF Solvent (g)			
EF-04a	3.5	46.5	4.85	0.15	3
EF-04b	3.5	46.5	4.75	0.25	5
EF-04c	3.5	46.5	4.65	0.35	7
EF-04d	3.5	46.5	4.5	0.5	10

Table 3.6: Summary of the procedure used for preparing electrospun PAN polymer nanofibres TiO<sub>2</sub> containing and PAN nanofibres

Sample name	Polymer	TiO <sub>2</sub> form	Procedure	Stabilisation	Temperature
EF-01	6 wt% PAN/DMF	NA	electrospinning	NA	NA
EF-02	8 wt% PAN/DMF	NA	electrospinning	NA	NA
EF-03	10 wt% PAN/DMF	NA	electrospinning	NA	NA
EF-04a	7 wt% PAN/DMF/3 wt% TiO <sub>2</sub>	Commercial TiO <sub>2</sub>	Physical admixture/electrospinning	NA	NA
EF-04b	7 wt% PAN/DMF/5 wt% TiO <sub>2</sub>	Commercial TiO <sub>2</sub>	Physical admixture/electrospinning	NA	NA
EF-04c	7 wt% PAN/DMF 7 wt% TiO <sub>2</sub>	Commercial TiO <sub>2</sub>	Physical admixture/electrospinning	NA	NA
EF-04d	7 wt% PAN/DMF/10 wt% TiO <sub>2</sub>	Commercial TiO <sub>2</sub>	Physical admixture/electrospinning	NA	NA

### 3.5.2 Deposition of TiO<sub>2</sub> on top of commercial electrospun nanofibres

To coat the commercial electrospun nanofibres the titanium oxy acac was deposited onto commercial PAN nanofibres obtained from a nanofibre company in Stellenbosch. In order to deposit the titanium oxyacetylacetonate onto the commercial electrospun nanofibres the precursor had to be dissolved ultrasonically in methanol and drop coated on the fibres. The technique was adopted from Castaneda *et al.*, (2002).



Four concentration profiles, 10 wt%, 15 wt%, 20 wt% and 30 wt% titanium oxy acetylacetonate were prepared individually, by coating the commercial PAN fibres, 4 x 2 cm in size, with titanium oxy acac. The profiles were assigned

according to the amount of precursor dissolved and drop coated onto the stabilised PAN fibre. Table 3.8 shows the amount of titanium oxy acac that was dissolved and drop coated onto the commercial electrospun nanofibres.

The commercial fibres modified with Ti oxy acac were prepared as follows: The commercial PAN nanofibres were weighed in order to determine the wt% of titanium oxy acac required for each set of fibres. As an example, the weight of the 4 x 2 cm commercial fibre sample was determined first in order to prepare the 10 wt% composite fibres. For a 0.0172 g fibre sample, a 10 wt% loading of the titanium oxy acac is required, equalling 0.0017 g (10 % in grams of the fibre weight). The 0.0017 g titanium oxy acac was dissolved ultrasonically in approximately 1 mL of methanol and drop coated onto the commercial PAN fibre. The centrifugal tube was rinsed with 0.5 mL of methanol to remove any residual Ti oxy acac. The fibre was then transferred to a crucible and placed in the furnace and stabilised under the appropriate conditions as set out in Table 3.7, for thermal oxidation of the Ti oxy acac to TiO<sub>2</sub>. The process of coating the commercial electrospun nanofibres with TiO<sub>2</sub> from here on forward will be referred to as thermal coating.

In order to synthesise the TiO<sub>2</sub> coated carbonised electrospun nanofibres, a similar catalyst loading procedure was followed as for the stabilised fibres as given above. As described earlier, the wt% of titanium oxy acac required for each concentration was calculated from the weight of the commercial PAN fibre used. The specific amounts of titanium oxy acac was then weighed and dissolved in methanol and drop coated onto the electrospun nanofibres. After the 275 °C stabilisation temperature was reached, the furnace was then heated further to 400 °C at 5 °C per minute. This further heating step was performed for 1 hour in nitrogen gas at 2 cm<sup>2</sup>/min flow rate.

Table 3.7 shows thermal conditions that were employed to stabilise and carbonise the commercial PAN nanofibres after loading the catalyst. At the same time the thermal procedures assisted in the crystallisation of titanium oxy acac to TiO<sub>2</sub>.

Table 3.7: Thermal conditions for stabilisation and carbonisation of the TiO<sub>2</sub> loaded fibres

	Heating rate (min <sup>-1</sup> )	Target Temp (°C)	Soaking time (hr)	Heating rate (min <sup>-1</sup> )	Target Temp (°C)	Soaking time (hr)
<b>TiO<sub>2</sub> coated Stabilised fibres</b>	1	275	1	N/A	N/A	N/A
<b>TiO<sub>2</sub> coated Carbonised fibres</b>	1	275	1	5	400	1

The nanofibres that were prepared during the experiments as specified in 3.5.2 are given in Table 3.8 with detail of all applied parameters.

Table 3.8: Summary of the commercial nanofibres coated with TiO<sub>2</sub>

Sample name	Polymer	Catalyst concentration (wt%)	TiO <sub>2</sub> form	Fibre weight (g)	Titanium oxy acac weight (g)	Thermal profile
EF-05	Commercial PAN fibre	10 wt%	10 wt% oxy acetylacetonate	0.0172	0.0017	Stabilisation – 275°C, 1 °C/min heating rate, Air
EF-06	Commercial PAN fibre	15 wt%	15 wt% oxy acetylacetonate	0.0182	0.0027	Stabilisation – 275°C, 1 °C/min heating rate, Air
EF-07	Commercial PAN fibre	20 wt%	20 wt% oxy acetylacetonate	0.017	0.0034	Stabilisation – 275 °C, 1 °C/min heating rate, Air
EF-08	Commercial PAN fibre	30 wt%	30 wt% oxy acetylacetonate	0.0191	0.0057	Stabilisation – 275 °C, 1 °C/min heating rate, Air
EF-09	Commercial PAN fibre	10 wt%	10 wt% oxy acetylacetonate	0.018	0.0018	After stabilisation carbonisation – 400 °C, 5 °C/min, nitrogen 2 cm <sup>2</sup> /min
EF-10	Commercial PAN fibre	15 wt%	15 wt% oxy acetylacetonate	0.0188	0.0027	After stabilisation carbonisation – 400 °C, 5 °C/min, nitrogen 2 cm <sup>2</sup> /min
EF-11	Commercial PAN fibre	20 wt%	20 wt% oxy acetylacetonate	0.0193	0.0038	After stabilisation carbonisation – 400 °C, 5 °C/min, nitrogen 2 cm <sup>2</sup> /min
EF-12	Commercial PAN fibre	30 wt%	30 wt% oxy acetylacetonate	0.0184	0.0054	After stabilisation carbonisation – 400 °C, 5 °C/min, nitrogen 2 cm <sup>2</sup> /min

### 3.6 Photocatalytic study

The light-driven decolouration of MB is an internationally approved standardised method used to test and compare photonic efficiency of photocatalytic coatings (Tschirch *et al.*, 2008). In order to investigate the photocatalytic activity of the composite samples, a photodegradation study using methylene blue (MB) was carried out under UV light irradiation (see Figure 3.3). The reaction was carried out inside an aluminium foil lined container. A 9 W Osram lamp was used as the UV light source (254 nm) and setup over a 500 mL glass beaker 3 cm from the solution surface. The solution was stirred using a magnetic stirrer. The reaction was prepared by submerging the TiO<sub>2</sub> coated fibres into a beaker containing a 100 mL of 10 mg/L methylene blue dye solution. The MB solutions were prepared via serial dilution. The concentration of methylene blue during and after the reaction was determined using UV Vis spectra. The calibration curves were prepared by making five standard methylene blue solutions of known concentrations. The concentration sequence was as follows 10 mg/L, 8 mg/L, 6 mg/L, 4 mg/L and 2 mg/L. The absorbance was determined with UV-vis spectrophotometer at 665 nm wavelength. In the experiment the fibres were soaked for 1 hour in contact with the MB solution (100 mL of  $x$  concentration) in the dark to allow for adsorption of MB to stabilise after which the initial MB concentration in solution was established. Both the TiO<sub>2</sub> coated oxidatively stabilised fibres (EF-05 – EF-08) and carbonised fibres (EF-09 – EF-12) sunk to the bottom of the 500 mL beaker where the sample remained undisturbed by the stirrer, at a very low speed, for the duration of the study. The electrospun PAN polymer fibres loaded with TiO<sub>2</sub> were mounted on cello-tape to prevent the fibres from floating around and to ensure adequate illumination. The total distance between the fibres and UV source was 4 cm. The mixture was stirred continuously from initial exposure for the duration of the reaction to facilitate adequate interaction of the dye with the catalyst. The photodegradation experiment was conducted for 8 hours. The dye removal was determined by sampling 10 mL, using a syringe, of MB solution at 2 hour intervals and measuring the absorbance at 665 nm wavelength using a UV-vis spectrophotometer.

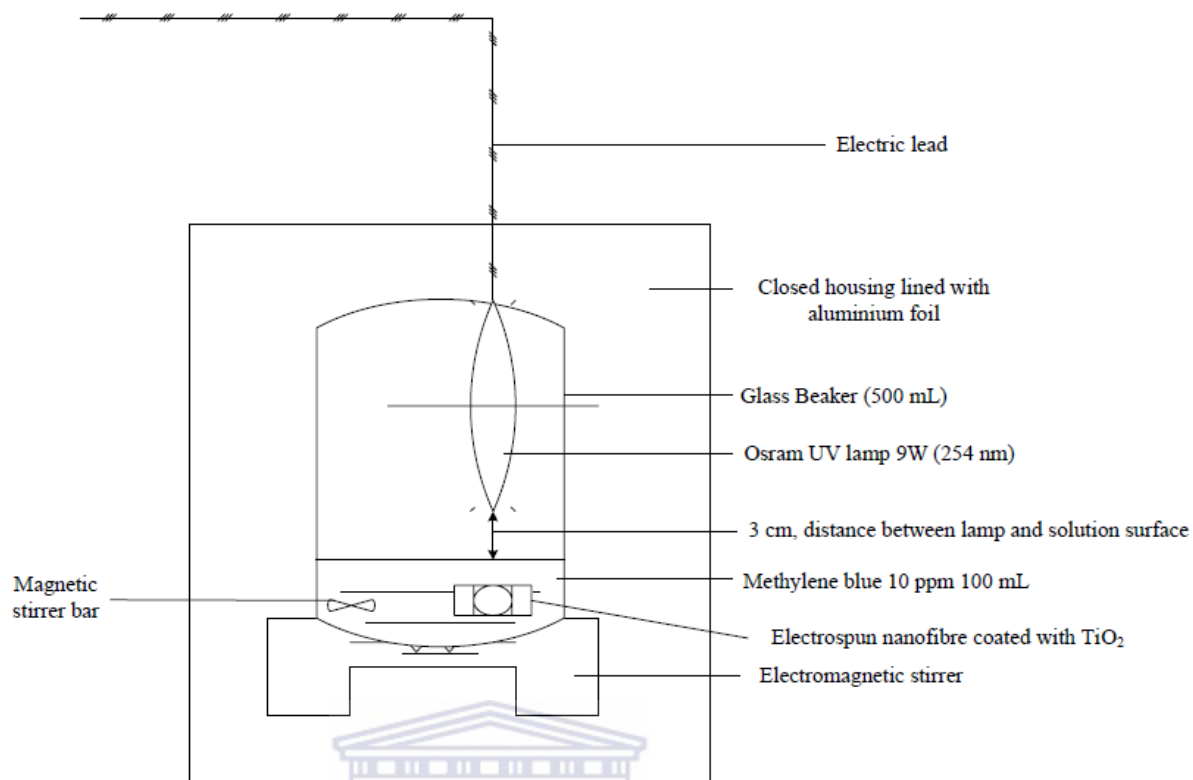


Figure 3.3: The photocatalytic degradation of methylene blue dye experimental setup

In order to establish the optimum catalyst loading and compare the photocatalytic ability of the different types of fibres, a control group was used to assess the photocatalytic fibre performance. The control group comprised of a blank experiment where the MB solution (100 mL 10 mg/L) only was subjected to UV irradiation. The second blank experiment was performed with the blank (0.0180 g) PAN polymer electrospun nanofibres without any TiO<sub>2</sub> incorporated and the third with the commercial TiO<sub>2</sub> (0.0020 g) powdered catalyst illuminated under UV light. The first two experiments, commercial PAN fibres and the MB UV-irradiated experiment, were conducted in order to establish any decolouration that is not related to the photocatalytic nanofibres. The third experiment was conducted as baseline to monitor and compare to the performance of the supported TiO<sub>2</sub> catalyst on the electrospun nanofibres and to determine any interference by the support material on the TiO<sub>2</sub>.

The MB degradation study was conducted for 8 hours whilst illuminated with a UV light intensity of 1.242 W/m<sup>2</sup>.

### 3.6.1 Dye degradation analysis

The Helios Epsilon UV Vis Spectrometer (Thermo Scientific) was used to measure the absorbance of the methylene blue solution during and after the photodegradation experiment. The absorbance was measured at a fixed wavelength (665 nm) and the concentrations for each solution were calculated as follows:

$$A = \epsilon lc(\text{Beer's Law}) \quad (\text{Eq. 3.1})$$

The concentration  $c$  was calculated using the absorbance  $A$ ,  $\epsilon$  (molar absorptivity) and  $l$  (cuvette path length). The slope of the calibration curve was determined as follow:

$$\text{Concentration } (c) = \frac{\text{Absorbance}}{\text{slope of calibration curve}} \quad (\text{Eq. 3.2})$$

The final concentration for each solution was calculated and expressed in mg/L. The degradation percentage was calculated by using the following equation:

$$\text{Degradation percentage } (\%) = \frac{C_i - C_f}{C_i} \times 100 \quad (\text{Eq. 3.3})$$

### 3.6.2 Photolysis of H<sub>2</sub>O<sub>2</sub> for OH radical formation

Advanced oxidation processes are characterized by the production of OH radicals. These radicals are highly reactive species and can attack most parts of organic molecules. PAN fibres are acrylic fibres with molecular formula [C<sub>3</sub>H<sub>3</sub>N]<sub>n</sub>. The functional groups can become the subject of radical interactions (Yusof and Ahmad, 2010). This photolysis study was conducted to assess the chemical stability of the composite photocatalytic electrospun nanofibres. The process adopted from Hislop and Bolton, (1999) was customised to subject the fibres to a high OH radical environment. The process by which the OH radicals are produced is shown in the following equation:



The EF-04b fibres were submerged in a 100 mL 4 ppm H<sub>2</sub>O<sub>2</sub> solution for different time intervals, 2 hours, 4 hours, 6 hours and 12 hours. Four EF-04b fibre samples, approximately 0.020 g in weight, were used with one sample per time interval. The experiment was conducted under UV light as set out in section 3.6.

### **3.7 Characterization techniques**

The following techniques were used to characterize the composite fibres; Transmission Electron Microscopy (TEM), High Resolution Scanning Electron Microscopy (HRSEM), Energy Dispersive Spectroscopy (EDS), X-ray Diffraction Spectroscopy (XRD), RAMAN Spectroscopy and Fourier Transform Infrared Spectroscopy (FT-IR). Thermal Gravimetric Analysis (TGA) and Differential Scanning Calorimetry (DSC) were used to establish the thermal profile of the fibres. The aim of characterization was to study the physical, chemical and thermal properties of the synthesized fibres.

#### **3.7.1 Rheological analysis**

To determine the viscosity of the different polymer concentrations rheological analysis was performed on the polymer sol-gel solutions. MCR300 rheometer (Anton Paar) was used to test the rheological properties of the polymeric material. The system was set to the shear rate profile. The sol-gel samples were placed in the concentric cylinder sample holder and analysed. The shear flow was determined by recording 30 data points with 5 second durations. Three replicates of each sample were performed.

#### **3.7.2 Physical characterization**

Physical characterization of the nanofibres were performed to image the morphology and nanostructures and to investigate the properties of the fibres.

##### **3.7.2.1 High Resolution Scanning Electron Microscopy**

The morphology of the electrospun fibres and photocatalyst was examined using a Zeiss scanning electron microscope. The structural and elemental aspects of the

fibres were investigated using an In-lens detector at low beam voltage of 5 kV. Low voltage imaging was used to minimize the charging effect of the fibres.

In order to obtain imaging, the fibres were subjected to a sample preparation step which involved a plasma sputter process, with an Au and Pd target done for 30 seconds under Ar gas. The sample was coated with Au and Pd to render it more conductive with a 60 % Au /40 % Pd ratio. This conductive process helps to improve the sample's mechanical stability and contributes to an overall improvement in the imaging of the sample.

### **3.7.2.2 Energy Dispersive Spectroscopy**

The energy dispersive spectroscopy (EDS) technique uses energy dispersion, which is the separation of x-rays according to their energies, to generate electronic signals. The strength of the electronic current from the crystal is proportional to the x-ray energy. The signals are then fed into a multi-channel analyser that plots the information as a spectrum which can be used for elemental detection and semi-quantitative analysis. EDS analysis was used to analyse the catalyst loading on the fibres as well as the dispersion across the fibres. The technique was performed using a Zeiss scanning electron microscope as for 3.7.2.1. The analysis was conducted after the HRSEM analysis requiring no additional sample preparation steps.

### **3.7.2.3 Transmission Electron Microscopy**

Transmission electron microscopy (TEM) characterization was performed on a HITACHI H-800 electron microscope. The system was operated using bright field imaging mode at an accelerating voltage of 200 kV using a Tungsten filament. The sample was prepared for analysis by sandwiching the sample of fibre between two copper grids. The grids along with the sample were mounted on the sample holder and characterized.

### 3.7.3 X-ray Diffraction Spectroscopy

The x-ray diffraction (XRD) technique is a technique used in crystallography. It is a diffraction technique that generates diffraction patterns that was used for the identification of the crystal structure and phase identity of the TiO<sub>2</sub> on the fibres.

The measurements were carried out with a D8 ADVANCE diffractometer from BRUKER AXS using an X-ray tube with copper K-alpha radiation operated at 40 kV and 40 mA and a position sensitive detector, Vantec\_1. The experimental conditions for the XRD instrument are presented in Table 3.9. Figure 3.4 shows a typical XRD spectrum of TiO<sub>2</sub> and anatase crystal phase TiO<sub>2</sub> that will be investigated in this study.

Table 3.9: XRD instrument conditions

Name of Instrument	D8 Advance BRUKER AXS
Scanning range in 2θ	10° - 90°
Step size in 2θ	0.028
Scan speed per step	0.5 sec
Operational parameters	40 kV and 40 mA
Detector	Vantec_1 (position sensitive)

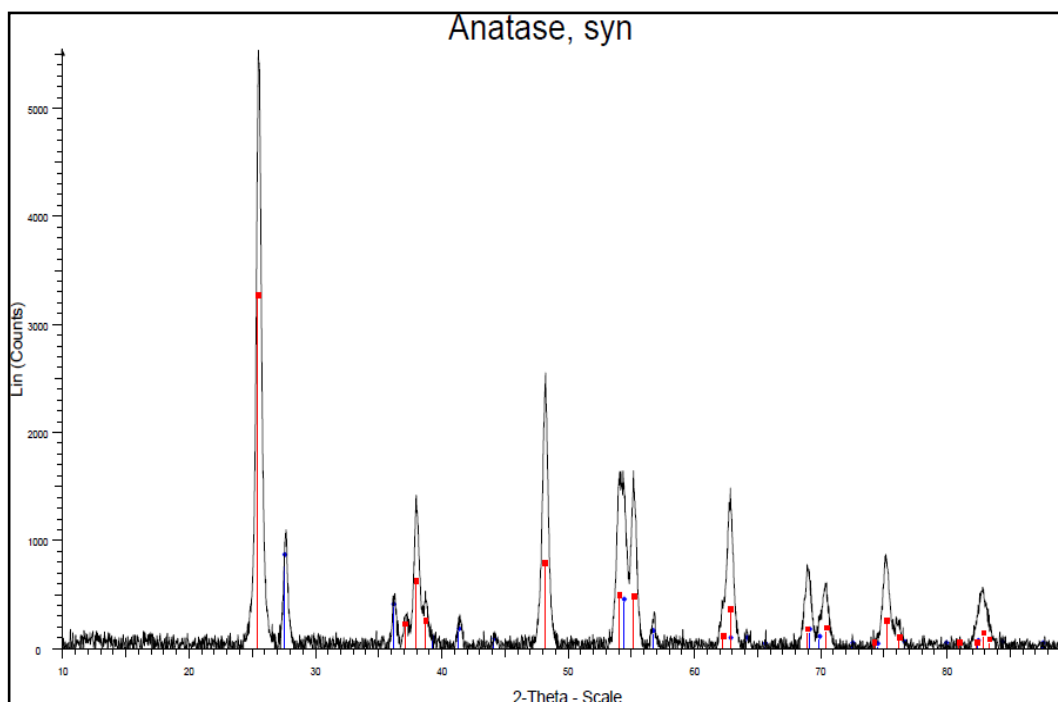


Figure 3.4: Characteristic XRD spectrum of TiO<sub>2</sub> (rutile) and anatase crystal phase TiO<sub>2</sub> (ICSD collection code: 024276 Anatase, syn; ICSD collection code: 202241Ti Oxide)

Figure 3.4 shows the major diffraction peaks for TiO<sub>2</sub> rutile (blue) at 27.6°, 36.1° and 54°. The major diffraction peaks for TiO<sub>2</sub> anatase (red) was at 25.2°, 38°, 48.1°, 54° and 55.1°.

### 3.7.4 Raman Spectroscopy

Raman spectroscopy studies the chemical structure and physical form of a molecule, and allows the identification of substances from characteristic spectral patterns and provides quantitative analysis of the amount of substance in a sample. It has been recognised as one of the most sensitive techniques for studying the structural properties of carbonaceous materials. The samples were characterised with an Xplora Raman Spectrometer from Horiba. For solid samples no sample prep was required. Solid state sample analysis is a non-destructive method. Two Olympus lenses for different magnifications were used. The samples were focussed at 10x magnification and recorded at 100x magnification using a

visible light 532 nm laser wavelength. The high wavenumber Raman spectroscopy was performed at  $2850\text{ cm}^{-1}$ .

### **3.7.5 Fourier Transform Infrared (FTIR)**

Fourier Transform Infrared spectroscopy was used to provide information on bonds and changes in bonding in the molecular structure of the fibre. The fibres were characterized with a Perkin Elmer 100 FT-IR spectrometer. This technique virtually required no sample preparation. The machine was cleaned and set up to obtain a background spectrum trial. The samples were placed on the attenuated total reflectance (ATR) sample holder and recorded in the range of  $4000 - 650\text{ cm}^{-1}$ . The spectrogram obtained was used to investigate changes in the characteristics of the sample.

### **3.7.6 Thermogravimetric Analysis**

The thermal behaviour of the electrospun fibres was established with thermogravimetric analysis (TGA). Before the analysis was performed the system was calibrated to stabilise the baseline. The thermogravimetric analysis was performed under air using a STA 6000 (PerkinElmer) thermal analyser. The samples were placed in an aluminium sample holder due to the low weight of the fibres. The heating rate of the sample was  $1\text{ }^{\circ}\text{C}/\text{min}$  up to  $300\text{ }^{\circ}\text{C}$  and  $5\text{ }^{\circ}\text{C}/\text{min}$  from  $300$  to  $850\text{ }^{\circ}\text{C}$  in air.

### **3.7.7 Differential Scanning Calorimetry (DSC)**

DSC analysis was performed on a PerkinElmer DSC 7. To check the system an Indium calibration was performed by running a blank to check the enthalpy of the system.  $1.2\text{ mg}$  of the PAN fibre sample was placed in an aluminium sample holder and compressed. The sample was analysed over  $50 - 400\text{ }^{\circ}\text{C}$  temperature range at a  $10\text{ }^{\circ}\text{C}$  heating rate per minute in nitrogen gas with a gas flow of  $20\text{ mL}/\text{min}$ .

## Chapter 4

### 4. Rheology of PAN polymer sol-gel and characteristics of electrospun fibres

#### 4.1 Introduction

This chapter describes the baseline characteristics of the formulated PAN polymer sol-gel and electrospun fibres made from it. The chapter is organized in a manner to show the electrospinning parameters as well as the bare PAN polymer fibres' characteristics. The optimum conditions obtained during the electrospinning experiments for nanofibre synthesis are also discussed. The baseline characteristics of the electrospun PAN fibres are detailed as determined by HRSEM, FTIR, RAMAN, TGA and DSC.

Chapter 5 discusses the modifications to PAN fibres imparted by TiO<sub>2</sub> incorporation.

The next section briefly describes the relationship between the formulated polymer solution concentration and viscosity. The assessment will be based on the rheological analysis of the PAN sol-gel at various concentrations and the impact of rheology on the shearing potential of the polymer.

##### 4.1.1 Optimum sol-gel formulation

The fibres were electrospun from a sol-gel solution composed of Polyacrylonitrile in Dimethylformamide (DMF). Polyacrylonitrile (PAN) is widely utilized in making ultrafiltration membranes, by casting the polymer film to a 300- $\mu$ m-thick film and precipitating it in water, for its high solvent resistance and chemical stability (Scharnag and Buschatz, 2001). The intended application of the fibres also required the polymer to be hydrophobic; therefore PAN with its high hydrophobic properties was the ideal polymer (Wang *et al.*, 2005). Commercially there are several solvents used for the preparation of PAN solutions, but DMF and dimethylacetamide displayed superior solubility capacities (Mataram *et al.*, 2011).

Rheological analysis was performed on the PAN/DMF sol-gel in order to determine the optimum PAN/DMF wt% ratio required to electrospin continuous

nanofibres and to determine the rheological properties of the various sol-gel solutions. The rheological analysis of the PAN polymer sol-gels, with wt% ratios as prepared in section 3.2, is shown in this section. The rheological analysis was performed as per procedure 3.7.1 for the 6 wt% (EF-01), 8 wt% (EF-02) and 10 wt% (EF-03) PAN polymer sol-gels (see Table 3.3). The results are graphically displayed below in Figure 4.1.

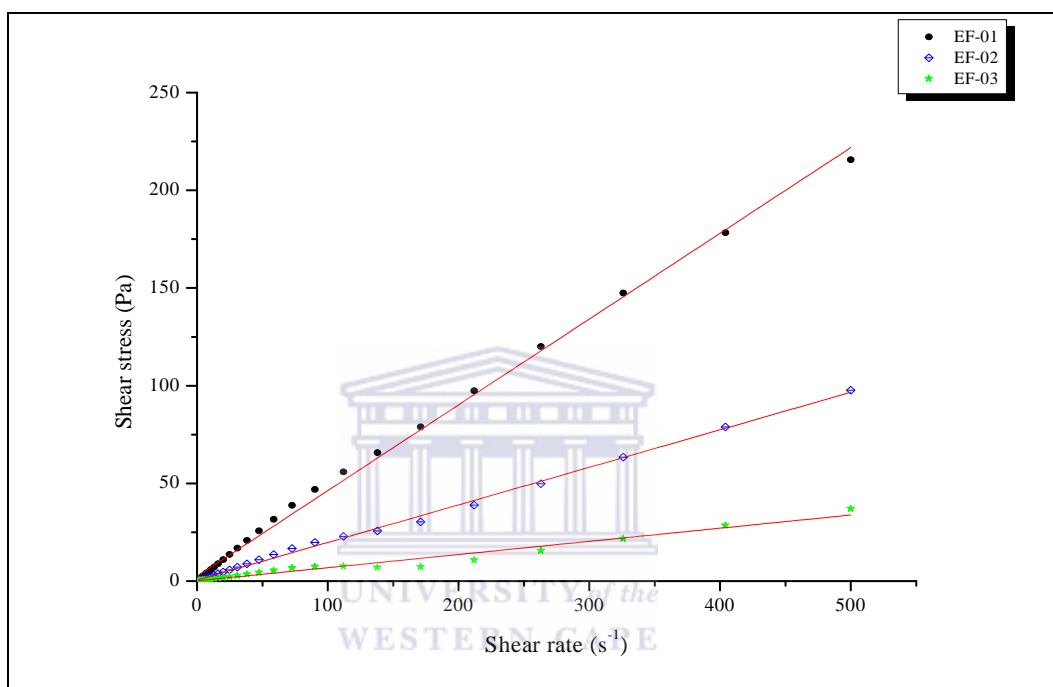


Figure 4.1: Shear stress versus shear rate for PAN/DMF sol-gel formulated to have 6, 8 and 10 wt% of PAN in DMF (EF-01=6 wt%; EF-02=8 wt%; EF-03=10 wt% PAN/DMF) (n=3)

The flow curves in Figure 4.1 display the correlation between shear stress and shear rate for each polymer solution. Each polymer solution appeared to be modified by the fluid flow. The flow curves in Figure 4.1 illustrate how the yield stress, the minimum stress that is required to induce deformation, for each polymeric solution increased as the concentration increased. Figure 4.1 identifies an allometric relationship between the sol-gel viscosity and concentration. The flow curves of the polymer solutions are representative of non-Newtonian fluid behaviour elicited at different polymer concentrations. As the polymer concentration increased the Newtonian plateau shifted upwards. When the stress applied to the polymer solutions was low the fluid flow was minimal. Only once

shear stress increased did fluid flow occur. This behaviour was confirmed by reports by Paquien *et al.*, (2005) who found similar trends in silica/PDMS dispersions. The shifts in the Newtonian plateau are due to increased inter-particle interactions up to where yielding transition takes place (Malkin, 2013).

Figure 4.2 illustrates the effect of increased polymer concentration on the solution viscosity.

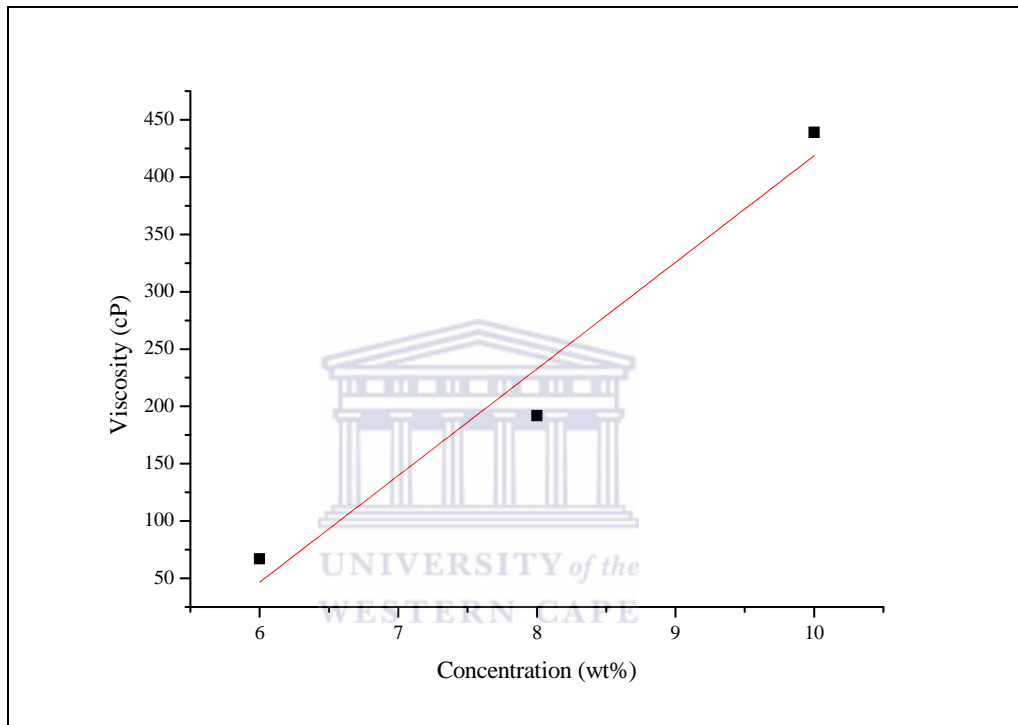


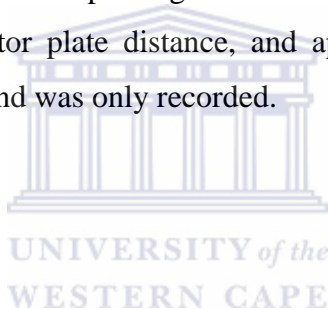
Figure 4.2: The effect of increasing polymer concentration on the sol-gel viscosity (n=3)

Figure 4.2 depicts the relationship between polymer viscosity and concentration. The polymer viscosity increased with concentration, yielding a straight line. However there appears to be a deviation in the trend for the 8 wt% PAN polymer solution. Each analysis was performed three times. The flow curve depicts a positive correlation between the solution viscosity and PAN concentration in DMF solvent.

#### 4.1.2 Morphology of electrospun fibres

The following section investigates the effect of polymer concentration on the electrospun fibre morphology. Figures 4.4 - 4.6 depicts the HRSEM images of the 6 wt%, 8 wt% and 10 wt% PAN/DMF electrospun fibres. The HRSEM analysis was obtained according to the procedure described in section 3.7.2.1. The electrospun fibres were characterised to assess the effect of the polymer concentrations and the electrospinning parameters on the fibre morphology. The fibres were electrospun from 6, 8 and 10 wt% PAN in DMF solutions as described in section 3.2.

Figure 4.3 shows the fibres that were electrospun under the physical parameters proposed by Yordem *et al.*, (2008), as presented in experimental section 3.3 which gives the procedure for electrospinning. The electrospun fibres were manipulated by flow rate, the collector plate distance, and applied potential. The humidity could not be controlled and was only recorded.



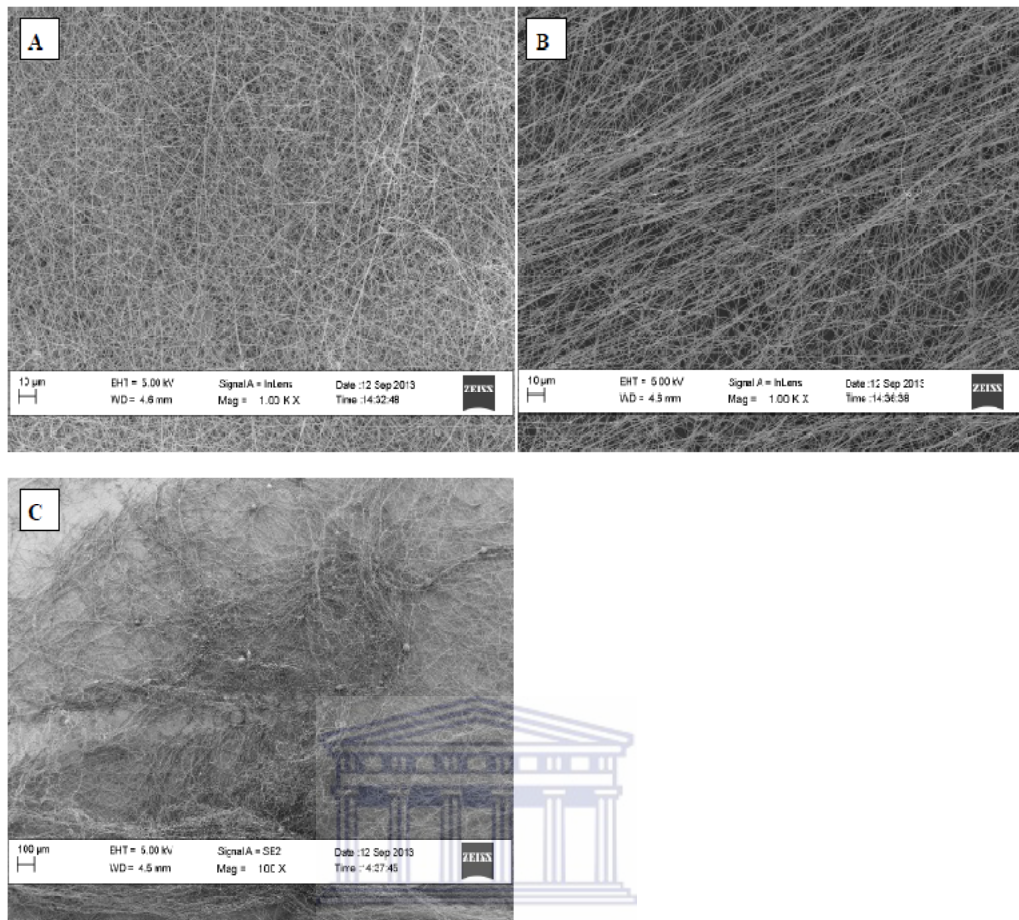


Figure 4.3: HRSEM images showing the preliminary electrospun fibres, (A) 6 wt% (EF-01), (B) 8 wt% (EF-02) and (C) 10 wt% (EF-03) PAN/DMF electrospun fibres without  $\text{TiO}_2$

Comparing the fibres, beads-on-string formation can be observed in EF-01 (A) and EF-03 (C) PAN fibres (see Figure 4.3). As the concentration of the polymer sol-gel increased the fibres started to smooth out and increase in diameter. Bead formation decreased and changes in the morphology of the fibres were observed as well. Beads-on-string has been reported to be prevalent at lower viscosity albeit rendering fibres with thinner diameters (Lin *et al.*, 2005). The interference in the uniformity of the fibres could be ascribed to the low polymer concentration (Lin *et al.*, 2005; Yordem *et al.*, 2008). This is due to an increased charge density on the Taylor cone. The coulombic repulsion overcomes the surface tension at a higher rate resulting in smaller droplet formation and a decreased charge density across the filament (Stanger *et al.*, 2009). The molecular weight of the polymer

prevents the filament from breaking instead it facilitates the connection between the beaded fibres (Gu *et al.*, 2005). Similar findings were reported by Raghavan *et al.*, (2012).

Figures 4.4, -5 and 4.6 show the higher magnification HRSEM images of the fibres presented in Figure 4.3.

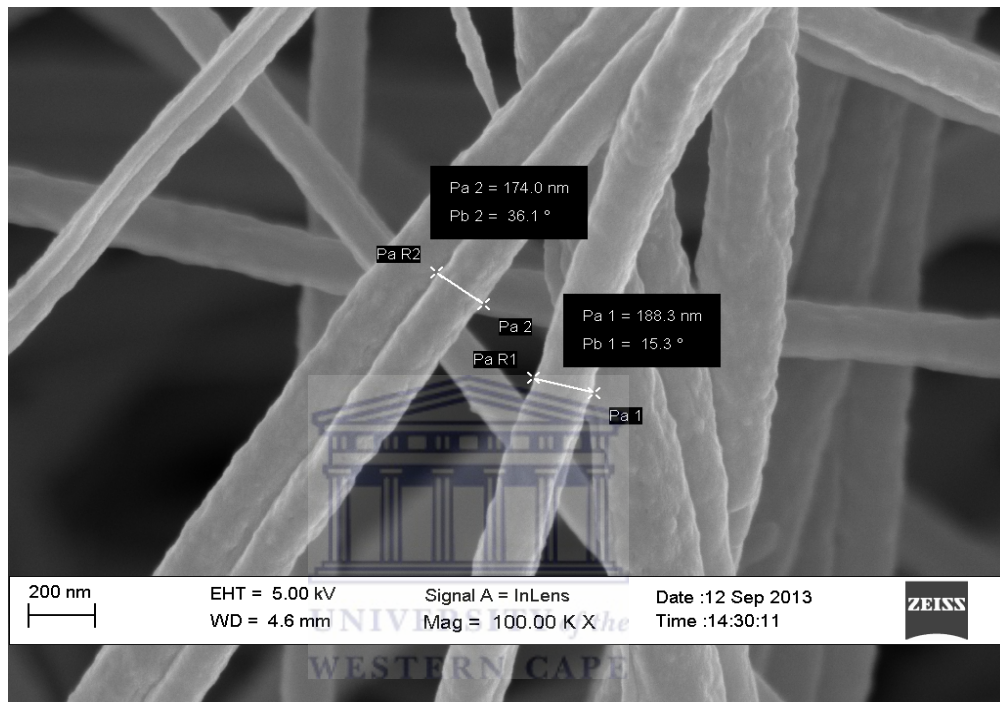


Figure 4.4: HRSEM image showing the morphology of the EF-01 nanofibres spun from the 6 wt% PAN/DMF sol-gel

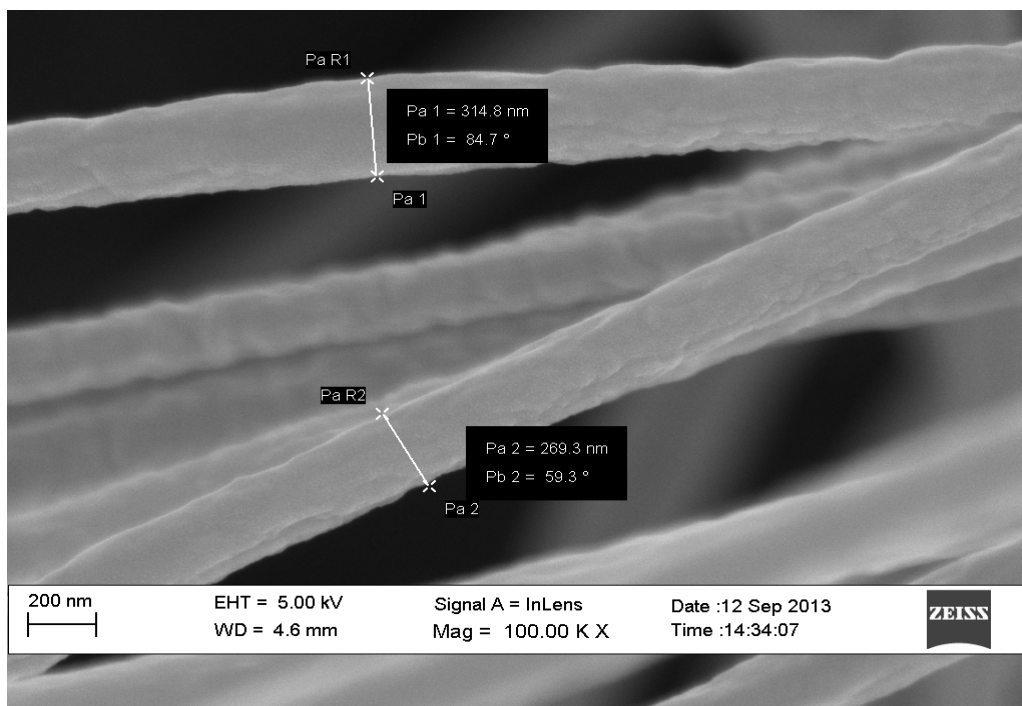


Figure 4.5: HRSEM image showing the morphology of the EF-02 nanofibres spun from the 8 wt% PAN/DMF sol-gel

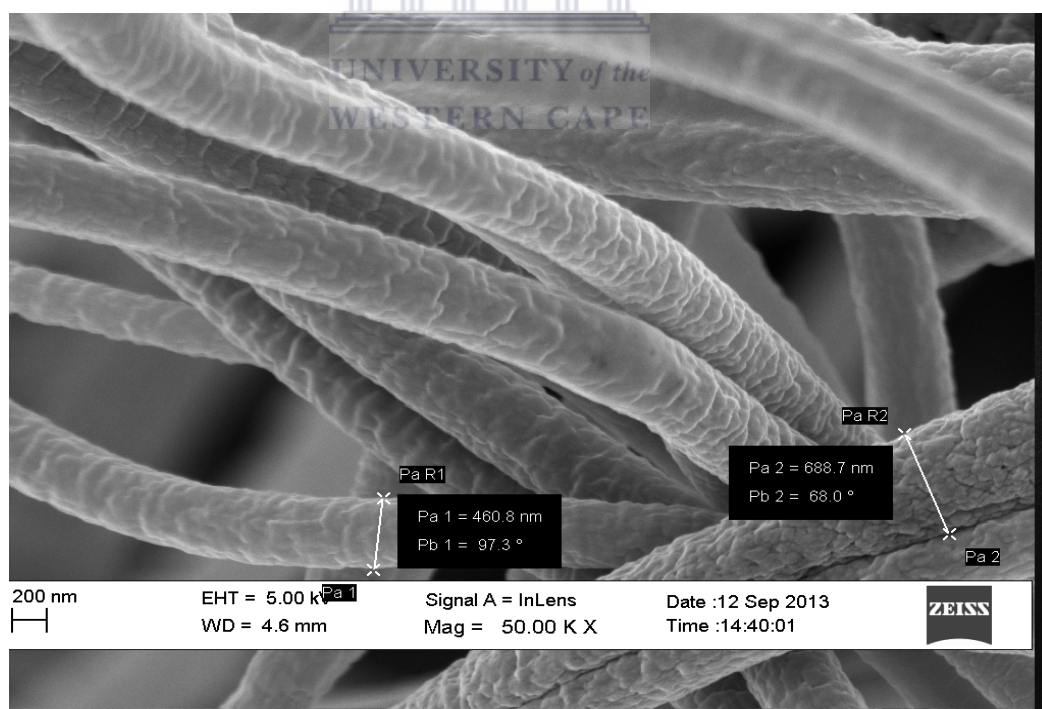


Figure 4.6: HRSEM image showing the morphology of the EF-03 nanofibres spun from the 10 wt% PAN/DMF sol-gel

From the HRSEM images, (see Figures 4.4 – 4.6) distinct changes in the morphological appearance of the fibres can be observed. As the concentration increased the fibre diameter increased as well. The morphology of the fibres also appeared to change from a smooth to a rougher surface. The results coincide with He *et al.*, (2008) findings that proposed fibre diameter to be dependent on the solution concentration.

The effect of solution concentration is presented in Figure 4.7. It illustrates the relationship between the polymer solution concentration and the electrospun polymer fibre diameter. The sol-gel was pumped to the spinneret with a flow rate of 2 mL/h in all cases.



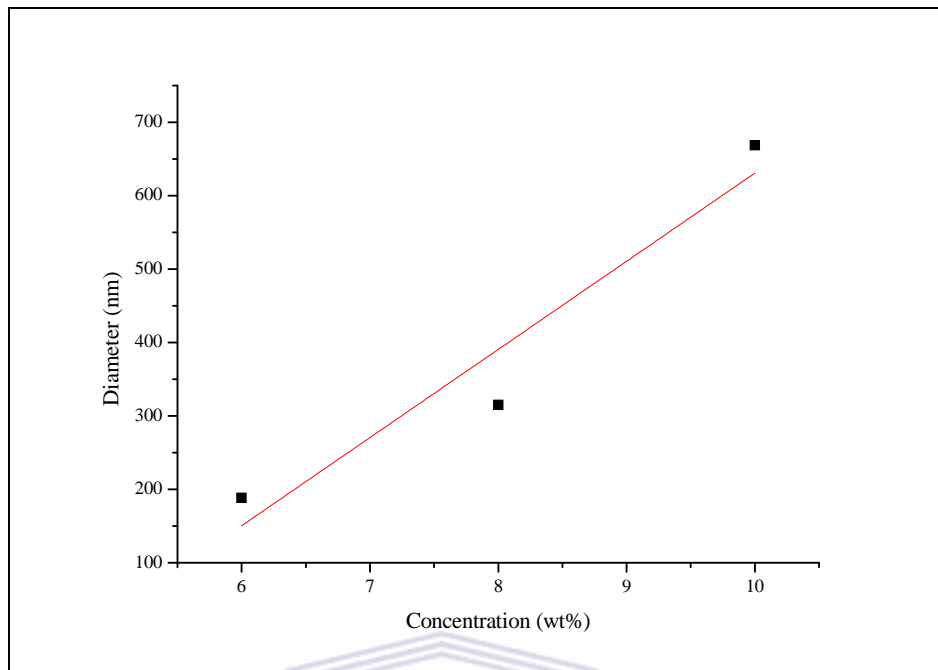


Figure 4.7: The effect of increased polymer concentrations at 6, 8 and 10 wt% on the fibre diameter (n=3)

The graph (see Figure 4.7) shows a fairly linear correlation between polymer concentration and fibre diameter. The graph shows how the fibre diameter increased as the polymer solution concentration increased in the sol-gel blend.

The higher magnification images of the different polymer concentrations displayed variations in the uniformity of the fibres. From the results it is evident that the average fibre diameter (see Figure 4.7) increased with increasing polymer concentration. The diameter of the electrospun nanofibres increased from 174 nm - 188.3 nm for the EF-01 fibres to 269.3 nm - 314.8 nm for the EF-02 fibres and 460.8 nm - 688.7 nm for the EF-03 fibres. The changes in the surface morphology could possibly be attributed to a lower evaporation rate of the solvent from the fibres in EF-03. As the polymer concentration increased the tip to collector distance over which the fibres were electrospun, as per section 3.3, prevented rapid drying of the jet fluid before the fibres were deposited on the collector plate.

## 4.2 Fourier Transform Infrared Spectroscopy (FTIR)

FTIR spectroscopy was performed to find the baseline vibrations of the PAN polymer. The FTIR spectral data was recorded on Perkin-Elmer equipment as described in section 3.7.5. Figure 4.8 shows the spectra of the electrospun PAN polymer fibres without TiO<sub>2</sub> to identify any changes in the composition of the polymer in further results that might have occurred after TiO<sub>2</sub> doping (see section 5).

In this case a 7 wt% PAN/DMF sol-gel was used to prepare fibres. The 7 wt% PAN polymer sol-gel is representative of the PAN/DMF formulation that was used throughout the study for all further samples. Based on the morphology of EF-01 (6 wt% PAN/DMF) and EF-02 (8 wt% PAN/DMF) fibres from the HRSEM analysis the 7 wt% PAN/DMF solution appeared the most suitable concentration for the fabrication of uniform polymer nanofibres, as it was the intermediate concentration between 6 wt% and 8 wt% PAN in DMF, and could produce fibres with an intermediate nanodiameter of around 200 nm.

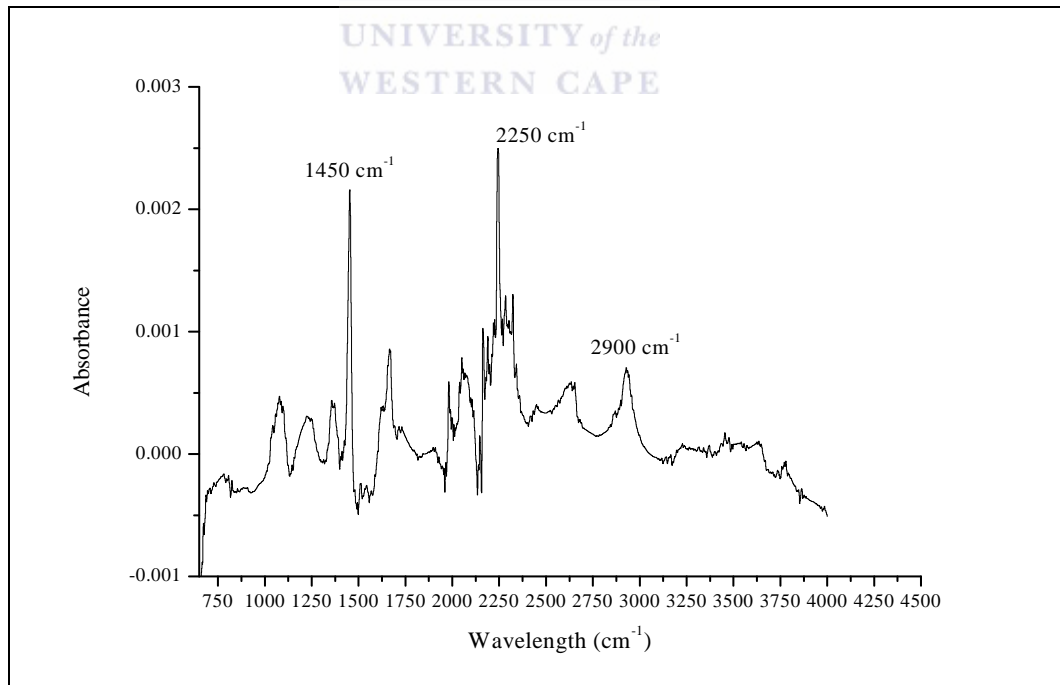


Figure 4.8: FTIR absorbance spectra of the blank 7 wt% PAN (EF-04) electrospun fibres over the mid-infrared region (4000 – 650 cm<sup>-1</sup>)

As Figure 4.8 shows, the FTIR absorption spectra displayed three major peaks. The peaks observed in the range  $3000 - 2850 \text{ cm}^{-1}$  are related to C-H stretching bands for aliphatic compounds. Triple bond stretching usually falls in the  $2500 - 2000 \text{ cm}^{-1}$  range and the peak at  $2250 \text{ cm}^{-1}$  in Figure 4.8 is related to  $(\text{C}\equiv\text{N})$  stretching. Bands in the  $2000 - 1500 \text{ cm}^{-1}$  region are usually assigned to  $(\text{C}=\text{C})$  and  $(\text{C}=\text{O})$  stretching. The peak at  $\sim 1660 \text{ cm}^{-1}$  is usually related to carbonyl stretching. Bands in the finger print region  $1500 - 650 \text{ cm}^{-1}$  can usually be associated with PAN skeletal vibrations. The peak at  $\sim 1460 \text{ cm}^{-1}$  can be ascribed to  $\text{CH}_2$  aliphatic vibrations (Stuart 2004; Hong *et al.*, 2006; Minceva-Sukarova *et al.*, 2012). The FTIR results coincided with reports by Minceva-Sukarova *et al.*, (2012) identifying the characteristic bands of the PAN polymer.

### 4.3 Thermal Gravimetric Analysis (TGA)

TGA was used to determine the optimum conditions for oxidative stabilisation and carbonisation of the PAN electrospun nanofibres. The thermal profile of the electrospun 7 wt% PAN polymer fibre is presented in Figure 4.9.

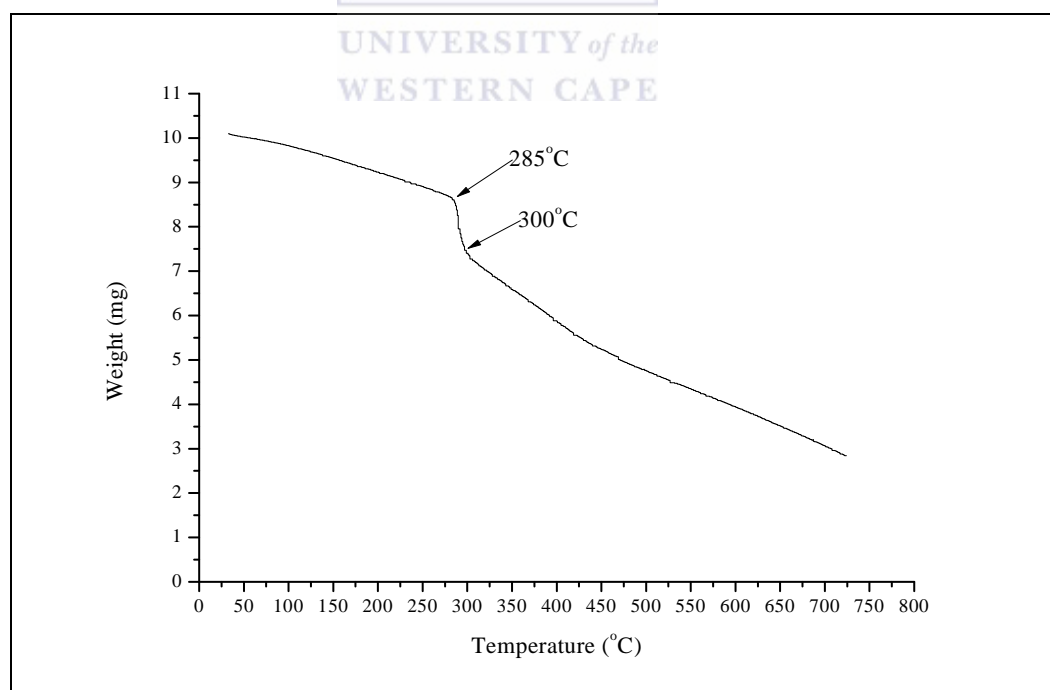


Figure 4.9: The TGA spectra of blank 7 wt% PAN (EF-04) polymer fibres up to  $800 \text{ }^{\circ}\text{C}$  in air

The spectrum in Figure 4.9 shows oxidative stabilisation to occur in the 150 °C – 300 °C temperature range. The mass loss that occurred from 10.1 mg to ~8.6 mg in the region is as a result of oxidative stabilisation of the polymer fibres heated in air at 5 °C per minute. During this thermal step the PAN-chains crosslink to form a more stable structure. The weight loss from 7.5 mg to ~5.1 mg between 300 and 450 °C is associated with the pre-carbonisation of the polymer and can be attributed to further aromatization of the fibre. The weight loss can be attributed to the loss of water upon cyclisation (Yusof and Ismail, 2012; Rahaman *et al.*, 2007). The TGA results coincide with reports by Rahaman *et al.*, (2007).

#### 4.4 Summary

In this chapter the basic characteristics of the PAN polymer sol-gel solution and subsequently the nanofibres made from it, were investigated to gain a better perspective of the fundamental properties of the polymer and the nanofibres. This facilitated the establishment of the optimum heating parameters that were required for the modification of the polymer. The HRSEM analysis of the morphology of EF-01 identified beaded fibre formation when the fibres were spun with the 6 wt% PAN/DMF solution. When the fibres were electrospun from the 8 wt% PAN/DMF solution the fibre morphology of EF-02, although uniform, was quite thick, with the average fibre diameter between 269 nm – 314 nm the fibres could not be considered nanofibres thus 7 wt% PAN/DMF was taken to be the best sol-gel formulation to use for further studies. The solution viscosity results coincided with literature. The relationship between fibre diameter and solution concentration was fairly linear. The results outlined the baseline characteristics of the fibres with no major divergence from literature.

The next chapter investigates the modification of the polymer fibres with TiO<sub>2</sub>.

## Chapter 5

### 5. Characterization of the TiO<sub>2</sub> doped electrospun fibres: Results and Discussion

#### 5.1 Introduction

The following chapter presents the results of the modifications of PAN electrospun nanofibres with TiO<sub>2</sub>. It is organized in manner to showcase the deposition of TiO<sub>2</sub> onto or loading inside the polymer fibres as well as the composite TiO<sub>2</sub> PAN fibre characteristics. Each aspect will briefly be highlighted and the parameters explained.

Research has seen a fair amount of studies performed on light induced mineralisation of organic pollutants using TiO<sub>2</sub>. In its free form the performance of titanium dioxide has been reported to increase the opacity of systems as well as reducing the radiation path lengths by light scattering. In order to achieve the maximum activity from the photocatalysts and avoid problems, it is crucial that these catalysts are immobilized on support materials (Manuel and da Silva, 2009). Literature has reported on a number of advances towards the immobilisation of photocatalysts on carbon constituents and other support systems (see section 2.4.4). By supporting TiO<sub>2</sub> on electrospun nanofibres with their large surface to volume ratio the limitations of TiO<sub>2</sub> in powder form such as solution turbidity, light scattering and loss of active surface area can be eliminated.

The aim of the study was to assess the photocatalytic ability of TiO<sub>2</sub> supported either inside or on top of electrospun nanofibres. The composite fibres were characterized to determine any changes to the fibre due to possible coordination interactions between TiO<sub>2</sub> and the PAN fibres using FTIR and RAMAN spectroscopy. Thereafter, any morphological changes to the fibres prepared by different TiO<sub>2</sub> loadings into or upon the polymer as well as the effect of thermal stabilisation or carbonisation of the fibres were investigated with electron microscopy. The crystalline phases of TiO<sub>2</sub> on the fibres were identified with XRD. Thereafter, thermal and chemical stability assessments of the composite fibres were performed through DSC and photolysis of hydrogen peroxide.

Considering the proposed applications it was necessary to assess the chemical robustness of the photocatalytic fibers. This study also determined the optimum catalyst loading by comparing the photocatalytic activity of the composite TiO<sub>2</sub> PAN fibres at different loadings by means of a photodegradation study using MB as model organic pollutant, which is set out in Chapter 6.

### **5.1.1 Characterization of the composite polymer fibres**

The photocatalytic composite fibres were electrospun from a 7 wt% PAN/DMF solution which was found to be the optimum polymer sol-gel concentration. It facilitated narrow fibre diameters and lower bead densities when compared with 6 or 8 wt% electrospun PAN nanofibres (See section 4.1.2).

The effect of admixing powdered commercial TiO<sub>2</sub> P25 into the 7 wt% PAN/DMF sol-gel on the properties of the composite electrospun nanofibre will be reported in this section. The composite fibres were prepared as set out in section 3.5.1. After the commercial powder TiO<sub>2</sub> was added to the sol-gel, the sol-gel was vortex mixed for 1 hour for adequate dispersion of the TiO<sub>2</sub>. When commercial powder TiO<sub>2</sub> catalyst was mixed into and dispersed in the PAN/DMF sol-gel the solution whitened and opacified. This was due to the optical properties of TiO<sub>2</sub>. The TiO<sub>2</sub>/PAN/DMF solution was placed in a syringe which was connected horizontally to the capillary pump with an 18 gauge needle connected to the positive terminal of the high voltage power supply. The PAN sol-gel containing the TiO<sub>2</sub> was electrospun using conditions set out in Table 3.4 to produce the TiO<sub>2</sub> containing PAN composite nanofibres.

Four different TiO<sub>2</sub> loadings were electrospun from the TiO<sub>2</sub> infused 7 wt% PAN/DMF polymer sol-gel, 3 wt% (EF-04a), 5 wt% (EF-04b), 7 wt% (EF-04c) and 10 wt% (EF-04d) TiO<sub>2</sub> was added (see Table 3.5). The samples were assigned, in wt%, according to the calculated amount of TiO<sub>2</sub> which was dissolved in the 7 wt% PAN/DMF solution (see section 3.5.1). The EF-04 series of nanofibres were characterised by HRSEM and TEM according to the procedures described in section 3.7.2.1 and 3.7.2.3.

### 5.1.1.1 Morphology of EF-04a (3 wt% TiO<sub>2</sub> in 7% PAN/DMF)

The following section investigates the effect of admixing 3 wt% of TiO<sub>2</sub> with 5 g of the 7 wt% PAN/DMF sol-gel on the morphology of composite electrospun fibres as set out in section 3.5.1. The HRSEM images of EF-04a (see Table 3.5) can be seen in Figures 5.1 - 5.2.

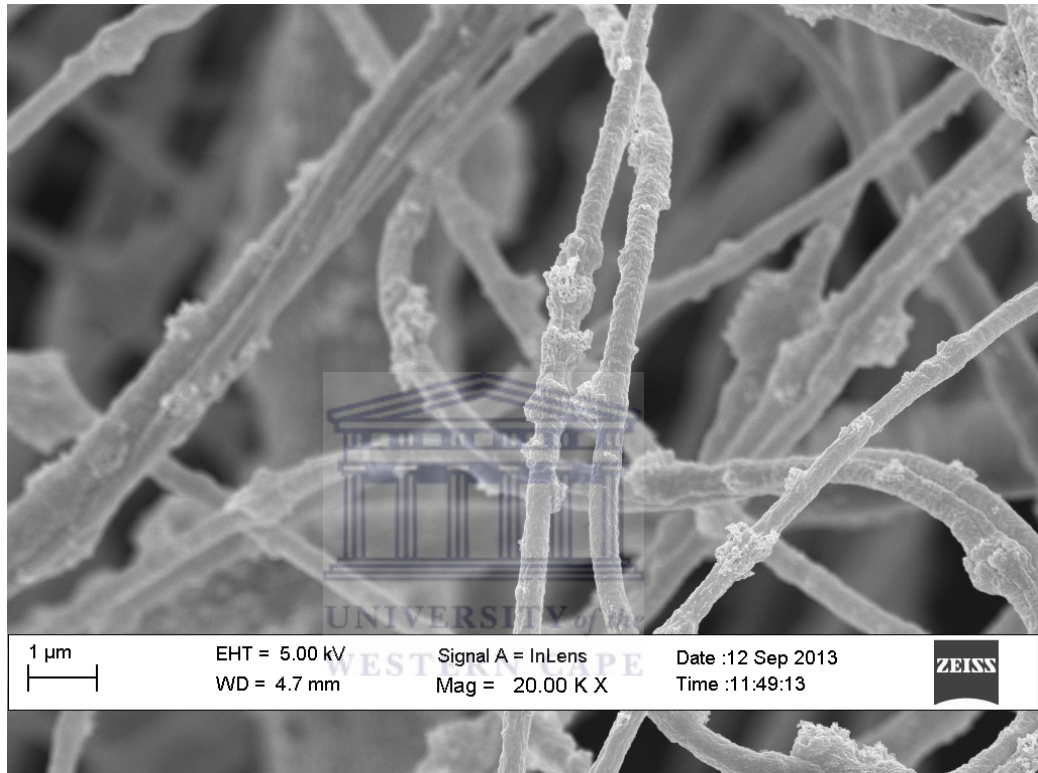


Figure 5.1: HRSEM image of EF-04a showing the TiO<sub>2</sub> catalyst distribution across the PAN fibres' interface (3 wt% TiO<sub>2</sub> in 7% PAN/DMF)

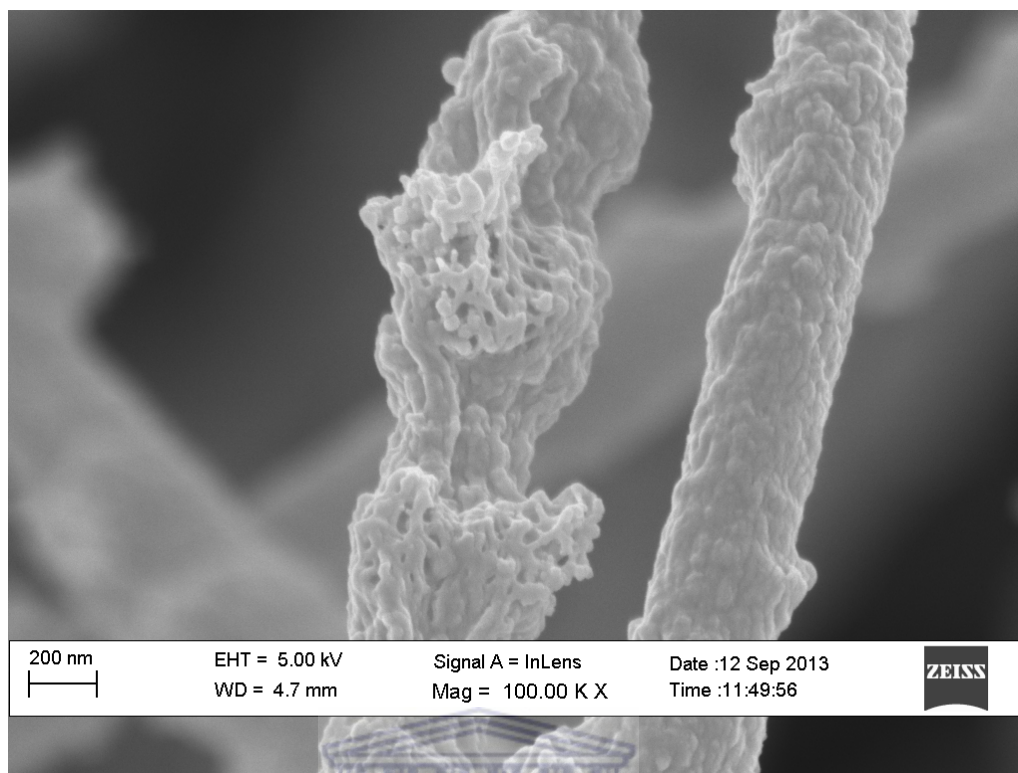


Figure 5.2: HRSEM image showing where the  $\text{TiO}_2$  catalysts breach the surface of EF-04a (3 wt%  $\text{TiO}_2$  in 7% PAN/DMF)

Figures 5.1 and 5.2 shows the HRSEM images of EF-04a (3 wt%  $\text{TiO}_2$  in 7 wt% PAN/DMF), the catalyst appeared to be well dispersed in the PAN nanofibres. As per Figure 5.2 the catalyst appears to be embedded in the fibre and seems to be concentrated around the beaded areas of the filament. The catalyst did not appear to form thin films across the fibre surface instead small clusters appeared to be prevalent in the beaded sections of the fibre. The HRSEM image (see Figure 5.1) showed bead formation to be prevalent in the  $\text{TiO}_2$  containing electrospun fibres. The fibre diameter is approximately 400 nm. The  $\text{TiO}_2$  catalyst loading appears to have influenced the morphology as well as bead density of the PAN fibres. This could be attributed to an increased charge density on the droplet before it accelerated across the electrostatic interface onto the collector plate.

#### 5.1.1.2 Morphology of EF-04b (5 wt% $\text{TiO}_2$ in 7% PAN/DMF)

The following section investigates the effect of admixing 5 wt% of  $\text{TiO}_2$  into the 7 wt% PAN/DMF sol-gel on the composite electrospun fibre as set out in section

3.5.1. Figures 5.3 and 5.4 shows the HRSEM images of the ES-04b (5 wt% TiO<sub>2</sub> in 7 wt% PAN/DMF) nanofibres (see Table 3.5).

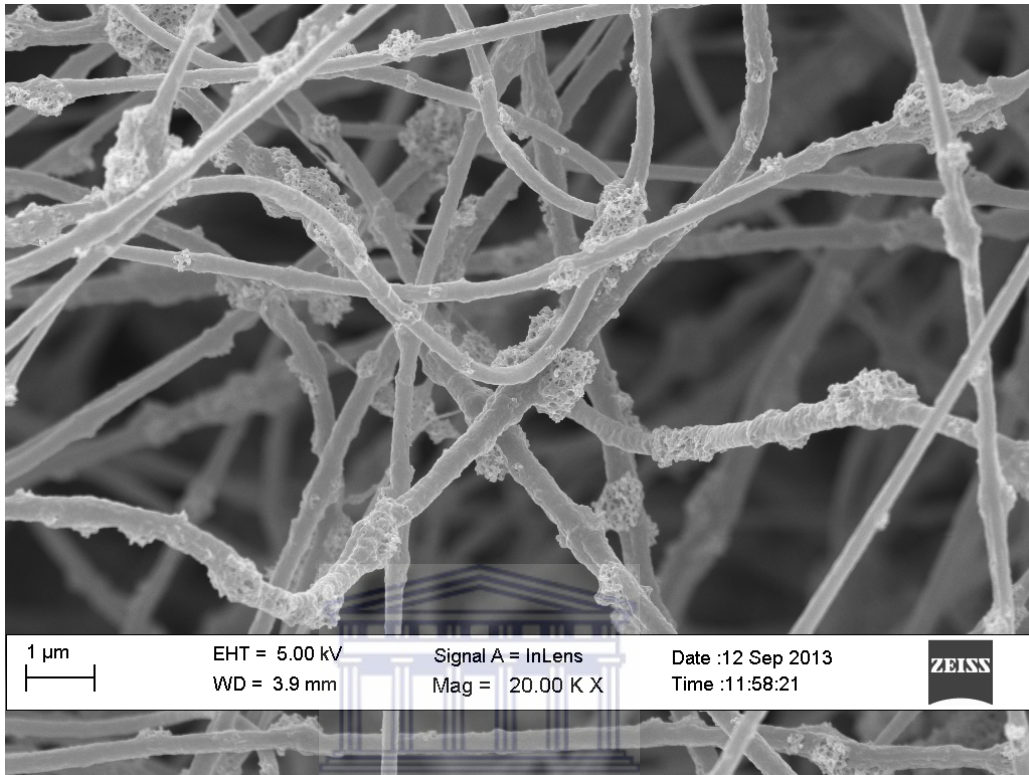


Figure 5.3: HRSEM image of EF-04b showing the TiO<sub>2</sub> catalyst distribution across PAN fibres' interface (5 wt% TiO<sub>2</sub> in 7% PAN/DMF)

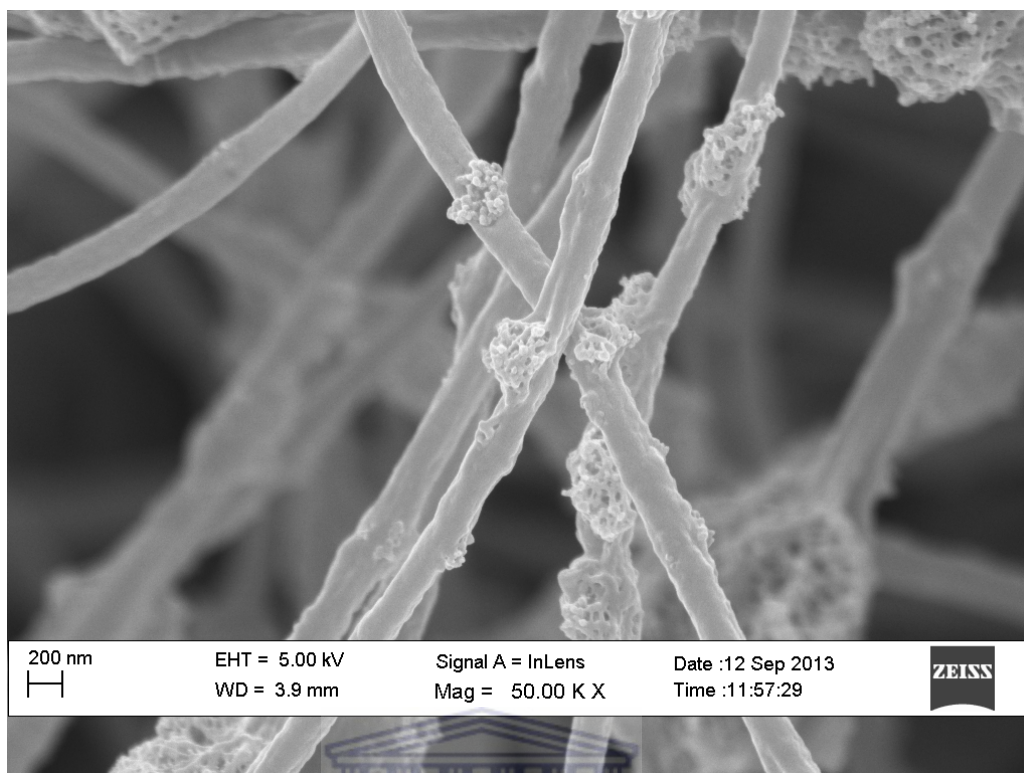


Figure 5.4: HRSEM image showing the bead morphology of EF-04b

The images (see Figure 5.3 and 5.4) of EF-04b fibres showed an increase in the bead size and density on the electrospun fibres. Compared to EF-04a the catalyst appeared more dispersed as the catalyst loading was increased and the fibre slightly narrower, with a diameter of approximately 300 nm.

#### 5.1.1.3 Morphology of EF-04c (7 wt% TiO<sub>2</sub> in 7% PAN/DMF)

The following section investigates the effect of admixing 7 wt% of TiO<sub>2</sub> into 7 wt% PAN/DMF sol-gel on the composite electrospun fibre as set out in section 3.5.1. Figures 5.5 and 5.6 show the HRSEM images of the EF-04c (7 wt% TiO<sub>2</sub> in 7 wt% PAN/DMF) nanofibres (see Table 3.5).

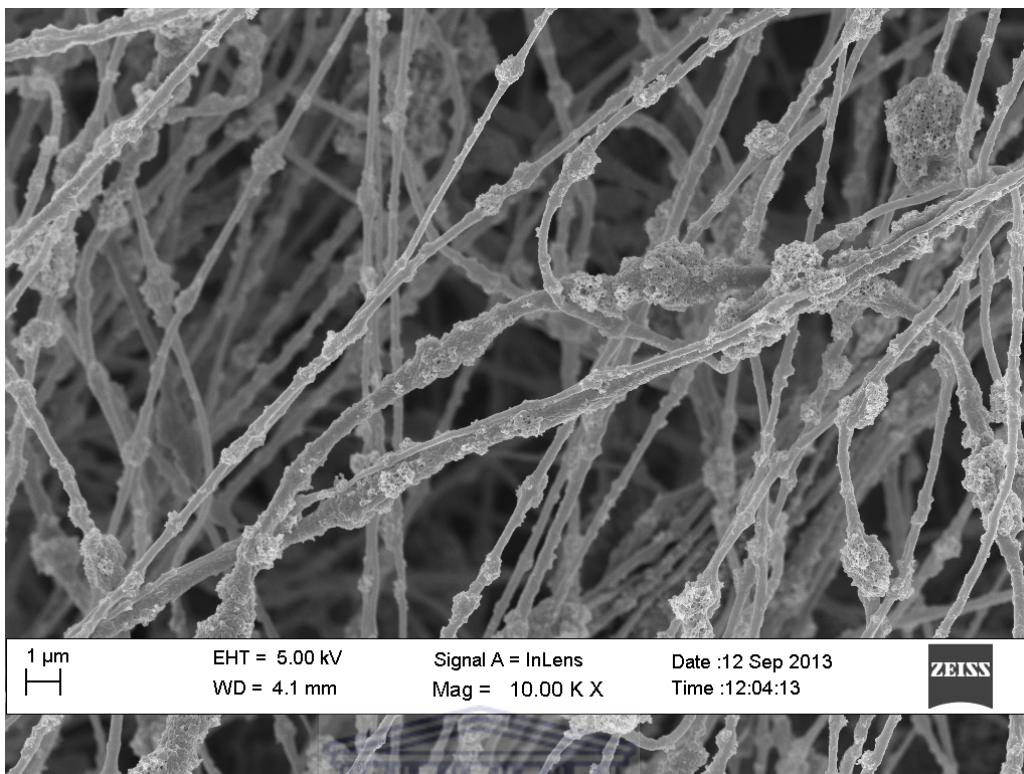


Figure 5.5: HRSEM image of EF-04c showing the TiO<sub>2</sub> catalyst distribution across PAN fibres' interface (7 wt% TiO<sub>2</sub> in 7% PAN/DMF)

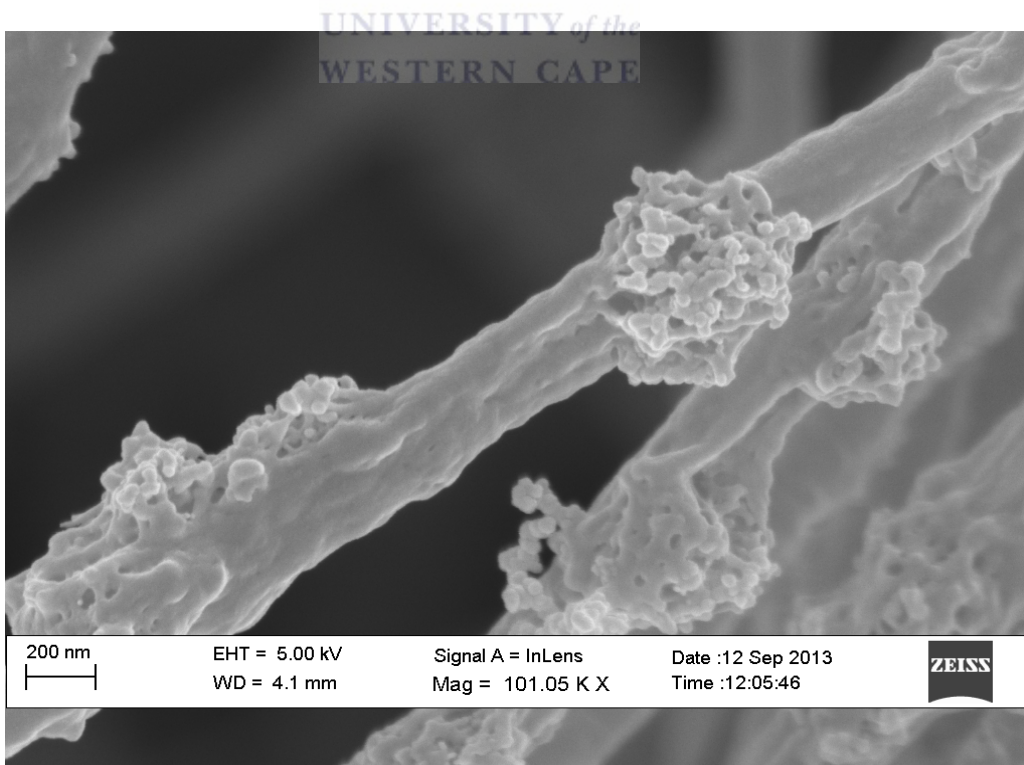


Figure 5.6: HRSEM image showing the bead morphology of EF-04c

The HRSEM images for EF-04c showed high density bead formation on the fibres (see Figure 5.5). Compared to EF-04b in Figure 5.4 the clusters appear larger in size. The image in Figure 5.6 showed the clusters to be where the catalysts breached the surface of the fibres it also shows the catalyst clustered in areas where the beads were situated. Bead-on-string formation also appeared to increase along with size of the beads (see Figure 5.5). The bead morphology appeared to be more porous and the fibre diameter to be approximately 320 nm (see Figure 5.6).

#### 5.1.1.4 Morphology of EF-04d (10 wt% TiO<sub>2</sub> in 7% PAN/DMF)

The following section investigates the effect of admixing 10 wt% of TiO<sub>2</sub> into 7 wt% PAN/DMF sol-gel on the composite electrospun fibre as set out in section 3.5.1. Figures 5.7 and 5.8 show the HRSEM images of the EF-04d (10 wt% TiO<sub>2</sub> in 7 wt% PAN/DMF) nanofibres (see Table 3.5). TEM was performed to investigate how the catalyst was dispersed inside the fibres and can be seen in Figure 5.9.

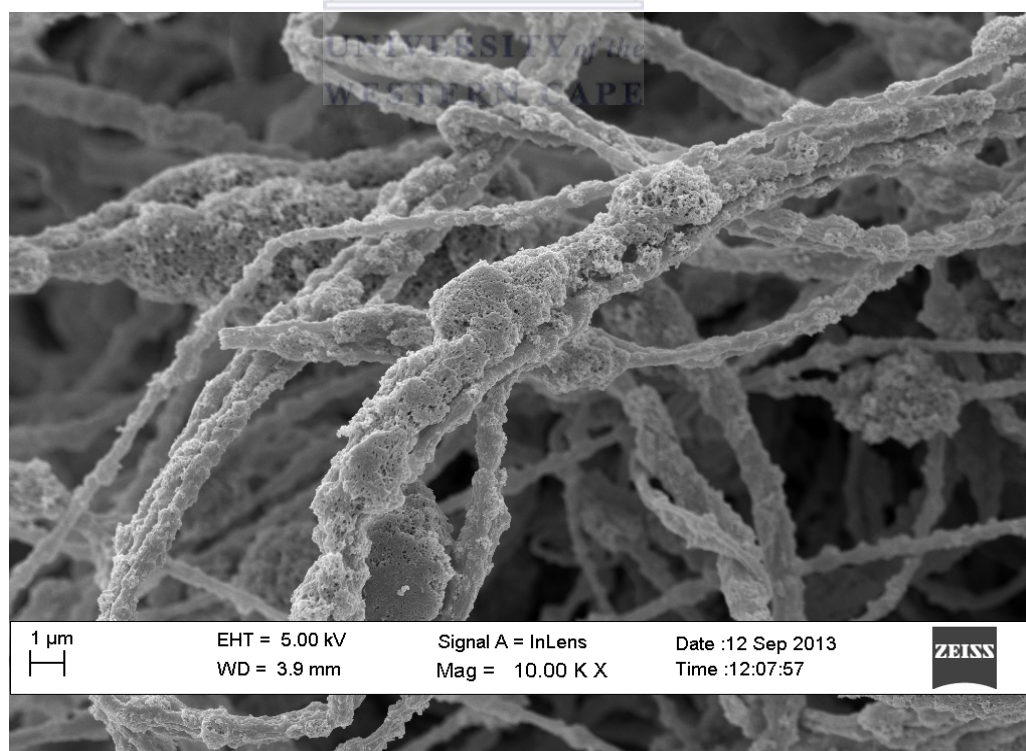


Figure 5.7: HRSEM image of EF-04d showing the TiO<sub>2</sub> catalyst distribution across PAN fibres' interface (10 wt% TiO<sub>2</sub> in 7% PAN/DMF)

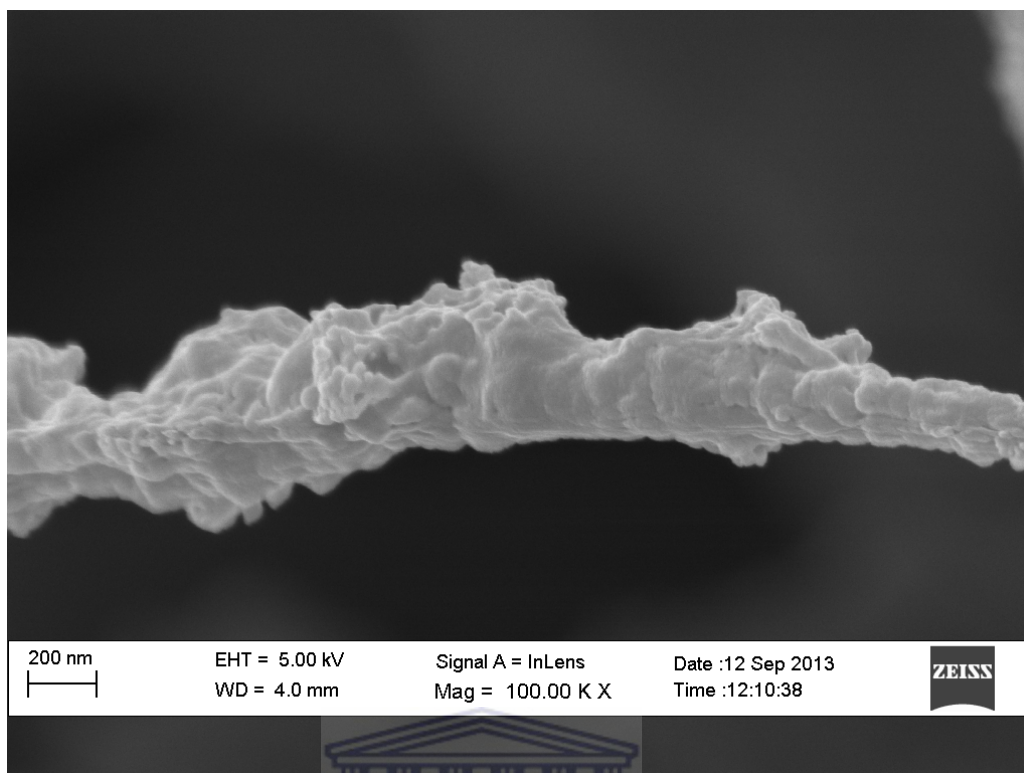


Figure 5.8: HRSEM image showing the morphology of EF-04d (10 wt% TiO<sub>2</sub> in 7 wt% PAN/DMF)

The higher catalyst loading in Figures 5.7 and 5.8 appears to transform the surface morphology of the fibres, from smooth filaments to rough, porous, irregular filaments with irregular fibre diameters (see Figure 5.7). Therefore to synthesize smooth nanofibres with TiO<sub>2</sub> embedded inside the PAN fibres the concentration of the TiO<sub>2</sub> needs to be maintained in the range of 3 – 5 wt%. Similar findings were reported by Khalil *et al.*, (2013) who synthesized a new class of poly lactic-co-glycolic acid nanofibres containing silver nanoparticles.

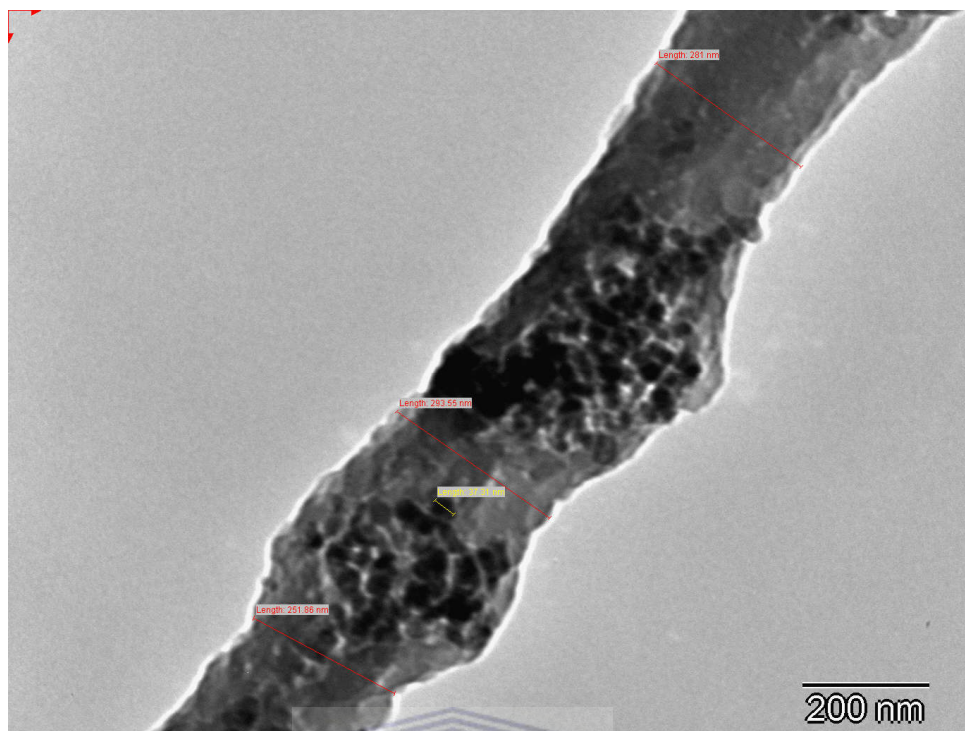


Figure 5.9: TEM image showing the dispersion of TiO<sub>2</sub> inside EF-04d (10 wt% TiO<sub>2</sub> in 7% PAN/DMF)

From the Transmission Electron Microscope (TEM) image of EF-04d (see Fig. 5.9) it is clear that the catalyst is embedded and dispersed inside the fibre and not merely deposited on the surface of it even at high TiO<sub>2</sub> loading. EF-04d was imaged by TEM as it had the highest TiO<sub>2</sub> loading. It also indicates that TiO<sub>2</sub> was loaded without any chemical and structural modifications into the PAN polymer matrix. This coincides with reports by Patel *et al.*, (2007) and Khalil *et al.*, (2013).

### 5.1.2 Energy Dispersive X-ray Spectroscopy (EDS)

In order to determine the TiO<sub>2</sub> loading inside the EF-04 series electrospun nanofibres EDS analysis had to be carried out as set out in section 3.7.2.2. The EDS analysis should also give an indication of the effectiveness of the loading procedure in terms of the distribution of the commercial powder TiO<sub>2</sub> across the fibres. The TiO<sub>2</sub> loading was determined as set out in section 3.5.1. The EDS analysis was performed on random spots on sections of 500 μm square in size of the electrospun nanofibres. The data of titanium distribution across the EF-04 series (see Table 3.5) electrospun nanofibres is given in Table 5.1. The results

give the partial-qualitative composition of the EF-04 series of electrospun nanofibres, which respectively theoretically had 3, 5, 7 or 10 wt% TiO<sub>2</sub> incorporated into the 7 wt% PAN/DMF.

Table 5.1: EDS data of the wt% of Ti across the EF-04 series electrospun nanofibres (n=1)

<b>Element wt%</b>	<b>EF-04a 3 wt%</b>	<b>EF-04b 5 wt%</b>	<b>EF-04c 7 wt%</b>	<b>EF-04d 10 wt%</b>
<b>C</b>	71.2	60.4	35.0	29.9
<b>O</b>	18.6	20.0	22.3	25.8
<b>Ti</b>	10.3	19.6	42.7	44.3
<b>Total:</b>	100	100	100	100

The EDS analysis (see Table 5.1) of EF-04 series electrospun nanofibres performed over a 500 µm square area confirmed the increasing trend in loading of TiO<sub>2</sub>. The results indicate that carbon and TiO<sub>2</sub> are the principle components of the EF-04 series electrospun nanofibres. The EDS data for the EF-04 series nanofibres does not appear to coincide with the theoretical loading of the fibres however considering the complete evaporation of DMF from the PAN polymer the actual loading of Ti increases by a factor of 14.29. Therefore by calculation, the theoretical loading of Ti on the fibres should be as follows: EF-04a was 43 wt%, EF-04b 71 wt%, EF-04c 100 wt% and EF-04d 143 wt%. Interpreting the EDS data, the actual loading of Ti obtained on the EF-04 series fibres was less than 50% of the calculated theoretical loading. The wt% of Ti on EF-04a was 10.25 wt%, EF-04b was 19.57 wt%, EF-04c was 42.72 wt% and EF-04d was 44.3 wt%. The qualitative EDS data thus just showed a positive correlation between the theoretical and actual loading.

### 5.1.3 X-Ray Diffraction Spectroscopy (XRD)

The XRD technique was used to identify the crystal phases of the commercial anatase TiO<sub>2</sub> nanoparticles incorporated in the EF-04b electrospun nanofibres. The spectra were compared to a typical spectrum of anatase and titanium oxide (see notes on Figure 3.4). The x-ray diffraction pattern of EF-04b shown in Figure

5.10 is representative of the EF-04 series electrospun nanofibres as all FTIR spectra were similar.

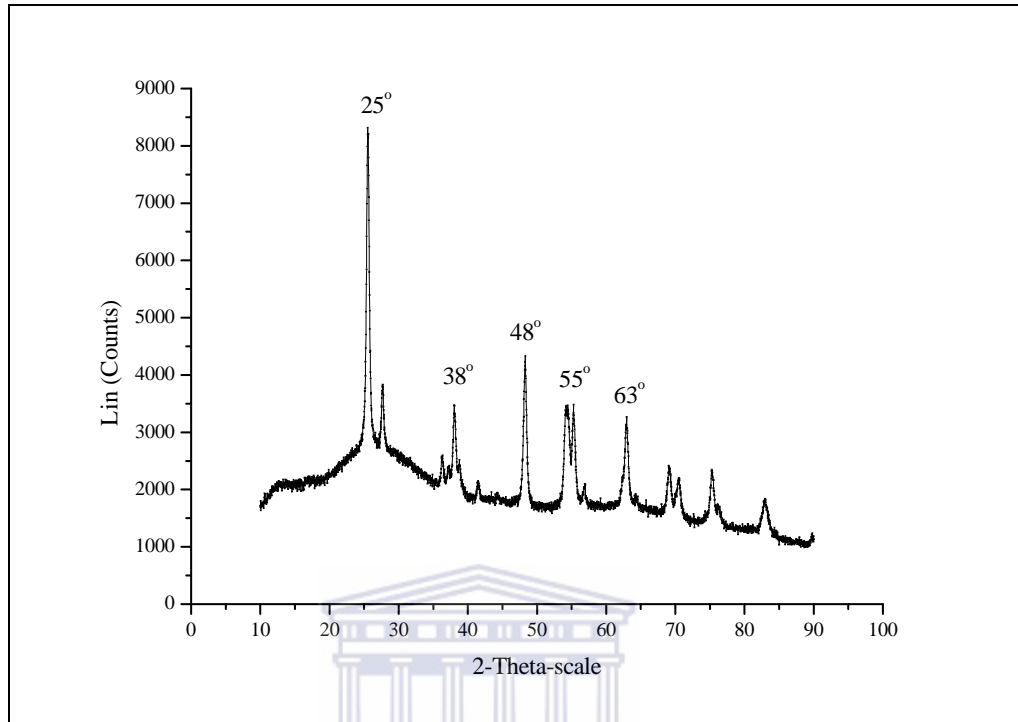


Figure 5.10: X-ray crystallographic analysis of the commercial anatase  $\text{TiO}_2$  embedded in the EF-04b electrospun PAN nanofibres (5 wt% powdered commercial  $\text{TiO}_2$  loading)

A reference XRD spectrum from literature, showing peaks at  $17^\circ$  and  $29.3^\circ$  for pure PAN fibres is shown in Figure 2.10. In Figure 5.10 the XRD spectrum of PAN and  $\text{TiO}_2$  shows strong diffraction peaks at  $25^\circ$ ,  $38^\circ$ ,  $48^\circ$ ,  $55^\circ$  and  $63^\circ$ . The XRD pattern of commercial anatase  $\text{TiO}_2$  containing electrospun fibres corresponded with the standard spectrum of  $\text{TiO}_2$  anatase phase (see section 3.7.3). The peaks confirmed the crystalline phase in sample EF-04b to be anatase. High intensity peaks identify crystalline nanoparticles which were incorporated into the EF-04 electrospun nanofibres. Not much peak broadening of  $\text{TiO}_2$  phase was observed, long range order was observed in the diffraction pattern that identified the anatase crystalline phase. These findings were confirmed by reports by Theivasanthi and Alagar, (2013).

### 5.1.4 Raman spectroscopy

The incorporation of powder  $\text{TiO}_2$  in electrospun PAN polymer fibres was examined with Raman spectroscopy to identify any changes to the polymer molecular structure. Figure 5.11 shows a Raman spectrum of EF-04b (5 wt%  $\text{TiO}_2$  in 7 wt% PAN/DMF). The spectrum is representative of the EF-04 series electrospun nanofibres and identified three main Raman bands at  $\sim 500 \text{ cm}^{-1}$ ,  $1450 \text{ cm}^{-1}$  and  $1525 \text{ cm}^{-1}$ .

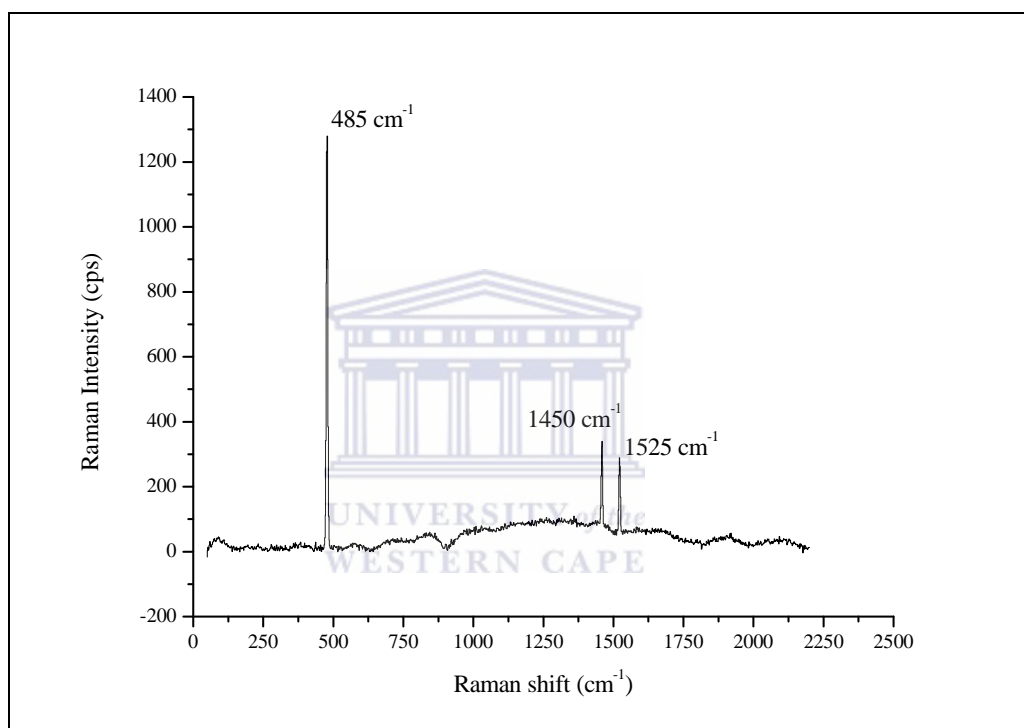


Figure 5.11: Raman spectra of EF-04b, representative of the EF-04 electrospun nanofibres

The peak at  $485 \text{ cm}^{-1}$  corresponds to Ti-O-Ti vibration of anatase phase (Hu *et al.*, 2007). Bands in the fingerprint region in Raman spectra, below  $650 \text{ cm}^{-1}$ , usually arise because of metal organic groups, inorganic groups or lattice vibrations (Smith and Dent, 2005). The peak at  $1525 \text{ cm}^{-1}$  corresponds to  $2000 - 1500 \text{ cm}^{-1}$  region where double bonds occur and can be attributed to (-C=C-) double bonds, the corresponding peak at  $1450 \text{ cm}^{-1}$  can be attributed to carbon-carbon vibrations (Smith and Dent, 2005). Senthilnathan and Philip (2010) reported crystalline anatase  $\text{TiO}_2$  to have six fundamental modes of vibrations correspondingly at 144

$\text{cm}^{-1}$ ,  $197 \text{ cm}^{-1}$ ,  $397 \text{ cm}^{-1}$ ,  $518 \text{ cm}^{-1}$  and  $640 \text{ cm}^{-1}$ . Compared to literature there appears to be a shift in the  $\text{TiO}_2$  peak in Figure 5.11 but the cause of the shift in vibration at  $485 \text{ cm}^{-1}$  is unclear.

### 5.1.5 Fourier Transform Infrared Spectroscopy (FTIR)

FT-IR spectroscopy was performed to obtain evidence of any bonding interaction between the polymer and  $\text{TiO}_2$  nanoparticles. The spectrum shown in Figure 5.12 of EF-04b is representative of the EF-04 electrospun nanofibres.

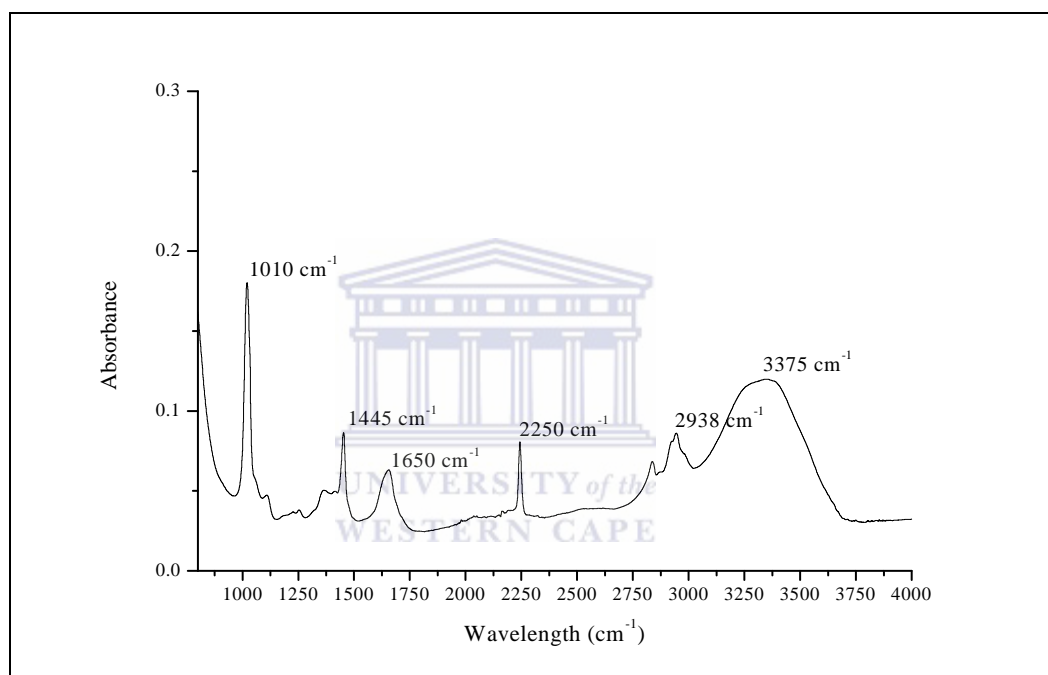


Figure 5.12: FTIR absorbance spectra of EF-04b over the mid-infrared region ( $4000 - 650 \text{ cm}^{-1}$ )

The reference FTIR spectrum for  $\text{TiO}_2$  P25 can be found in Section 2.4.1 (see Figure 2.16). The spectrum of EF-04b is shown in Figure 5.12. The broad peak at  $3375 \text{ cm}^{-1}$  and the peak at  $1650 \text{ cm}^{-1}$  are due to OH group stretching vibrations (Jensen *et al.*, 2005). The peak at  $1010 \text{ cm}^{-1}$  in the finger print region of EF-04b spectrum is attributed to the raw PAN fibre however the assignment of this peak is inconclusive (Minceva-Sukarova *et al.*, 2012). The FTIR spectra of the blank 7 wt% PAN fibre is given in chapter 4 (see Figure 4.8), if we compare the 2 spectra the peaks are somewhat different. Bonding interactions between the catalyst and

the polymer could not accurately be established as the existing FTIR library does not cover all the bonding information present in nanomaterials (Baudot *et al.*, 2010).

### 5.1.6 Photocatalytic electrospun nanofibres exposure to H<sub>2</sub>O<sub>2</sub> photolysis

The EF-04b electrospun nanofibres (5 wt% TiO<sub>2</sub> in 7 wt% PAN/DMF) were subjected to stability testing for 8 hours under the reaction conditions of UV photolysis of hydrogen peroxide, a process that generates hydroxyl radicals to simulate a high radical environment. The experiment was conducted by weighing out 4 samples of EF-04b of approximately 0.020 mg and placing the respective samples in a 100 mL 4 ppm H<sub>2</sub>O<sub>2</sub> solution as set out in section 3.6.2. The outcome of the prolonged exposure to the radical rich environment on the fibre structure can be seen from the FTIR spectra presented in Figure 5.13.

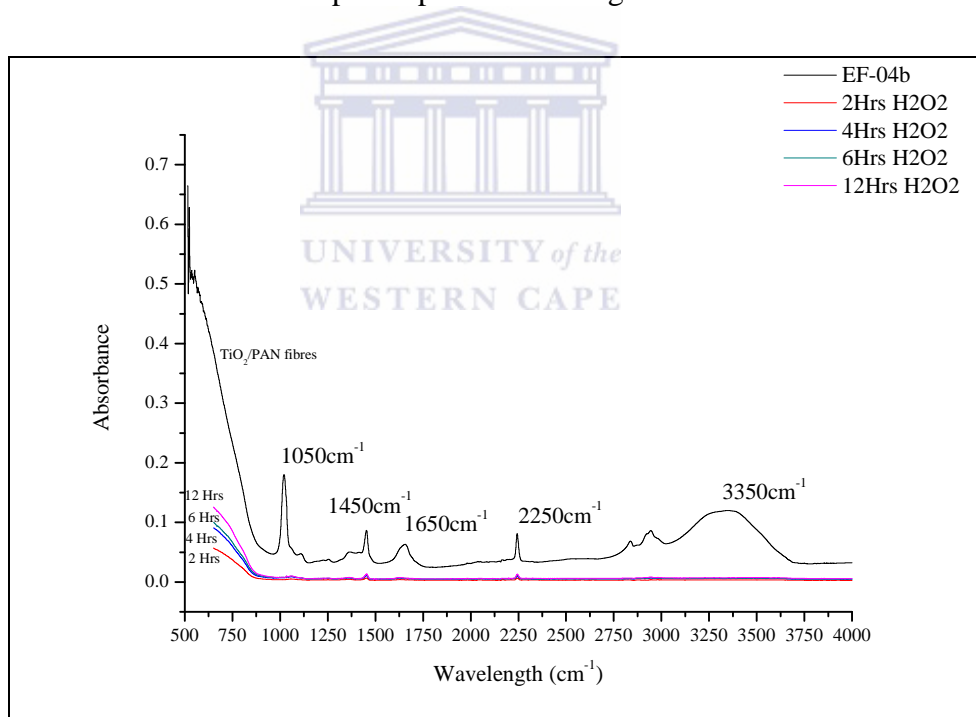


Figure 5.13: FTIR spectra of EF-04b (5 wt% TiO<sub>2</sub> in 7 wt% PAN/DMF) chemical stability under high radical environment produced by H<sub>2</sub>O<sub>2</sub> photolysis

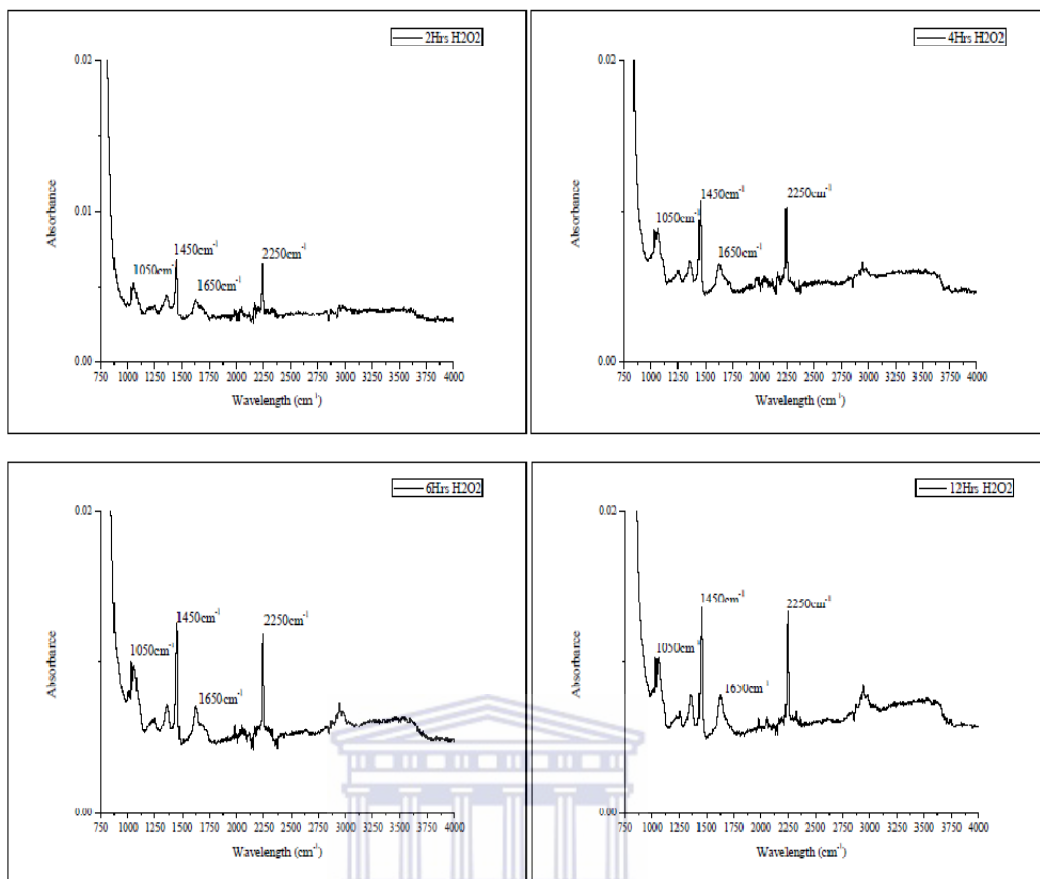


Figure 5.14: Individual spectra of EF-04b fibres after H<sub>2</sub>O<sub>2</sub> photolysis at 2, 4, 6 and 12 hours

The FTIR spectrum in Figure 5.13 shows the effect of the exposure of EF-04b electrospun nanofibres to the radical environment generated by H<sub>2</sub>O<sub>2</sub> photolysis. As the time of exposure increased the stretch in vibration intensities decreased. This can be attributed to the loss of elasticity by the fibres after radical exposure. The fibres immediately clumped up when they were removed from the H<sub>2</sub>O<sub>2</sub> solution for all fibres, though they were intact. Once the fibres dried they had lost most of their elasticity due to hydrolysis from H<sub>2</sub>O<sub>2</sub> radical attack, for all the different exposure times, showing that PAN is highly susceptible to free radical attack and, ultimately not stable in a free radical rich environment. This motivates for the carbonisation of the composite fibres as set out in section 5.3.

### 5.1.7 Differential Scanning Calorimetry (DSC)

DSC analysis was performed on the 7 wt% PAN/DMF electrospun nanofibres to determine if the addition of TiO<sub>2</sub> to the polymer fibre has any affect on the

thermal stability of the fibres. Figure 5.15 shows the DSC spectra of fibres prepared with 7 wt% PAN/DMF by itself before TiO<sub>2</sub> incorporation compared to EF-04b electrospun nanofibres containing 5 wt% TiO<sub>2</sub>.

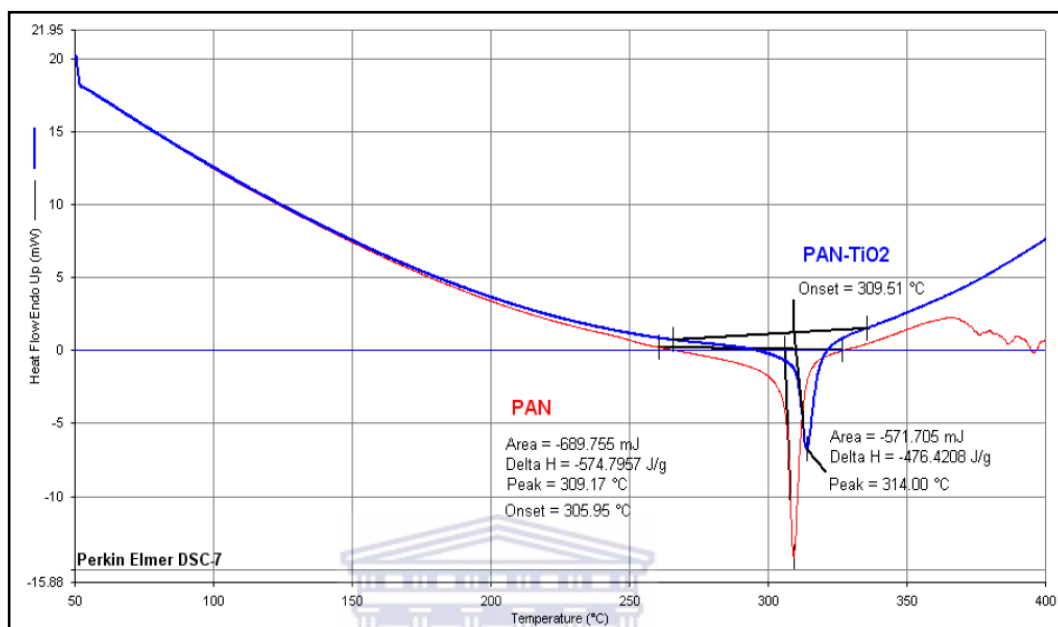


Figure 5.15: DCS spectra of the 7 wt% PAN/DMF and EF-04b electrospun nanofibres

The DSC curve for PAN nanofibres without TiO<sub>2</sub> given in Figure 5.15 shows an exothermic peak at ~ 310 °C that was due to the cyclisation reaction that is a highly exothermic process. For EF-04b which contained 5 wt% TiO<sub>2</sub> the exothermic peak shifted to a higher temperature of ~ 314 °C but with a lower release rate. The peak area for EF-04b showed lower enthalpy during the cyclisation reaction. This was deduced from the peak area of the DSC curve for EF-04b. This could be attributed to decreased entropy on the EF-04b. TiO<sub>2</sub> appeared to add stability to the electrospun nanofibres through nitrile polymerisation. These findings coincide with reports by Moafi *et al.*, (2011).

## 5.2 Characterization of oxidatively stabilised composite nanofibres

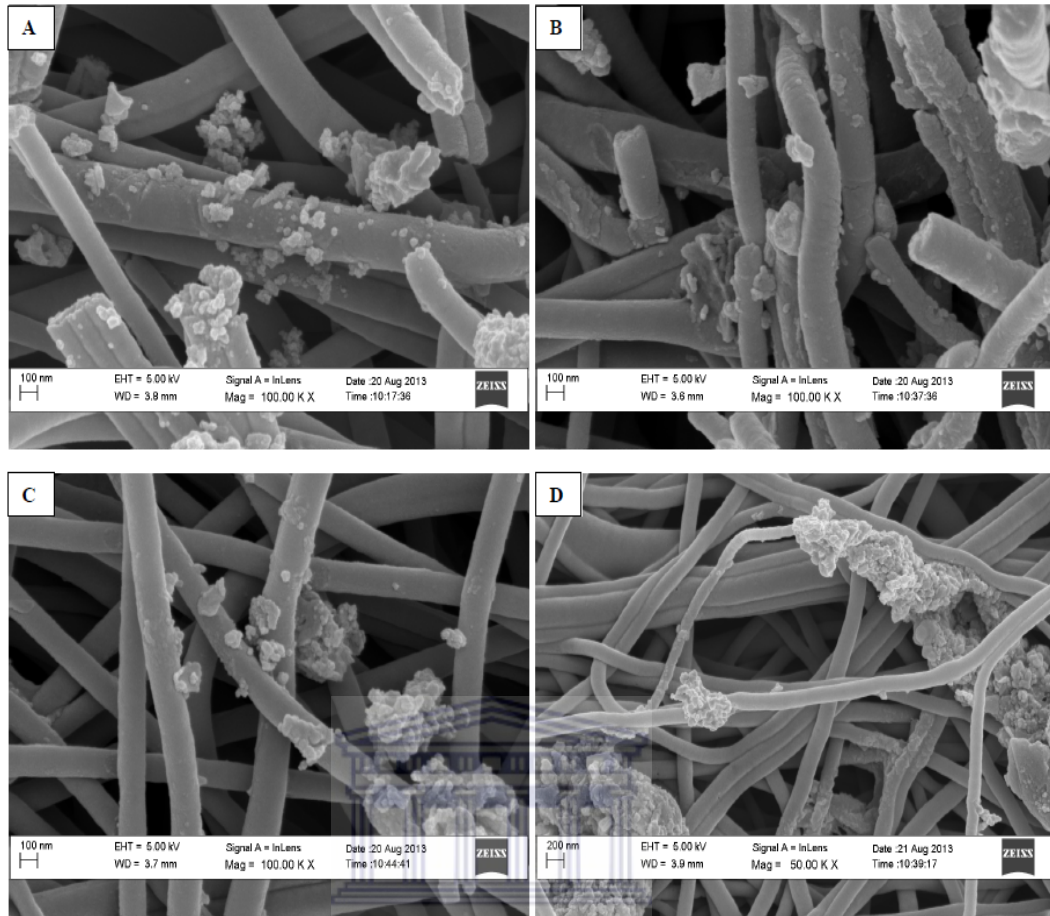
PAN polymer fibres are commonly used to synthesise high performance carbon nanofibres. The fibres can be transformed to carbon nanofibres under thermal conditions (see section 2.2). The following section details the thermally coated and stabilised EF-05 – EF-08 commercial PAN nanofibres (see Table 3.8) and

discusses possible influences of the thermal step, and TiO<sub>2</sub> coating procedure on the fibre stability and performance.

In order to stabilize the commercial PAN nanofibres and simultaneously coat them with TiO<sub>2</sub> the samples of EF-05 – EF-08 nanofibres had to be subjected to a heat treatment step (see Table 3.7). In order to coat the surface of the commercial PAN fibres with photocatalyst it required the atomistic deposition of TiO<sub>2</sub>. The effect of coating different loadings of TiO<sub>2</sub> on the surface of commercial PAN nanofibres was investigated to assess the mass % loading of catalyst on the fibres and also to determine the stability of the catalyst coated on the commercial PAN fibres. The results are presented in this section. The composites were prepared by coating the commercial PAN fibres with titanium oxy acac dissolved in methanol (see section 3.5.2). The fibres were loaded as follows 10 wt%, 15 wt%, 20 wt% and 30 wt%. The stabilisation of the commercial PAN fibres and the transformation of titanium oxy acac to TiO<sub>2</sub> were performed simultaneously under the stabilisation conditions. The fibres were stabilised by heating the commercial PAN fibres in air to 275 °C at 1 °C/min. The fibres were then stabilised in air for 1 hour at set temperature. The technique was adopted from Castaneda *et al.*, (2002) who used an ultrasonic spray pyrolysis process to deposit Titanium oxide thin films on Pyrex glass. The process was based on the chemical vapour deposition (CVD) process. However, in this study the process used to deposit TiO<sub>2</sub> on the commercial electrospun fibres resembled a thermal oxidation process where the titanium oxy acetylacetonate was thermally converted to TiO<sub>2</sub>.

### **5.2.1 Morphology of oxidatively stabilised composite nanofibres**

The EF-05 – EF08 nanofibres were prepared as outlined in section 3.5.2. Figure 5.16 shows the morphology of the different TiO<sub>2</sub> loadings coated on the EF-05 – EF-08 nanofibres, via thermal oxidation as determined with HRSEM.



UNIVERSITY of the

Figure 5.16: HRSEM images showing the oxidatively stabilised thermally coated  $\text{TiO}_2$  commercial PAN fibres at different concentrations, (A) EF-05 (10 wt% Ti oxy acac), (B) EF-06 (15 wt% Ti oxy acac), (C) EF-07 (20 wt% Ti oxy acac) and (D) EF-08 (30 wt% Ti oxy acac)

From Figure 5.16 the  $\text{TiO}_2$  appears to be better dispersed on EF-05 and EF-06 (10 and 15 wt% respectively). As the titanium oxy acac loading increased the  $\text{TiO}_2$  became more aggregated after the thermal coating process and resulted in cluster formation becoming more prevalent on EF-07 and EF-08.

Figure 5.17 shows the  $\text{TiO}_2$  formation that occurred on the nanofibres under the thermal conditions prescribed for the thermal coating and stabilisation of the commercial PAN nanofibres (see Table 3.7).

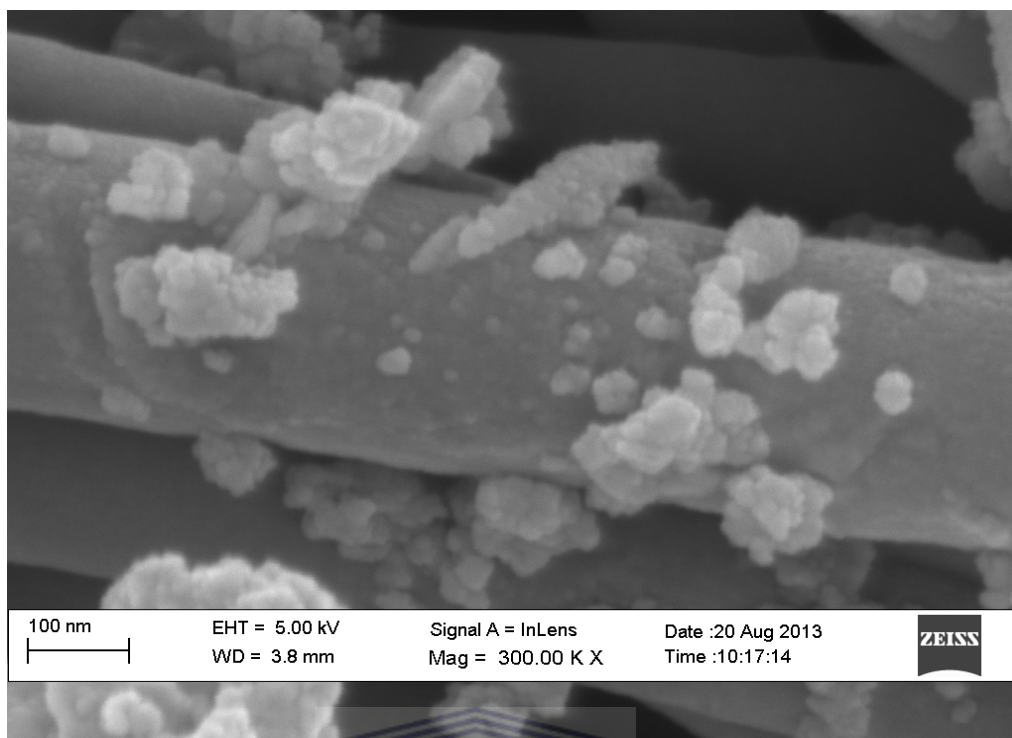


Figure 5.17: HRSEM image of EF-05 (representative of EF-05-EF-08 series fibres)

From the HRSEM image the morphology of the EF-05 nanofibres in Figure 5.17 shows the  $\text{TiO}_2$  to be deposited on the surface of the stabilised commercial PAN fibre forming the  $\text{TiO}_2$ /PAN composite fibre. Unlike the EF-04 series nanofibres where the commercial  $\text{TiO}_2$  was situated and distributed inside the fibre the nanoparticulates with aggregates of less than 50 nm up to 200 nm were randomly distributed across the surface of the fibres.

### 5.2.2 Energy Dispersive X-ray Spectroscopy (EDS)

In order to determine the actual amount of  $\text{TiO}_2$  loading thermally coated on top of the EF-05 – EF-08 series of electrospun nanofibres EDS analysis was carried out as set out in section 3.7.2.2. The EDS analysis should also give an indication of the effectiveness of the loading procedure in terms of the degree of distribution of the  $\text{TiO}_2$  on top of the fibres. The  $\text{TiO}_2$  loading was determined as set out in section 3.5.2. The EDS analysis was performed on random sections of the composite nanofibres. The data of  $\text{TiO}_2$  distribution across the EF-05-EF-08 series fibres (see Table 3.8) nanofibres is given in Table 5.2. The analysis was

performed over a 500  $\mu\text{m}$  square area of the sample. The results give the qualitative composition of the EF-05-EF-08 series composite nanofibres.

Table 5.2: EDS data of the wt% composition of EF-05, EF-06, EF-07 and EF-08 series nanofibres (n=1)

<b>Element wt%</b>	<b>EF-05 10 wt%</b>	<b>EF-06 15 wt%</b>	<b>EF-07 20 wt%</b>	<b>EF-08 30 wt%</b>
<b>C</b>	81.1	81.2	70.4	53.8
<b>O</b>	13.8	14.2	18.9	22.9
<b>Ti</b>	5.1	4.6	10.7	23.3
<b>Total:</b>	100	100	100	100

The EDS analysis (see Table 5.2) of EF-05 - EF-08 series composite nanofibres performed over a 500  $\mu\text{m}$  square area of the sample shows the loading of  $\text{TiO}_2$  on the commercial PAN nanofibres. The results indicate that carbon and  $\text{TiO}_2$  are the principle components of the EF-05 - EF-08 series electrospun nanofibres. The EDS data shows the  $\text{TiO}_2$  loading on the EF-05 - EF-08 series fibres to be inconsistent with the theoretical loading. The Ti wt% on EF-05 was 5.14 wt% EF-06 4.6 wt%, EF-07 10.7 wt% and EF-08 23.31 wt%. Loading  $\text{TiO}_2$  onto the commercial fibres resulted in lower loading of the  $\text{TiO}_2$  compared to the incorporation of powdered  $\text{TiO}_2$  into the electrospun PAN fibres (EF-04 series). Moreover the coatings were not uniform as the HRSEM showed.

Compared to the EF-04 series nanofibres where the powdered  $\text{TiO}_2$  catalyst was incorporated in the electrospinning solution lower loading was achieved on the EF-05 – EF-08 series nanofibres, where Ti oxy acac was used as precursor. The EDS data show the actual loading of Ti on the EF-05 – EF-08 fibres were approximately 50% of the theoretical loading. Electrospinning fibres from a PAN/DMF sol-gel containing  $\text{TiO}_2$  nanoparticles is also a much simpler and lower energy process than thermally coating commercial PAN nanofibres with Ti precursor.

### 5.2.3 X-Ray Diffraction Spectroscopy (XRD)

XRD was performed on EF-06 (15 wt% theoretical loading) to identify the crystal phases of the TiO<sub>2</sub> nanoparticles thermally coated on the commercial PAN nanofibres. The HRSEM image in Figure 5.16 showed cluster formation to be least prevalent in EF-06. The spectra were compared to a typical spectrum of anatase and titanium oxide (see section 3.7.3). The x-ray diffraction pattern for EF-06 is shown in Figure 5.18 as representative of all the coated fibres that were oxidatively stabilised.

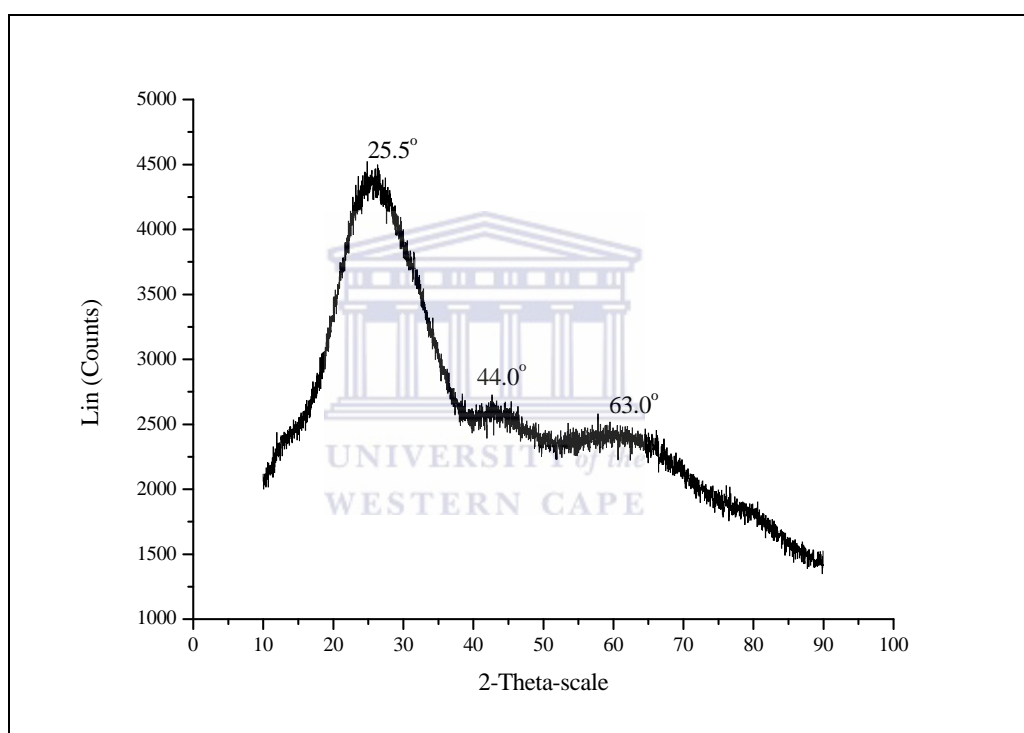


Figure 5.18: X-ray analysis of the sample EF-06 prepared under the oxidatively thermal stabilisation conditions

The X-ray diffraction pattern for EF-06 in Figure 5.18 shows a strong diffraction peak at  $\sim 25.5^\circ$ , the diffractogram also identified minor diffraction peaks at  $\sim 44.0^\circ$  and  $\sim 63^\circ$  peaks. These peaks correspond to the formation of pre-graphitic carbon (see Figure 2.10) (Lee *et al.*, 2012). Since EDS data shows the presence of TiO<sub>2</sub> it is likely that the short range order of the TiO<sub>2</sub> nanoparticles could not be resolved by XRD because of peak broadening and overlaps with graphitic peaks (Wang *et al.*, 2013). The HRSEM showed the TiO<sub>2</sub> nanoparticles to be aggregated

in clusters in the range of 50 – 200 nm in size. In Figure 5.10 the anatase phase was clearly visible in XRD of the TiO<sub>2</sub> incorporated electrospun nanofibres whereas for the thermally treated samples no long range order of the titanium phase was observed.

#### 5.2.4 Fourier Transform Infrared Spectroscopy (FTIR)

FT-IR spectroscopy was performed on EF-08 to identify any possible bonding interaction between the oxidatively stabilised commercial PAN fibres with the coating of TiO<sub>2</sub> nanoparticles. Cautious assignments of the IR bands of EF-08 (30 wt% TiO<sub>2</sub> on PAN) in the 4000 – 650 cm<sup>-1</sup> spectral region is given in Table 5.3.

Table 5.3 FTIR absorbance of EF-08 in the 4000 – 650 cm<sup>-1</sup> region

Absorbance (cm <sup>-1</sup> )	Assignment
3500 -3300	OH - stretching
3000	CH - stretching
2250	Nitrile - stretching
1700	conjugated C=N stretching
1580	D - bands
1375	G- bands
1250	CH - group vibrations

The absorption peaks in the 3300 – 3500 cm<sup>-1</sup> region can be ascribed to OH stretching, the peak at 3000 cm<sup>-1</sup> was ascribed to CH stretching, the decrease in intensity of the nitrile absorption band at 2250 cm<sup>-1</sup> was due to the chemical changes on the fibre due to stabilisation. The band that appeared at 1600 cm<sup>-1</sup> was ascribed to conjugated C=N stretching, the peak at ~1580 cm<sup>-1</sup> and corresponding peak at 1375 cm<sup>-1</sup> were ascribed to the characteristic peaks of D and G bands well known for carbon materials. The shoulder at 1250 cm<sup>-1</sup> was assigned to CH group vibrations. There appeared to be no significant changes to EF-08 to indicate TiO<sub>2</sub> coordination to the surface of the nanofibres. The only information that can be derived from the spectrum is that stabilisation of the polymer in EF-08 occurred (see Figure A1 in the appendix) (Chen and Harrison, 2002; Hong *et al.*, 2006; Lee *et al.*, 2012; Rahaman *et al* 2007; Zhang *et al.*, 2007; Zhu *et al.*, 1996).

### 5.3 Carbonisation of the commercial PAN nanofibres

PAN polymer fibres are commonly used as precursors to high performance carbon nanofibres. The following section will discuss the preparation of the carbonised EF-09 – EF-12 series nanofibres (see section 3.5.2). During the carbonisation process most of the non-carbon volatile components are removed from the PAN polymer which may produce stable, high tensile strength fibres containing no functional groups (Rahaman *et al.*, 2007). The following section discusses the possible influences of the thermal step (see Table 3.7) on the EF-09 – EF-012 series nanofibres.

#### 5.3.1 Preparation of the carbonised commercial nanofibres

The preparation of EF-09 – EF-12 is set out in Section 3.5.2. In the carbonisation step the oxidative stabilisation of the commercial PAN nanofibres at 275 °C in air was followed by carbonisation of the nanofibres in nitrogen (see Table 3.8). The fibres were heated from 275 °C to 400 °C at a heating rate of 5 °C/min, and carbonised for 1 hour in nitrogen gas. Due to the volatility of the metal oxides the flow rate of the nitrogen gas was set at 2 cm<sup>2</sup>/min, low enough to maintain an inert environment without blowing away the metal oxides.

Figure 5.19 shows the morphology of EF-09 (10 wt% Ti oxy acac), EF-10 (15 wt% Ti oxy acac), EF-11 (20 wt% Ti oxy acac) and EF-12 (30 wt% Ti oxy acac) as prepared in section 3.5.2, after carbonisation of the thermally coated, oxidatively stabilised commercial PAN nanofibres.

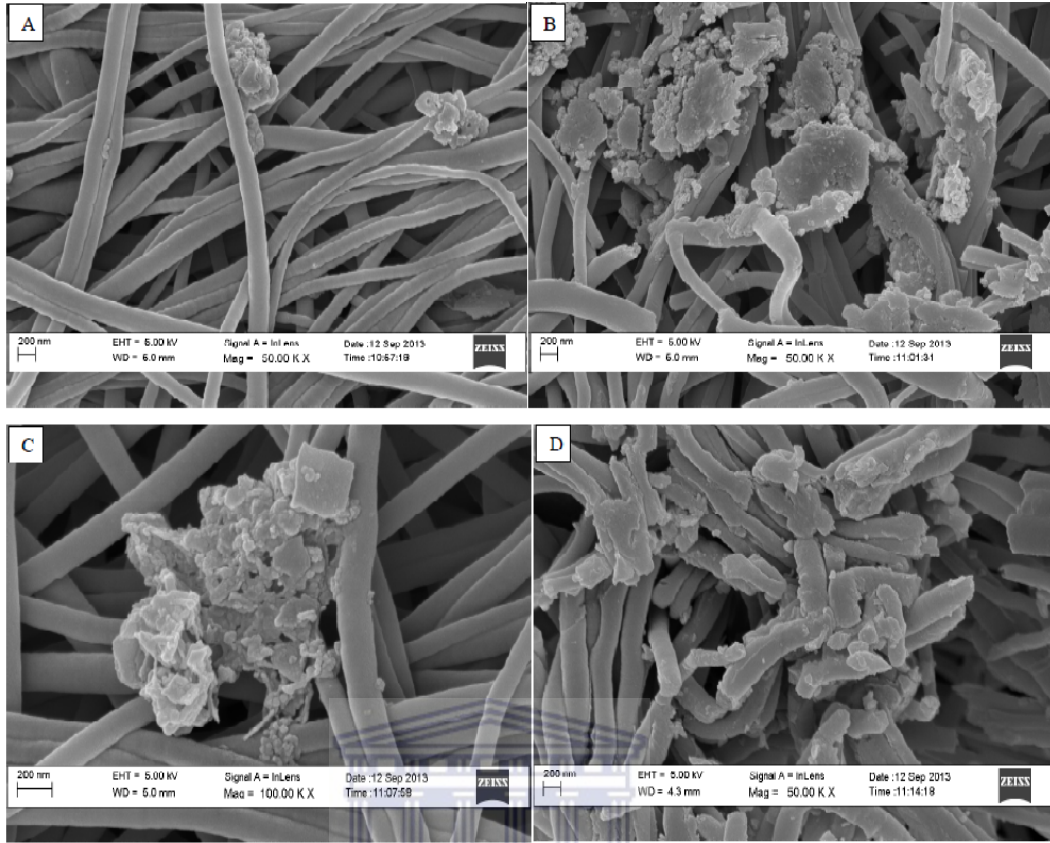


Figure 5.19: HRSEM images showing the TiO<sub>2</sub> coated on top of the carbonised fibres at different concentrations, (A) EF-09 (10 wt% Ti oxy acac), (B) EF-10 (15 wt% Ti oxy acac), (C) EF-11 (20 wt% Ti oxy acac) and (D) EF-12 (30 wt% Ti oxy acac)

Figure 5.19 shows the HRSEM images of the surface morphology of EF-09, EF-10, EF-11 and EF-12. The images show TiO<sub>2</sub> cluster formation to be prevalent. It appears as though the additional carbonisation conditions resulted in the loss of the TiO<sub>2</sub> nanoparticles, and breaking of the PAN fibres into shorter sections (compared to section 5.2.1 Figure 5.16).

Figure 5.20 shows the image of the TiO<sub>2</sub> coated carbonised commercial PAN nanofibres.

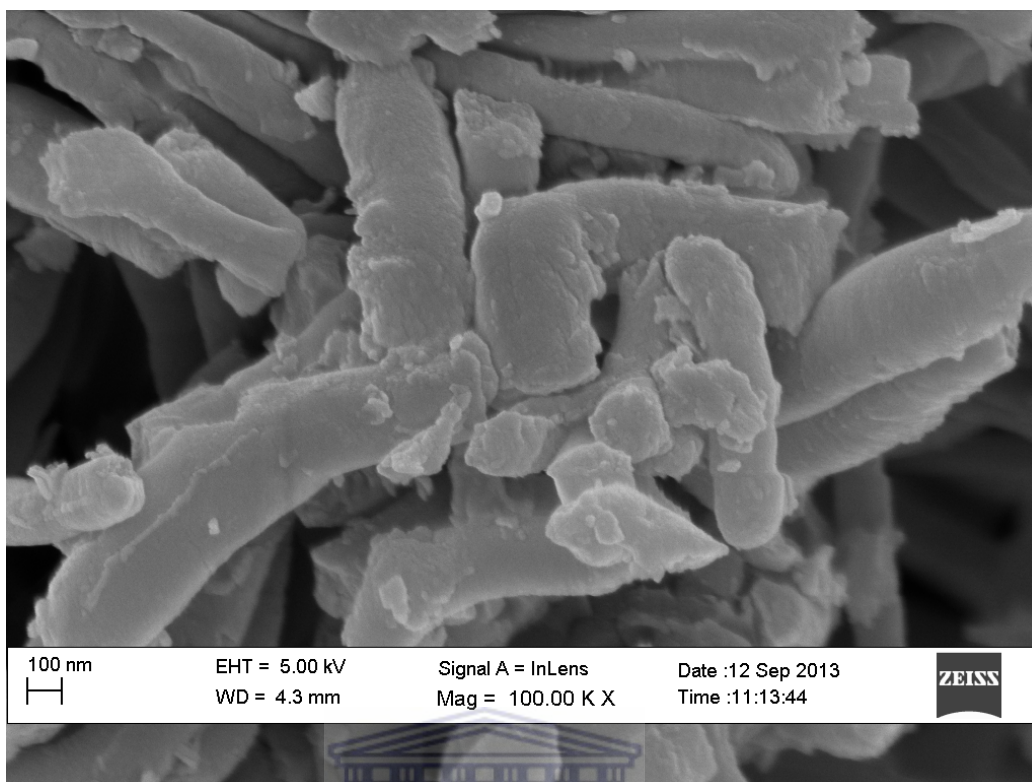


Figure 5.20: HRSEM image of EF-12 (representative of the EF-09-EF-12 series of TiO<sub>2</sub> loaded PAN nanofibres prepared via a thermal coating process), followed by carbonisation at 400 °C with a heating rate of 5 °C/min from 275 °C in nitrogen gas

Figure 5.20 details the surface morphology of EF-12 that was loaded with 30 wt% Ti oxy acac, and compared to the EF-06 that was only loaded with 10 wt% Ti oxy acac. It is clear that carbonisation conditions resulted in the loss of the TiO<sub>2</sub>. This could possibly be ascribed to the evaporation of TiO<sub>2</sub> from the surface of the fibres during the thermal oxidation of TiO<sub>2</sub> during the carbonisation conditions. The nitrogen gas flow might have carried the metal oxides away from the fibres to a cooler area in the reactor where the conditions were favourable for the metal oxides to condense on the surface. The HRSEM image in Figure 5.20 showed the PAN fibres to be broken. This is usually as result of cyclisation occurring too rapidly which results in either fusion or breaking of the fibres (Wangxi *et al.*, 2003).

### 5.3.2 Energy Dispersive X-ray Spectroscopy (EDS)

In order to determine the actual amount of  $\text{TiO}_2$  loading on top of the EF-09 – EF-12 series commercial PAN nanofibres, EDS analysis was carried out as set out in section 3.7.2.2. The EDS analysis should also give an indication of the effectiveness of the loading procedure in terms of the homogeneous distribution of the  $\text{TiO}_2$  on top of the fibres. The  $\text{TiO}_2$  loading was determined as set out in section 3.5.2. The EDS analysis was performed on random sections of the composite nanofibres. The data of  $\text{TiO}_2$  distribution across the EF-09 - EF-12 series fibres nanofibres is given in Table 5.4. The analysis was performed over a 500  $\mu\text{m}$  square area. The results give the qualitative composition of the EF-09 - EF-12 series of composite PAN nanofibres, coated with  $\text{TiO}_2$  via thermal oxidation and then carbonised.

Table 5.4: EDS data of the wt% composition of the EF-09, EF-10, EF-11 and EF-12 series nano fibres (n=1)

Element wt%	EF-09	EF-10	EF-11	EF-12
	10 wt%	15 wt%	20 wt%	30 wt%
<b>C</b>	81.4	76.8	68.6	70.5
<b>O</b>	15.7	20.0	25.1	22.9
<b>Ti</b>	2.9	3.2	6.3	6.6
<b>Total:</b>	100	100	100	100

The EDS analysis (see Table 5.4) of EF-09 - EF-12 series nanofibres performed over a 500  $\mu\text{m}$  square area shows the loading of  $\text{TiO}_2$  on the nanofibres. The results indicate that carbon and  $\text{TiO}_2$  are the principle components of the EF-09 - EF-12 series nanofibres. The EDS data shows the  $\text{TiO}_2$  loading on the EF-09 - EF-12 series fibres to be inconsistent with the theoretical loading. Compared to EF-05 – EF-08 (see Table 5.2) similar wt% composition was expected for EF-09 - EF-12 series fibres as the exact Ti oxy acac/oxidative stabilisation preparation method was followed except for the additional carbonisation step at 400 °C in nitrogen gas. However, the EDS analysis of the EF-09 – EF-12 series nanofibres confirmed carbonisation of the composite fibres resulted in the loss of much of the  $\text{TiO}_2$ .

Figure 5.21 shows the wt% of Ti on the EF-04, EF-05 – EF-08 and EF-09 – EF-12 series fibres to draw a comparison between the effectiveness of TiO<sub>2</sub> loading during electrospinning, or via Ti oxy acac sublimation during thermal stabilisation followed by carbonisation.

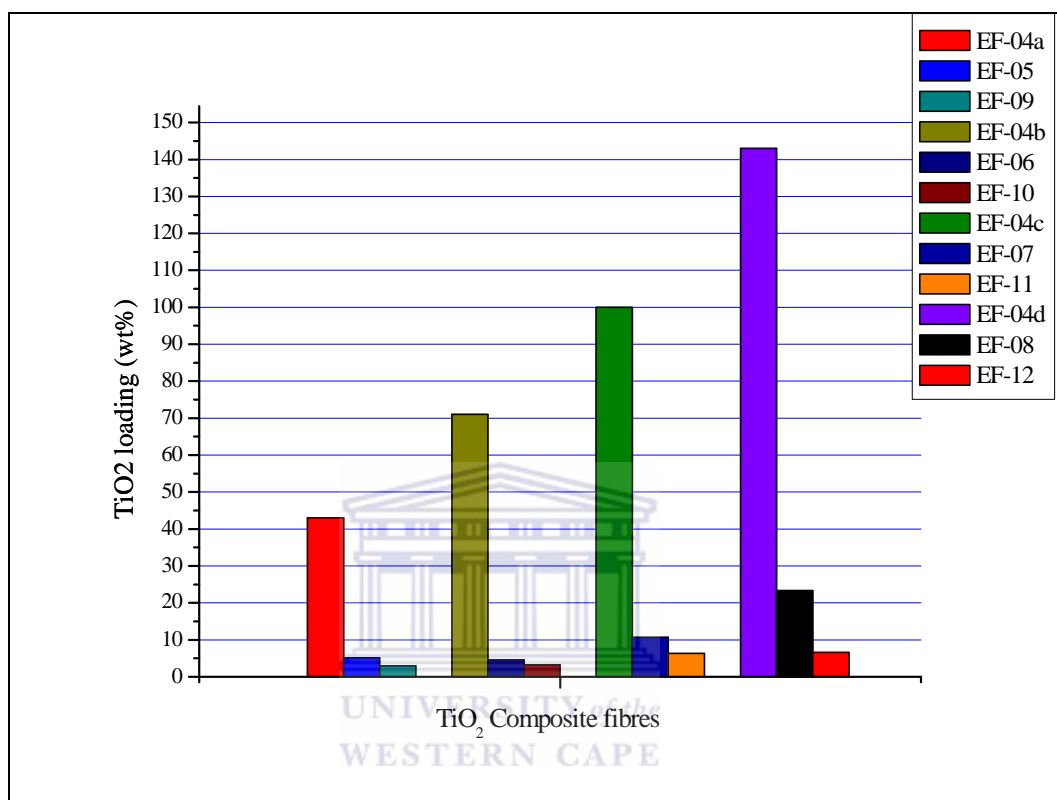


Figure 5.21: Actual Ti loading on the EF-04, EF-05 – EF-08 and EF-09 – EF-12 series of fibres

Figure 5.21 shows the Ti loading on the EF-04, EF-05 – EF-08 and EF-09 – EF-12 series fibres, although higher Ti loading was achieved by incorporating commercial TiO<sub>2</sub> powder in 7 wt% PAN/DMF the actual loading of TiO<sub>2</sub> on the surface of the commercial PAN fibres via thermal oxidation (EF-05 – EF-08) showed greater accuracy with respect to the theoretical 10, 15, 20 and 30 wt% loading. However a positive correlation was observed between the theoretical and actual Ti loading on the EF-04 series fibres therefore electrospinning 7 wt% PAN/DMF containing commercial TiO<sub>2</sub> powdered catalyst would work best to get TiO<sub>2</sub> loaded onto PAN nanofibres.

### 5.3.3 X-Ray Diffraction Spectroscopy (XRD)

XRD was performed on EF-09 to identify the crystal phases of the  $\text{TiO}_2$  nanoparticles thermally coated on the commercial PAN nanofibres. The spectrum was compared to a typical spectrum of anatase and titanium oxide (see section 3.7.3). The x-ray diffraction pattern for EF-09 is shown in Figure 5.22.

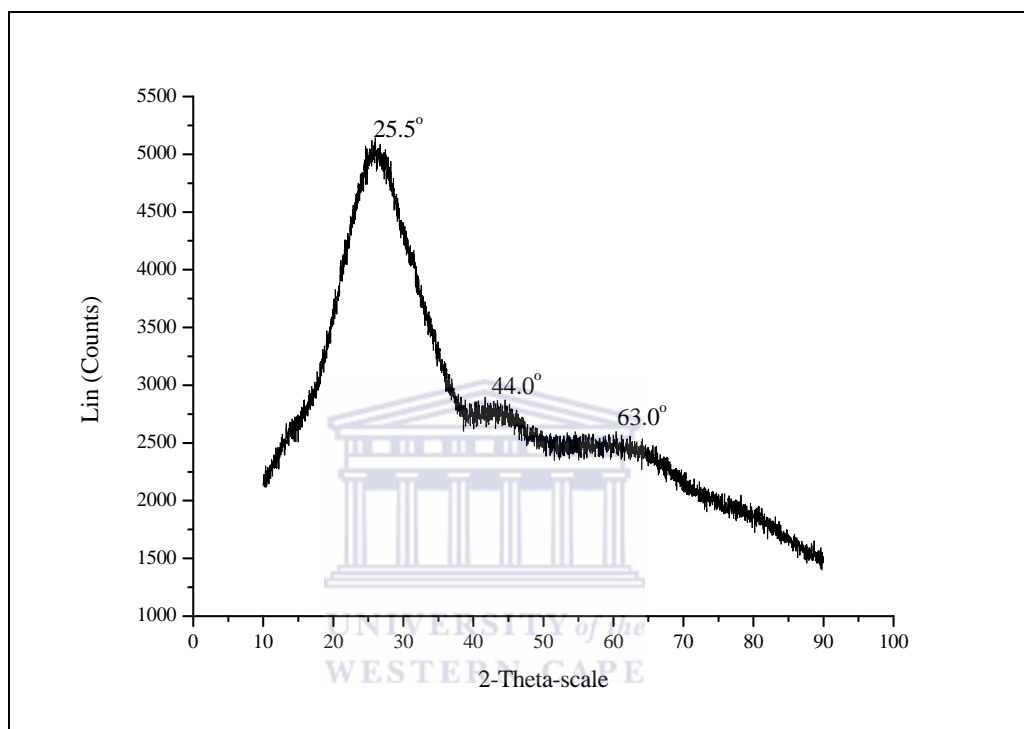


Figure 5.22: X-ray crystallography analysis of the catalyst crystal phases on EF-09

The X-ray diffraction pattern for EF-09 in Figure 5.22 shows a strong diffraction peak at  $\sim 25.5^\circ$ , the diffractogram also identified minor diffraction peaks at  $\sim 44.0^\circ$  and  $\sim 63^\circ$  peaks. These peaks correspond to the formation of pre-graphitic carbon (see Figure 2.10) (Lee *et al.*, 2010). Since EDS data shows the presence of  $\text{TiO}_2$  it is likely that the short range order of the  $\text{TiO}_2$  nanoparticles could not be resolved by XRD because of peak broadening and overlaps with graphitic peaks (Wang *et al.*, 2013). As EDS showed very low  $\text{TiO}_2$  wt% coating and HRSEM confirmed poor dispersion of  $\text{TiO}_2$  upon these samples were not ideal.

### 5.3.4 Fourier Transform Infrared Spectroscopy (FTIR)

FT-IR spectroscopy was performed on EF-09 to identify any possible bonding interaction between the fibre and TiO<sub>2</sub> nanoparticles. Cautious assignments of the IR bands for EF-09 (representative of EF-09 – EF-12 series fibres) in the 4000 – 650 cm<sup>-1</sup> spectral region is given in Table 5.5.

Table 5.5 FTIR absorbance of EF-09 in the 4000 – 650 cm<sup>-1</sup> region

Absorbance (cm <sup>-1</sup> )	Assignment
3500	OH - stretching
~2950	CH - stretching
1700	conjugated C=N stretching – similar to oxidatively stabilised fibres
1600	D – bands – slight shift in absorption
1375	G- bands – similar to oxidatively stabilised fibres
1250	CH - group vibrations – similar to oxidatively stabilised fibres

The absorption peaks in the 3300 – 3500 cm<sup>-1</sup> region were ascribed to OH stretching, the low intensity of the nitrile absorption band at 2250 cm<sup>-1</sup> was due to the chemical changes on the fibre due to carbonisation. The band at 1700 cm<sup>-1</sup> was ascribed to cyclic C=O stretching. The bands at ~1600 cm<sup>-1</sup> and 1375 cm<sup>-1</sup> were ascribed to the characteristic peaks of D and G bands well known for carbon materials. There appeared to be no significant changes to EF-09 to indicate TiO<sub>2</sub> coordination to the surface of the nanofibres. The only information that could be derived from the FTIR data was that carbonisation of EF-09 occurred. This was observed with the increased intensity of the D and G bands at 1600 cm<sup>-1</sup> and 1375 cm<sup>-1</sup> respectively. As with EF-05 – EF-08 there appeared to be no conclusive evidence to suggest the coordination of TiO<sub>2</sub> to the carbonised fibres the only difference between the oxidatively stabilised fibres and carbonised fibres was the elimination of the nitrile groups due to cyclisation where the triple bond structure was converted to the double bond structure (C=N) (see Figure A2 in the appendix) (Chen and Harrison, 2002; Hong *et al.*, 2006; Lee *et al.*, 2012; Rahaman *et al* 2007; Zhang *et al.*, 2007; Zhu *et al.*, 1996).

## 5.4 Summary

This section showed that coating  $\text{TiO}_2$  on the surface of the commercial nanofibres using Ti oxy acac as precursor proved to be impractical. Depositing  $\text{TiO}_2$  on the surface of the commercial fibres required coating the fibres with the titanium precursor solution. Although  $\text{TiO}_2$  was successfully coated on the fibres comparing the EDS data for both the stabilised and carbonised fibres the loading capacity on the fibres was inconsistent with and much lower than the theoretical loading percentage. The carbonisation conditions appeared to remove  $\text{TiO}_2$  from the surface of the fibres. There appeared to be no conclusive evidence to suggest the coordination between  $\text{TiO}_2$  and the fibre support structures, indicating a possibility to leach the  $\text{TiO}_2$  into solution.

Admixing powdered commercial  $\text{TiO}_2$  nanoparticles into the PAN/DMF sol-gel solution makes it possible to electrospin PAN polymer fibres with  $\text{TiO}_2$  loaded in the fibres. EDS analysis of the  $\text{TiO}_2$  containing PAN polymer fibres showed the loading capacity of Ti within the  $\text{TiO}_2$  containing PAN polymer fibres to correspond with the theoretical loading of the sol-gel increasing with increased loading. In terms of gram quantity equivalents EDS data confirmed the amount of  $\text{TiO}_2$  in the fibres were always lower than the 20 mg  $\text{TiO}_2$  reference sample in its particulate form. Compared to the  $\text{TiO}_2$  coated stabilised and carbonised fibres the  $\text{TiO}_2$  loaded polymer fibres displayed higher  $\text{TiO}_2$  loading. The DSC analysis performed on the  $\text{TiO}_2$  loaded PAN polymer fibres indicated a shift in the exothermic peak to a higher temperature that was associated with an increase in thermal stability in the  $\text{TiO}_2$  loaded PAN polymer fibres. Incorporating commercial  $\text{TiO}_2$  inside the electrospun PAN polymer fibres appeared to enhance the thermal stability of the fibres. This could be attributed to the improvement of the crystallinity on the amorphous carbon by  $\text{TiO}_2$ . As for the stabilisation and carbonisation steps, for this particular application the stabilisation steps appear to be redundant. The  $\text{TiO}_2$  containing PAN polymer fibres exhibited acceptable stability and were highly suitable for its application as photocatalyst support structures. The commercial powdered  $\text{TiO}_2$  also added additional stability to the electrospun fibres.

As for the synthesis protocols electrospinning the PAN polymers fibres with the powdered commercial  $\text{TiO}_2$  is simpler than the  $\text{TiO}_2$  thermal coating procedure of the commercial nanofibres. The thermal process is not only complicated, but the efficiency of the process was also unsatisfactory as the actual  $\text{TiO}_2$  loading obtained with the thermal coating process was very low, averaging 50 % of the theoretical loading. Losses could be attributed to  $\text{TiO}_2$  depositing further down the reactor instead of on the fibre following the thermal oxidation of Ti oxy acac. Despite successfully thermally coating the commercial fibres with  $\text{TiO}_2$  using Ti oxyacac + oxidative stabilisation and Ti oxyacac + carbonisation processes it was not possible to synthesise stable  $\text{TiO}_2$  coated fibres, because the fibres also became brittle and broke as was shown by HSEM.



## Chapter 6

### 6. Photocatalytic degradation of methylene blue

The degradation of MB in aqueous solutions is a general method used to characterize the photocatalytic activity of TiO<sub>2</sub> coatings (Tschirch *et al.*, 2008). This section presents the results and demonstrates the photocatalytic degradation of MB by the EF-04 – EF-12 nanofibres. The photocatalytic study was carried out as set out in section 3.6. The composite fibres were submerged in a 100 mL 10 ppm MB solution and subjected to UV-illumination (254 nm). The experiment was conducted over 8 hours. The UV-illumination step was preceded by soaking the composite fibres in the dark for 1 hour in the MB solution to allow for adsorption to stabilise. For most part of the study the experiments were performed only once, some of the experiments were repeated randomly however, the decolouration results of MB remained consistent.

#### 6.1 Baseline study

Before the evaluation of the photocatalytic nanofibres a set of control experiments were performed to isolate the activity of photocatalytic nanofibres being tested from any nuisance variables. The 3 preliminary experiments that served as the control groups were as follows: (1) 100 mL 10 ppm MB illuminated by UV light (254 nm); (2) PAN polymer fibres only, (without TiO<sub>2</sub>) submerged in a 100 mL 10 ppm MB solution illuminated by UV light (254 nm); and (3), 0.0027 g of the unsupported powdered commercial TiO<sub>2</sub> nanoparticles in a 100 mL 10 ppm MB solution illuminated by UV light (254 nm) as set out in section 3.6. The dye removal was determined by sampling 10 mL, using a syringe, of MB solution at 2 hour intervals and measuring the absorbance at 665 nm wavelength using a UV-vis spectrophotometer. Prior to each absorbance measurement the spectrophotometer was calibrated with deionised water. The solution dye absorption by the nanofibres and the beaker walls as well as possible dye degradation due to UV illumination, are all variables that might have an effect on the experimental outcome. The commercial powder TiO<sub>2</sub> nanoparticles were also part of the control group experiments. The amount of 0.0027 g of the commercial

powder (P25)  $\text{TiO}_2$  was used to degrade MB under UV illumination. The weight was chosen to approximate the amount of  $\text{TiO}_2$  represented by a sample of nanofibre weighing approximately 0.0200 g. The percentage MB removal was determined following the Beer-Lambert's law as set out in section 3.6.1.

Figure 6.1 shows the decolouration percentage of the 100 mL 10 ppm MB solutions for the three control group experiments. The degradation study was conducted over 8 hours under UV-illumination (254 nm).

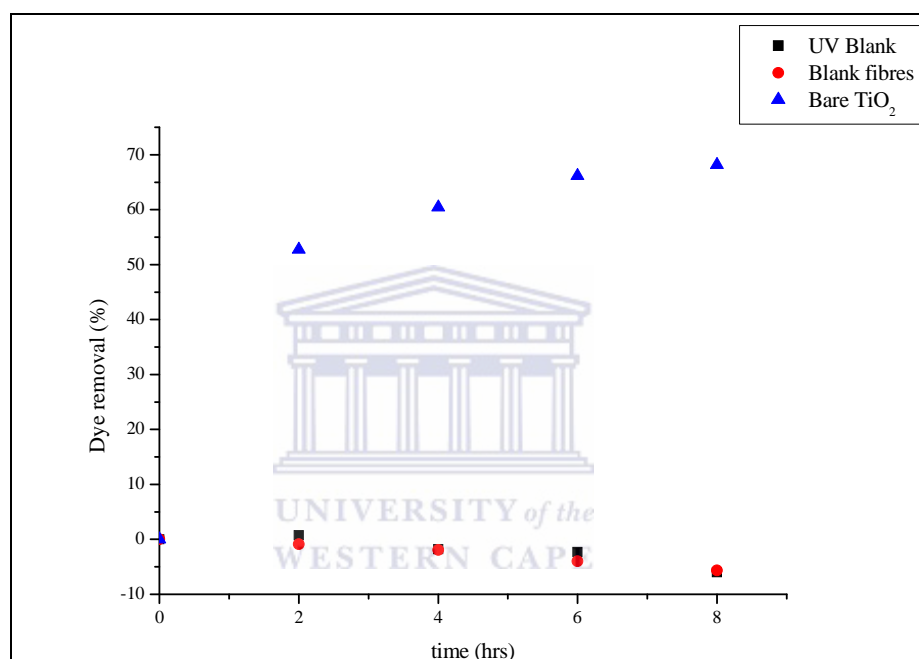


Figure 6.1: 100 mL 10 ppm aqueous MB decolouration for the control group under UV illumination (254 nm) and  $1.242 \text{ W/m}^2$  UV lamp intensity over 8 hours (gram of  $\text{TiO}_2$  P25 = 0.0027 g for bare  $\text{TiO}_2$  sample)

Figure 6.1 demonstrates the effect of UV light by itself, or blank commercial PAN nanofibres, or the commercial powder  $\text{TiO}_2$  on the decolouration of MB. There was no photocatalytic activity detected for either the blank commercial electrospun nanofibres or the UV illuminated MB solution. Therefore these variables had no effect on the decolouration of MB and the removal % remained around zero. Figure 6.1 shows the MB decolouration by the unsupported commercial  $\text{TiO}_2$  as well. Even at a  $\text{TiO}_2$  concentration as low as 25 mg/L, the commercial powdered  $\text{TiO}_2$  displayed sizeable photocatalytic activity for the

duration of the study. The commercial powder TiO<sub>2</sub> decoloured 68 % of the solution after 8 hours.

Figure 6.2 illustrates the first order kinetics of MB removal for the commercial powder TiO<sub>2</sub> nanoparticles.

$$\ln (C/C_0) = -kt \quad (1)$$

$$-k = \ln (C/C_0)/t \quad (2)$$

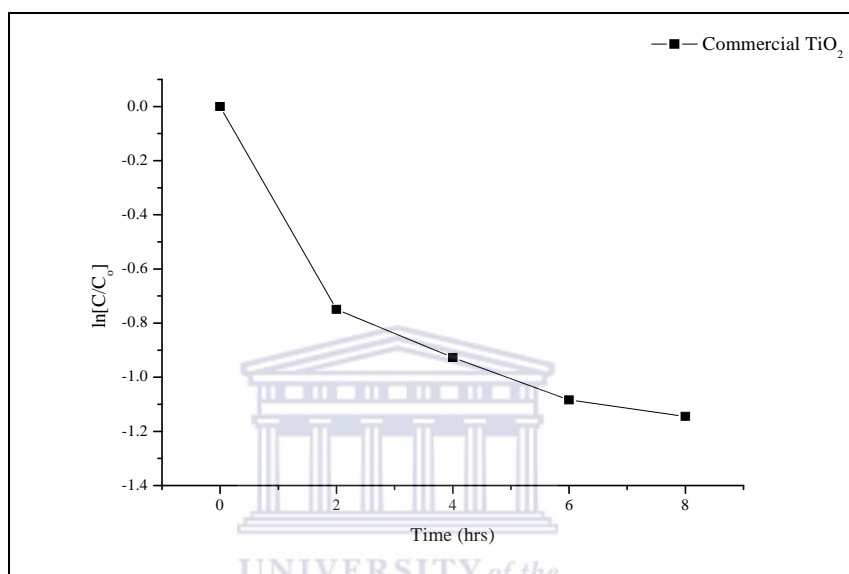


Figure 6.2: First-order kinetics of 100 mL 10 ppm MB solution decolouration by the powdered commercial TiO<sub>2</sub> under UV-illumination and 1.242 W/m<sup>2</sup> UV lamp intensity over 8 hours

The plot of  $\ln (C/C_0)$  with time of irradiation shows the degradation of MB by the commercial TiO<sub>2</sub> catalyst. Photodegradation of MB followed first order kinetics with time which gave a straight line with a slope of  $-k$ . The fitting line validation was based on the linear correlation of data points represented by  $R^2 = 0.74$ . The reaction rate constant increased with the decrease of initial MB concentration. The rate of degradation was therefore dependant only on the TiO<sub>2</sub> concentration. Reddy *et al.*, (2013) and Shi *et al.*, (2000) reported similar findings.

The rate constant of the first order kinetics of MB degradation over the commercial powder TiO<sub>2</sub> is depicted in Equation (1).  $C$  and  $C_0$  are the actual MB concentrations at a given reaction time and initial concentrations of MB at a given

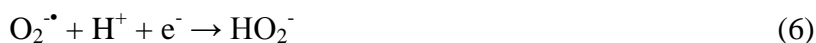
reaction time respectively and k the rate constant. The k value is therefore representative of the process efficiency. Table 6.1 shows the periodic monitoring using UV-Vis of MB decolouration by commercial powder TiO<sub>2</sub> where k is the instantaneous rate constant at the specific time interval and k' the average rate of reaction per second which is extrapolated from the linear graph. The calculations of k are based on the data presented in tables A1 – A4, see Appendix.

Table 6.1: The decolouration of MB during the photocatalyst study at 2 hour intervals for the commercial powder TiO<sub>2</sub>

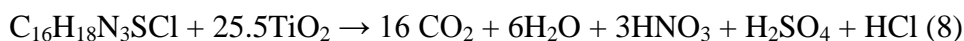
Sample	Decolouration efficiency							
	2 hr	k	4 hr	k	6 hr	k	8 hr	k'
Commercial powder TiO <sub>2</sub> MB% removal	52.74 %	-0.38	60.42 %	-0.23	66.17 %	-0.180	68.16 %	-0.13

The higher the MB concentration was the higher was the photocatalytic activity but as the MB concentration decreased so did the rate constant (k). The average rate of reaction for k' = -0.13 s<sup>-1</sup>, the slope of the graph in Figure 6.2, shows the reaction to still be first order at the end of the experiment. It also shows the rate of MB decolouration to decrease over time. The decrease in the rate of decolouration near the end of the study could be attributed to the increase in the diffusion pathlength of dye to the TiO<sub>2</sub> surface or conversely the longer diffusion pathlength of free radicals to the remaining dispersed dye molecules.

The following chemical equations represent the photocatalytic reactions:



There are two possible reaction mechanisms for MB decolouration, a reversible reaction where MB is reduced to the leuco form and the irreversible degradation of MB by free radicals generated by TiO<sub>2</sub>. The mineralization reaction for MB is shown in Equation (8).



(Tschirch *et al.*, 2008)

MB has been reported to be susceptible to reduction to 'leuco MB'. The reaction is reversible; LMB can be converted back to MB by the addition of O<sub>2</sub> gas to the solution (Tschirch *et al.*, 2008), however this was outside the scope of the study and consequently not tested. This has been reported to affect the decolouration rate of MB (Tschirch *et al.*, 2008; Houas *et al.*, 2001).

Both the PAN polymer fibres and blank MB solution exposed to UV irradiation for 8 hours showed a very slight photoactivity, possibly 'phantom-photoactivity' initially. Although literature reported light wavelengths below 350 nm and in the visible region around 660 nm to affect the decolouration of MB no significant degradation of MB was observed in this study. Tschirch *et al.*, (2008) reported on adsorption of dye onto the reactor surface that changed as the process progressed. This may account for the subzero trends as over 8 hours some of the adsorbed MB may have desorbed after initiation of the experiment.

## 6.2 Photocatalytic activity of EF-04 series nanofibres

The following section presents the results and demonstrates the photocatalytic activity of the EF-04 series of electrospun nanofibres (see Table 3.5). The photocatalytic study was carried out as set out in Section 3.6. The PAN electrospun fibres containing TiO<sub>2</sub> were submerged in a 100 mL 10 ppm MB solution, the experiment was carried out under UV-illumination (254 nm) over 8 hours. The experiment was preceded by soaking the fibres in the MB solution in the dark for 1 hour to allow for adsorption of MB to stabilise. The fibres were prepared by admixing the specified wt% of commercial powder TiO<sub>2</sub> and the 7 wt% PAN/DMF sol-gel. The solution was electrospun using the conditions as set out in Table 3.4. The weights of the fibres used in the experiments were as follows; EF-04a = 3 wt% TiO<sub>2</sub> in 7 % PAN/DMF (0.0170 g); EF-04b = 5 wt% TiO<sub>2</sub> in 7 % PAN/DMF (0.0161 g); EF04c = 7 wt% TiO<sub>2</sub> in 7 % PAN/DMF (0.0141 g); and EF-04d = 10 wt% in 7 % PAN/DMF (0.0178 g). The specified amount of fibres was supported on cello-tape to anchor the fibres and ensure adequate irradiation. The graph in Figure 6.3 shows the photocatalytic activity of

the EF-04 series of electrospun nanofibres with varying the TiO<sub>2</sub> loadings between 3 wt% and 10 wt%. The MB decolouration was measured as set out in Section 3.6.

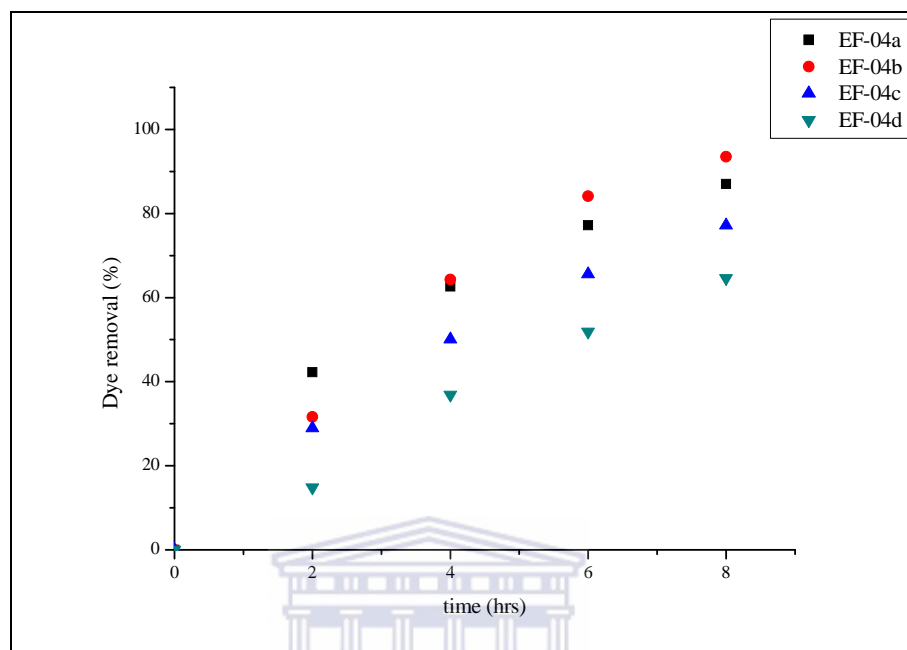


Figure 6.3: 100 mL 10 ppm aqueous MB decolouration for the EF-04 series of nanofibres under UV illumination (254 nm) and 1.242 W/m<sup>2</sup> UV lamp intensity over 8 hours

From the results in Figure 6.3 the greatest photocatalytic activity was achieved with the EF-04b electrospun nanofibres containing 5 wt% of TiO<sub>2</sub>, decolouring 90 % of the MB solution after 8 hours. This could possibly be attributed to adequate dispersion of the TiO<sub>2</sub> photocatalyst within the PAN fibre allowing for a higher active surface area. Photocatalytic ability of the EF-04 series of electrospun nanofibres appeared to decrease as the catalyst loading increased indicating a decrease in active surface area but still most fibres achieved more than 50 % decolouration of MB after 8 hours and were more or less as effective as the unsupported powdered commercial powdered TiO<sub>2</sub> (see Figure 6.1).

The TiO<sub>2</sub>/PAN fibres appeared to be stable for 8 hours under the applied reactions conditions as no leaching of TiO<sub>2</sub> into the solution was detected. To test for leaching of TiO<sub>2</sub> from the TiO<sub>2</sub>/PAN fibres into the solution UV analysis was

performed at 380 nm to test for TiO<sub>2</sub> absorption. UV analysis showed no significant absorbance at 380 nm.

Figure 6.4 illustrates the kinetics of MB decolouration for the EF-04 series of electrospun TiO<sub>2</sub>/PAN nanofibres. EF-04a = 3 wt% TiO<sub>2</sub> in 7 % PAN/DMF (0.0170 g); EF-04b = 5 wt% TiO<sub>2</sub> in 7 % PAN/DMF (0.0161 g); EF-04c = 7 wt% TiO<sub>2</sub> in 7 % PAN/DMF (0.0141 g); and EF-04d = 10 wt% in 7 % PAN/DMF (0.0178 g).

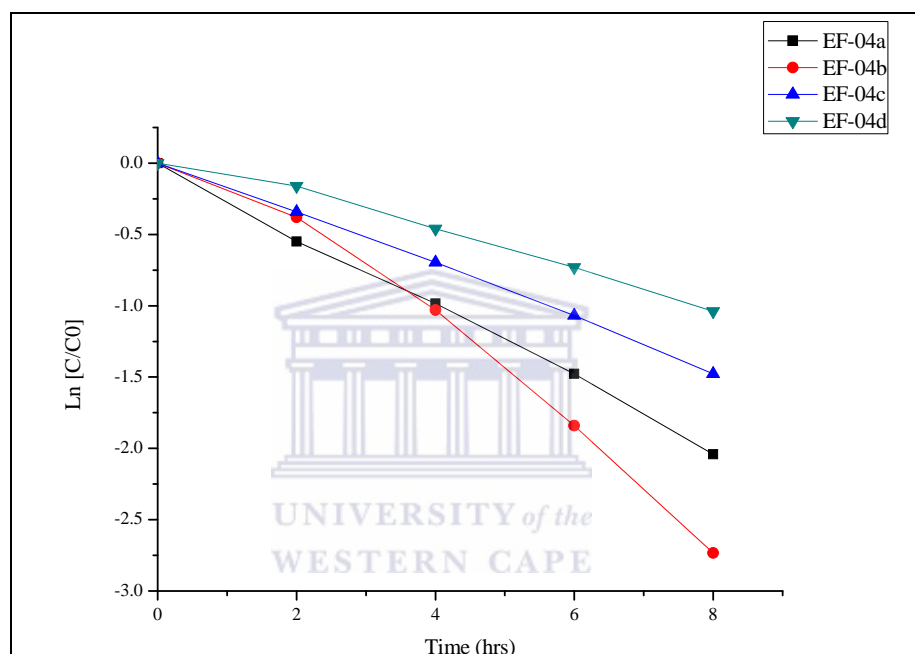


Figure 6.4: Kinetics of photocatalytic decolouration of 100 mL 10 ppm MB solution for the EF-04 series nanofibres under UV-illumination (254 nm) and 1.242 W/m<sup>2</sup> UV lamp intensity over 8 hours

The plot in Figure 6.4 shows the degradation kinetics of the EF-04 series of electrospun TiO<sub>2</sub>/PAN nanofibres over time. From the plot the decolouration of MB followed first order reaction kinetics. Although the initial rate of decolouration was higher in EF-04a, the EF-04b fibres overall displayed the highest rate of decolouration. As the catalyst concentration increased above EF-04c the rate of dye decolouration by the fibres decreased. This might be assigned to the reduction in active surface area of the TiO<sub>2</sub> catalyst as a result of TiO<sub>2</sub> cluster formation within beaded sections of the fibres. The graph indicated the

highest MB decolouration rate was achieved for the EF-04b sample containing approximately 20 wt% of TiO<sub>2</sub> see (Table 5.1). The fitting line validation was based on the linear correlation of data points represented by R<sup>2</sup> which was 0.9 < R<sup>2</sup> < 1 for all four data plots. Table 6.2 shows the periodic monitoring of MB decolouration by TiO<sub>2</sub> containing PAN fibres where k is the rate constant at the specific time interval and k' the overall rate of reaction.

Table 6.2: The decolouration of MB during the experiment at 2 hour intervals for the EF-04 series of electrospun nanofibres

Sample	Decolouration efficiency							
	2 hr	k	4 hr	k	6 hr	k	8hr	k'
EF-04a	42.27 %	-0.275	62.61 %	-0.246	77.19 %	-0.246	87.01 %	-0.251
EF-04b	31.65 %	-0.190	64.32 %	-0.258	84.12 %	-0.307	93.50 %	-0.346
EF-04c	28.97 %	-0.171	50.09 %	-0.174	65.61 %	-0.178	77.18 %	-0.184
EF-04d	14.85 %	-0.080	36.85 %	-0.115	51.87 %	-0.122	64.59 %	-0.132

The EF-04b electrospun nanofibres containing approximately 20 wt% of TiO<sub>2</sub> displayed the highest rate of MB decolouration, achieving up to 94 % decolouration after 8 hours which was considerably higher than the powdered TiO<sub>2</sub> P25 sample. Two reasons can be considered: (1) More grams TiO<sub>2</sub> was used or (2) the well dispersed but supported catalyst allowed better UV light penetration through the solution and thus better utilization of photon energy.

When comparing the activity of the supported TiO<sub>2</sub> catalyst to the powdered TiO<sub>2</sub> there was a significant increase in the activity of the TiO<sub>2</sub> catalyst. The average weight of the TiO<sub>2</sub> loaded fibres were in the range of 0.014 – 0.018 g and considering the partial-qualitative composition (see Table 5.1) the gram quantities of TiO<sub>2</sub> embedded in the fibres ranged between 0.002 – 0.009 g. Therefore the improved activity can be attributed to better light penetration of the TiO<sub>2</sub>, considering that the powdered TiO<sub>2</sub> catalyst with a weight of 0.0027 g turned the MB solution opaque in its particulate form, increasing the turbidity of the solution and obscuring the UV light penetration (Rincon and Pulgarin, 2003).

### 6.3 Photocatalytic activity of EF-05 – EF-08 nanofibres

The following section presents the results of the commercial PAN titanium oxy acac oxidatively stabilised fibres and demonstrates the photocatalytic ability of the EF-05 – EF-08 series of nanofibres (see Table 3.8). The composite fibres were prepared by coating the commercial electrospun PAN fibres with titanium oxy acac dissolved in methanol. The fibres, approximately 20 mg in weight, were then thermally stabilised at 275 °C for 1 hour, the heating rate was maintained at 1 °C per minute as set out in section 3.5.2. The photocatalytic study was carried out as set out in section 3.6. The wt% of the catalyst loaded on the EF-05 – EF-08 series nanofibres were as follows as per EDS results (see Table 5.2), EF-05 5.14 wt%, EF-06 4.60 wt%, EF-07 10.7 wt% and EF-08 23.31 wt%. The fibres were submerged in a 100 mL 10 ppm MB solution. The fibres were prepared by thermally coating the commercial PAN fibres with TiO<sub>2</sub> during the stabilisation process of the fibres at 275 °C (see section 3.5.2). The titanium oxy acac loading were as follows, the EF-05 fibres corresponded theoretically with 10 wt% titanium oxy acac loading, EF-06 corresponded theoretically to 15 wt% titanium oxy acac loading, EF-07 corresponded theoretically to 20 wt% titanium oxy acac loading and EF-08 corresponded theoretically to 30 wt% titanium oxy acac loading. The photocatalytic degradation experiment was carried out under UV-illumination (254 nm) over 8 hours. The experiment was preceded by soaking the fibres in the MB solution in the dark for 1 hour to allow for adsorption of MB to stabilise. Figure 6.5 shows the photocatalytic activity for the EF-05 – EF-08 nanofibres.

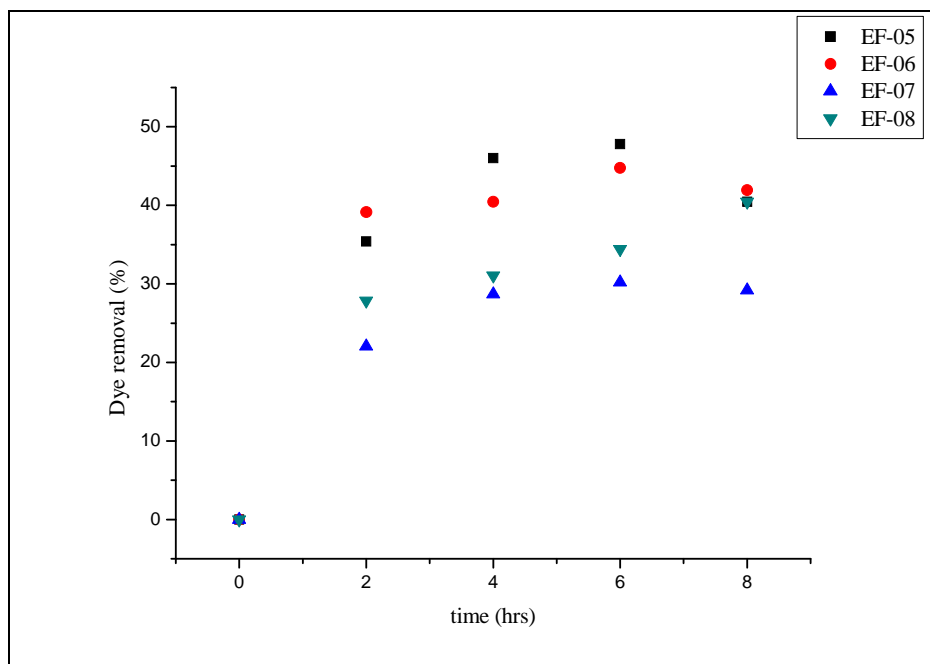


Figure 6.5: 100 mL 10 ppm aqueous MB solution decolouration for the EF-05 – EF-08 series nanofibres under UV illumination (254 nm) and 1.242 W/m<sup>2</sup> UV lamp intensity over 8 hours (catalyst loading EF-05 10 wt%, EF-06 15 wt%, EF-07 20 wt% and EF-08 30 wt%)

The results in Figure 6.5 showed the fibres prepared using the Ti oxy acac process to coat TiO<sub>2</sub> onto commercial PAN fibres to have effectively decolourized the MB dye solution by between 25 – 50 % after 8 hours. EF-05 displayed lower photocatalytic ability compared to the powdered TiO<sub>2</sub> and the TiO<sub>2</sub> containing fibres decolouring 48 % of the MB solution after 8 hours. The highest MB removal of 48 % was achieved after 6 hours for EF-05 which gave the best activity of all of this series of TiO<sub>2</sub> coated PAN fibre samples. The fibres proved to be stable under the reaction conditions with no detectable leaching of the catalyst into the solution. This was determined by sampling 10 mL of the MB solution and measuring the absorbance at 380 nm wavelength to detect possible traces of TiO<sub>2</sub> using the UV-vis spectrophotometer.

Figure 6.6 illustrates the kinetics of MB decolouration for EF-05 – EF08

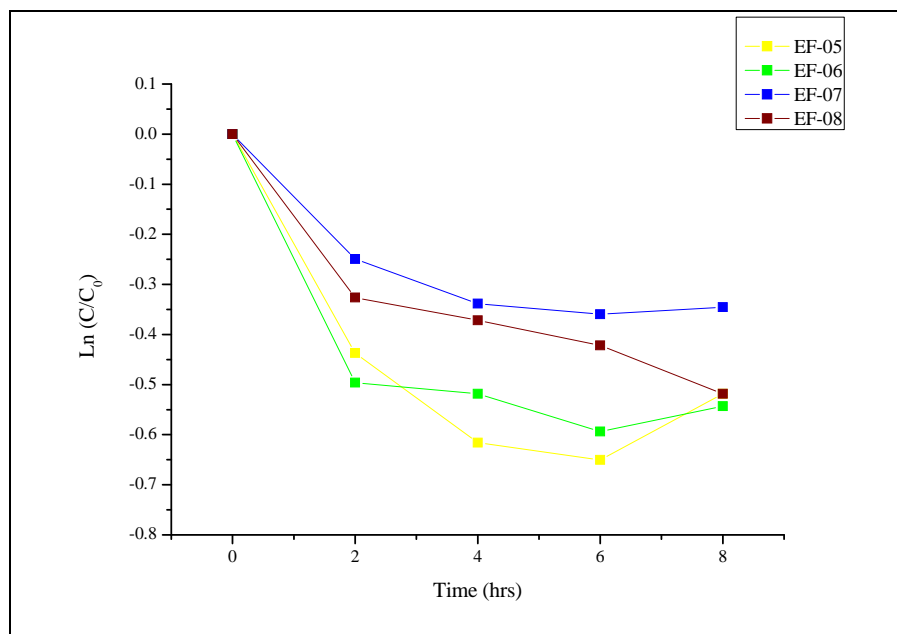


Figure 6.6: Kinetics of photocatalytic decolouration of 100 mL 10 ppm MB solution for the EF-05 – EF-08 series nanofibres under UV-illumination (254 nm) and  $1.242 \text{ W/m}^2$  UV lamp intensity over 8 hours (catalyst loading EF-05 10 wt%, EF-06 15 wt%, EF-07 20 wt% and EF-08 30 wt%)

Table 6.3 shows the periodic monitoring of MB decolouration by samples of thermally coated  $\text{TiO}_2$  on PAN fibres where  $k$  is the rate constant at the specific time interval and  $k'$  the overall rate of reaction. The fitting line validation was based on the linear correlation of data points represented by  $R^2$  which was  $0.5 < R^2 < 1$  for all four data plots. The decrease in the rate of decolouration indicated by the graph in Figure 6.6 is generally associated with an increase in solution oxygen and pH conditions that favour the oxidation of LMB back to MB (Tschirch *et al.*, 2008).

Table 6.3: The decolouration of MB during the photocatalyst study with sampling performed at 2 hour intervals for the EF-05 – EF-08 series nanofibres

Sample	Removal efficiency							
	2 hr	k	4 hr	k	6 hr	k	8 hr	k'
EF-05	35.40 %	-0.218	45.99 %	-0.154	47.81 %	-0.108	40.46 %	-0.063
EF-06	39.13 %	-0.248	40.44 %	-0.130	44.76 %	-0.099	41.92 %	-0.059
EF-07	27.85 %	-0.163	31.05 %	-0.093	34.43 %	-0.070	40.46 %	-0.057
EF-08	22.06 %	-0.125	28.69 %	-0.085	30.20 %	-0.060	29.21 %	-0.040

The plot in Figure 6.6 shows the decolouration pathway for EF-05, EF-06, EF-07 and EF-08 over time. Initially the decolouration of MB follows first order kinetics however, the plot identified a type of plateau at the 6 hour mark. Towards the end of the experiments an increase in MB concentration was observed for all the fibres but one, EF-07. MB concentration decreased sharply to reach a plateau however for EF-07 after the 6 hour mark EF-07 continued to decolour the MB solution to yield a maximum of 40.56%. The changes in the trend of decolouration of MB towards the end of the experiments might be attributed to changes in the reaction conditions, resulting in desorption of MB into the solution or the oxidation of LCM to MB. The change in the rate of decolouration could also be attributed to the loss of catalyst, however no significance absorbance was observed at 380 nm to confirm leaching of TiO<sub>2</sub>. Considering all the possibilities the plateau might be attributed to a loss in the active surface area of TiO<sub>2</sub> which directly affects the adsorption of MB (Tschirch *et al.*, 2008; Wilhelm and Stephan, 2007).

#### **6.4 Photocatalytic activity of EF-09 – EF-12 nanofibres**

The following section presents the results of commercial PAN titanium oxy acac carbonised PAN fibres and demonstrates the photocatalytic ability of the EF-09 – EF-12 nanofibres (see Table 3.8). The composite fibres, approximately 20 mg in weight, were prepared by coating the commercial electrospun PAN fibres with titanium oxy acac dissolved in methanol. The fibres were heated to 275 °C the heating rate was maintained at 1 °C per minute, thereafter the fibres were then carbonised at 400 °C for 1 hour. The heating rate after the 275 °C stabilisation step was kept to 5 °C per minute as set out in section 3.5.2. The photocatalytic study was carried out as set out in section 3.6. The titanium oxy acac wt% loading on the carbonised commercial PAN fibres were as follows EF-09 corresponded theoretically to 10 wt% Ti oxy acac, EF-10 corresponded theoretically to 15 wt% Ti oxy acac, EF-11 corresponded theoretically to 20 wt% Ti oxy acac and EF-12 corresponded theoretically to 30 wt% Ti oxy acac prepared as set out in section 3.5.2. The wt% of the catalyst loaded on the EF-09 – EF-12 series nanofibres were as follows as per EDS results (see Table 5.3), EF-09 2.95 wt%, EF-10 3.21 wt%, EF-11 6.33 wt% and EF-12 6.61 wt%. There appeared to be no correlation

between the theoretical loading that ranged between 10 – 30 wt% and the actual loading. The EF-09 – EF-12 series nanofibres were submerged in a 100 mL 10 ppm MB solution, the experiment was carried out under UV-illumination (254 nm) over 8 hours. The experiment was preceded by soaking the fibres in the MB solution in the dark for 1 hour to allow for adsorption of MB to stabilise. Figure 6.7 depicts the photocatalytic activity for the EF-09 – EF-12 nanofibres.

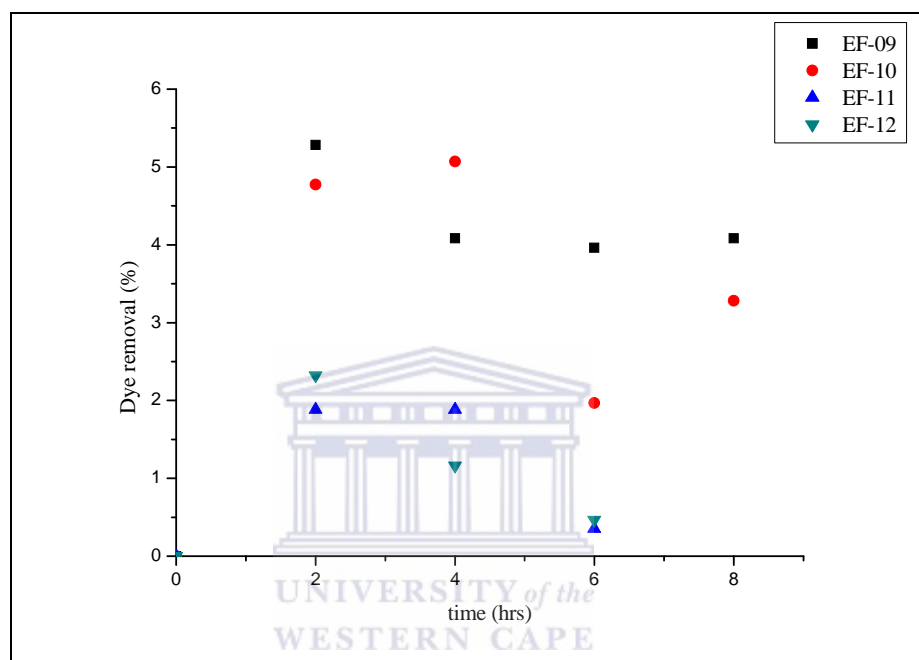


Figure 6.7: 100 mL 10 ppm aqueous MB solution decolouration for the EF-09 – EF-12 series nanofibres under UV illumination (254 nm) and  $1.242 \text{ W/m}^2$  UV lamp intensity over 8 hours

From the graph, (see Figure 6.7) there appeared to be very little decolouration of the MB dyes solutions by EF-09, EF10, EF-11 and EF-12, activity being below 6 % over 8 hours. The fibre performance was quite unusual, based on trends in literature these fibres should have had the greatest photocatalytic potential. Compared to the EF-05 – EF-08 fibres there were no correlations in terms of the photocatalytic activity of the EF-09 – EF-12 fibres with the same theoretical loading. This low activity could be attributed to the harsh thermal preparation conditions of the  $\text{TiO}_2$  coated carbonized nanofibres. In the preparation step the carbonisation of the fibres, at  $400 \text{ }^\circ\text{C}$ , was conducted under nitrogen following stabilisation of the fibres in oxygen. It is possible that the lack of photocatalytic

activity could be attributed to the loss of much of the TiO<sub>2</sub> from the fibre surface which was confirmed by EDS. The loss of TiO<sub>2</sub> during carbonisation could be seen in Figure 5.19. The TiO<sub>2</sub> coated on top of PAN was not firmly supported, and may have become unstable during the heating steps due to the volatility of the metal oxide.

The oxidative stabilisation and carbonisation steps of the PAN fibres are therefore not required for the fabrication of photocatalytic nanofibres as these additional processing steps are complicated and resulted in less effective photocatalytic activity, contrary to what is reported in literature (Kim *et al.*, 2012).

## 6.5 Summary

This section reviewed the photocatalytic activity of the composite fibres. When comparing the photocatalytic ability of the unsupported commercial powder TiO<sub>2</sub> to the TiO<sub>2</sub> containing nanofibres (EF-04a –EF-04d and EF-05 –EF-08), the different samples elicited very significant different rates of MB decolouration. CO<sub>2</sub> evolution during the degradation study was not measured consequently MB degradation is expressed as a measure of decolouration of the MB solution.

The EF-04 series electrospun nanofibres showed the greatest activity in the MB decomposition. The EF-04 series nanofibres outperformed the commercial powdered TiO<sub>2</sub>. All of the EF-04 series fibres achieved more than 65 % decolouration over 8 hrs. The EF-04 series of TiO<sub>2</sub> containing electrospun nanofibres outperformed the EF-05 – EF-08 thermally coated fibres, that displayed intermediate photocatalytic abilities of about 50 %, and EF-05 – EF-12 series of carbonised nanofibres coated with TiO<sub>2</sub> as well. In terms of catalyst loading, incorporating the TiO<sub>2</sub> catalyst in the electrospinning solution prior to preparing the fibre was more effective, as the commercial powdered TiO<sub>2</sub> nanoparticles appeared to be better dispersed inside the electrospun PAN fibres and the loading of the TiO<sub>2</sub> catalyst was also much easier and more consistent compared to thermally coating the TiO<sub>2</sub> onto the surface of commercial PAN fibres.

The powdered commercial TiO<sub>2</sub> containing PAN fibres synthesised in this study that yielded the best performance was electrospun from a 5 g 7 wt% PAN/DMF sol-gel and loaded with 5 wt% commercial powdered TiO<sub>2</sub>. The average fibre diameter was 300 nm. Illuminated by one 9 W UV-light source with a 254 nm wavelength the TiO<sub>2</sub> containing fibres were able to degrade 90 % of a 10 mg/L MB solution in 8 hours. It seems that the greatest photocatalytic activity of TiO<sub>2</sub> can be achieved using a shorter wavelength UV irradiation, in this instance 254 nm. On the basis of these results a UV-light source with a 254 nm wavelength and light intensity of 1.242 W/m<sup>2</sup> had no effect on MB decolouration when no TiO<sub>2</sub> was present but when illuminated by this UV-light source TiO<sub>2</sub> containing PAN nanofibres were photocatalytic active.

As mentioned before  $k$ , the rate constant, is a representative value of the reaction rate constant. Thus  $k'$  is an overall representative value of the process efficiency and inversely proportional to the photocatalyst, TiO<sub>2</sub>, efficiency. From the data it can be noted that the increased TiO<sub>2</sub> concentration does not present lower rate constant values as expected. Instead the results identified a maximum data value after which  $k'$  decreased indicating lower process efficiencies with increased catalyst loading of the fibres. The results therefore suggest that there was a TiO<sub>2</sub> concentration that provided the best photoactivity. EF-04b, representative of 5 wt% TiO<sub>2</sub> loading, presented the lowest rate constant and greatest efficiency in terms of dye removal and catalyst activity.

Im *et al.*, (2008) were able to successfully electrospin PAN fibres containing Degussa P25 TiO<sub>2</sub> the average fibre diameter was 0.8  $\mu$ m. The fibres were able to photocatalytically degrade Rhodamine B, however, it was only able to remove 80 % of the dye and this was achieved after 38 hours. Although Prasharn *et al.*, (2011) electrospun nanofibre webs containing TiO<sub>2</sub> with an average fibre diameter that ranged from 170 – 220 nm, the maximum MB decolouration achieved was also 80 %. Their study was conducted in a chamber equipped with 8 UV-A 8 W lamps with wavelengths ranging from 315 – 380 nm.

## Chapter 7

### 7. Conclusions and Recommendations

#### 7.1 Introduction

The key findings of the study were highlighted and summarised at the end of chapters 4, 5 and 6 and were used to formulate the conclusions presented in this chapter and to give recommendations for future studies.

#### 7.2 Conclusions of this research

The study was carried out with the aim of evaluating the effect of enriching electrospun PAN polymer fibres or thermally treated PAN fibres with the active mineral phase TiO<sub>2</sub> and to study the fibre integrity and the photocatalytic ability of the fibres. This was investigated by either: formulating a sol-gel to allow for the electrospinning of fibres with the narrowest diameter and then electrospinning nanofibres supplemented with TiO<sub>2</sub> nanoparticles, or thermally coating commercial electrospun PAN fibres with TiO<sub>2</sub> using a thermal oxidation process, followed by oxidatively stabilising and carbonising the thermally coated fibres.

The TiO<sub>2</sub> coated oxidatively stabilized fibres were prepared by thermal oxidation of titanium oxy acetylacetonate on the surface of the commercial electrospun PAN nanofibres which were treated at 275 °C. At the onset of the experiments TGA analysis was initially performed on the commercial PAN electrospun nanofibres to identify the temperatures at which oxidative stabilisation and carbonisation initiates. The fibres were prepared by heating the fibres coated with Ti oxy acac to 275 °C with a heating rate of 1 °C per minute, thereafter some fibres were additionally carbonised at 400 °C for 1 hour in nitrogen. During the heat treatment process the Ti oxy acac thermally oxidised on the surface of the commercial electrospun fibres. HRSEM analysis of the surface morphology of the fibres coated with TiO<sub>2</sub> showed cluster formation to become more prevalent as the loading increased from 10 wt% to 30 wt%. The results from the photocatalytic study showed this to have an influence on the photocatalytic ability of the fibres. The thermally prepared fibres with TiO<sub>2</sub> loading at best could only achieve 48, 45 and 34 % MB decolouration for the fibres loaded with 10, 15 or 20 wt% Ti oxy

acac respectively. The photocatalytic ability went down further for the fibres loaded with 30 wt% Ti oxy acac achieving only a 30 % MB decolouration. Although the thermally coated fibres displayed some photocatalytic activity the 20 mg fibre sample (EF-05) coated with 10 wt% Ti oxy acac were only able to degrade 48 % of the 10 mg/L MB solution over the 8 hour experimental period. No photocatalytic activity was noticed in the TiO<sub>2</sub> coated carbonised fibres during the photocatalytic decolouration of MB over the 8 hour experimental period. The lack of photocatalytic activity was attributed to the loss of the catalyst during the carbonisation heat treatment step and was confirmed by EDS analysis of the TiO<sub>2</sub> coated carbonised fibres. These fibres were not subjected to further stability analysis as the heat treatment steps resulted in the fibres becoming brittle and inelastic, contrary to what is reported in literature.

Rheological analysis performed on the PAN/DMF sol-gel identified the optimum PAN/DMF wt% ratio to be 7 wt% to electrospin continuous nanofibres. Commercial powdered TiO<sub>2</sub> was incorporated into the fibres that were successfully electrospun after establishing the ideal parameters for the fabrication of the narrowest uniform fibres. This was achieved by dispersing 3, 5, 7 or 10 wt% of the catalyst in 5 g aliquots of the sol-gel solution prior to electrospinning. HRSEM and TEM imaging showed the electrospun TiO<sub>2</sub> containing fibres to have an average diameter of 300 nm with the commercial powdered TiO<sub>2</sub> distributed inside the polymer nanofibres. These composite fibres were successfully applied in the decolouration of MB. When illuminated by a 9 W UV-light source with a 254 nm wavelength and 1.242 W/m<sup>2</sup> light intensity approximately 20 mg of the TiO<sub>2</sub> containing electrospun fibres degraded 90 % of a 10 mg/L MB solution within 8 hours. Also, submerging the fibres into the MB solution 4 cm from the UV-light source appeared to have no adverse effect on the photocatalytic activity of the fibres. DSC analysis showed TiO<sub>2</sub> to impart additional thermal stability to the electrospun TiO<sub>2</sub> containing polymer fibres. UV Vis spectroscopy detected no noticeable leaching of TiO<sub>2</sub> from the fibres into the MB solution. When illuminated by a 254 nm UV-light source the fibres were more photocatalytically active compared to the powdered TiO<sub>2</sub> in its free particulate form, probably because the powder form catalyst increased the turbidity of the solution and

prevented adequate UV penetration. No alterations were made to the size, morphology or composition of the catalyst. The improved photocatalytic behaviour of the electrospun TiO<sub>2</sub> containing fibres was therefore attributed to greater catalyst exposure to UV light and subsequently improved photon penetration only. Also the areas where the TiO<sub>2</sub> penetrated the surface of the electrospun fibers were porous and could have assisted in the photocatalytic activity of the fibres by increasing the adsorption capacity of the fibres. It is postulated that the MB molecules first adsorbed onto the surface of the fibres and then migrated towards the TiO<sub>2</sub>. However, when the TiO<sub>2</sub> containing PAN polymer fibres were subjected to accelerated oxidizing conditions during the photolysis of hydrogen peroxide, a test which simulated advanced radical formation conditions over a 12 hour period, the fibres became brittle once they were removed from the solutions. The structural changes that took place in the polymer fibres could be as a result of polymerization that was induced by the radical environment, such changes to the polymer can have an effect on its mechanical properties.

The incorporation of commercial powdered TiO<sub>2</sub> P25 into the commercial PAN polymer sol-gel solution prior to electrospinning appears to be the most functional method of enriching PAN polymer fibres with TiO<sub>2</sub>. Coating the TiO<sub>2</sub> onto the surface of the fibres would require a crystallization step in which the amorphous titanium becomes crystalline. Such a step can be both energy and time consuming and a good product was not obtained under the conditions tested. In this study the amorphous titanium acac was thermally oxidised, on commercial electrospun PAN fibres, to the crystalline state during the oxidative stabilisation and carbonisation heat treatment steps. The heat treatment steps were harsh and resulted in the loss of the viscoelasticity of the fibres and also risked losing the catalyst during the thermal oxidation of Ti oxy acac to TiO<sub>2</sub>. Stretching of the fibres before the heat treatment procedures is considered crucial as it prevents cross-linking of the polymer. In this study, this step was omitted which might explain why the heat treatment steps resulted in the loss of the viscoelasticity of the fibres. Therefore the intricacy and ramification of each step in the heat

treatment process of the PAN polymer fibres make this procedure very complicated.

On the other hand, TiO<sub>2</sub> could be successfully incorporated into electrospun nanofibres without affecting the photocatalytic abilities of the TiO<sub>2</sub> but actually enhancing it. It should be remarked that a photocatalyst should not just display excellent photocatalytic activity but should also simplify the recovery process as well. Incorporating P25 TiO<sub>2</sub> the catalyst into the PAN sol-gel and then electrospinning the fibres enhanced the efficiency of the catalyst by improving the active surface area of TiO<sub>2</sub>. It also circumvented the turbidity caused by TiO<sub>2</sub> nanoparticles when used in the free particulate form and had substantial low turbidity. The findings of the study were used to answer the research questions as well as test the hypotheses mentioned in section 1.4. Since there was an improvement in the performance of the TiO<sub>2</sub> composite fibres and no leaching of the TiO<sub>2</sub> into the solution, the hypothesis (H1 and H2) of supporting TiO<sub>2</sub> on top or inside electrospun fibres to eliminate the problems associated with free floating TiO<sub>2</sub> nanoparticles in free particulate form can be accepted. Incorporating the TiO<sub>2</sub> catalyst in the fibres also improved the efficiency of TiO<sub>2</sub> by enhancing the exposure of the catalyst to the light source as the rate of decolouration of the TiO<sub>2</sub> embedded fibres compared to the TiO<sub>2</sub> nanoparticles were greater therefore H2 can also be accepted. The related null-hypotheses (H01 and H02) can be rejected as no secondary removal steps were required as no leaching of TiO<sub>2</sub> into the solution was detected. When the fibres were subjected to accelerated radical formation conditions the fibres lost viscoelasticity, therefore the null-hypothesis (H03) can be accepted as the polymer fibres did not maintain their integrity under accelerated aging and thus may not be very durable during application in an enriched radical environment.

### **7.3 Recommendations and future work**

From the scope of the study there are some recommendations for future research.

- The FTIR characterization of the fibres could not give conclusive evidence of coordination between powdered TiO<sub>2</sub> and the PAN nanofibres. Further

characterisation is required to establish appropriate baselines for identification of possible coordination between  $\text{TiO}_2$  and the nanofibres

- There is a need to alter the preparation procedure for the  $\text{TiO}_2$  containing electrospun PAN fibres by dispersing the  $\text{TiO}_2$  in the DMF solvent and using the  $\text{TiO}_2$  infused DMF solution to dissolve the PAN polymer to form the sol-gel as this might improve the catalyst dispersion and minimize cluster formation. The resulting sol-gel should be electrospun and the fibre morphology and  $\text{TiO}_2$  distribution assessed
- A different method of coating  $\text{TiO}_2$  on the surface of electrospun PAN fibres is required, for instance submerging the fibres in a titanium substrate for example a 20 %  $\text{TiCl}_4$  in HCl solution and facilitating the oxidation of the titanium precursor to  $\text{TiO}_2$
- The heat treatment procedures were very harsh and resulted in the fibres becoming brittle and loosing elasticity, however laboratory prepared electrospun PAN fibres subjected to similar heat treatment steps as the commercial electrospun fibres might have different mechanical properties. The affects of pre-treatment procedures, such as hydrolysis and stretching of the fibres, on the properties of the heat treated fibres should be assessed

## References

- Abdolahi A., Hamzah E., Ibrahim Z., Hashim S. 2012. Synthesis of uniform polyaniline nanofibres through interfacial polymerization. *Materials*. Volume 5:1487-1494
- Adams L. K. Lyon D.Y., Alvarez P.J.J. 2006. Comparative eco-toxicity of nanoscale TiO<sub>2</sub>, SiO<sub>2</sub>, and ZnO water suspensions. *Water research* (40):3527-3532
- Aman N., Satapathy P.K., Mishra T., Mahato M., Das N. N. 2012. Synthesis and photocatalytic activity of mesoporous cerium doped TiO<sub>2</sub> as visible light sensitive photocatalyst. *Materials Research Bulletin*. Volume 47:179-183
- Andreozzi R., Caprio V., Insola A., Marotta R. 1999. Advanced oxidation processes (AOP) for water purification and recovery. *Catalysis Today*. Volume 53:51:59
- Antic Z., Krsmanovic R. M., Nikolic M. G., Marinovic-Cincovic M. M., Mitric M., Polizzi S., Dramicanin M. D. 2012. Multisite luminescence of rare earth doped TiO<sub>2</sub> anatase nanoparticles. *Materials Chemistry and Physics*. Volume 135:1064-1069
- Arana J., Dona-Rodriguez J. M., Rendon E. T., i Cabo C. G., Gonzalez-Diaz O., Herrera-Melian J.A., Perez-Pena J., Colon G., Navio G. C. 2003. TiO<sub>2</sub> activation by using activated carbon as a support Part I. Surface characterization and decantibility. *Applied Catalysis B: Environmental*. Volume 44:161-172
- Ayala P., Arenal R., Rummeli M., Rubio A., Pichler T. 2010. The doping of carbon nanotubes with nitrogen and their potential applications. *Carbon*. Volume 48:575-586
- Bai J., Yang Q., Wang S., Yaoxian L. 2011. Preparation and characterization of electrospun Ag/polyacrylonitrile composite nanofibres. *Korean Journal of Chemical Engineering*. Volume 28(8):1761-1763

- Ballari M. de los M., Brandi R., Alfano O., Cassano A. 2008. Mass transfer limitations in photocatalytic reactors employing titanium dioxide suspensions: I. Concentration profiles in the bulk. *Chemical Engineering Journal*. Volume 136(1):50-65
- Barnes H. A. 2000. A handbook of elementary rheology. Institute of Non-Newtonian Fluid Mechanics. Aberystwyth: University of Wales
- Baudot C., Tan C. M., Kong J. C. 2010. FTIR spectroscopy as a tool for nanomaterial characterisation. *Infrared Physics and Technology*. Volume 53:434-438
- Benaissa H. 2009. Effect of temperature on methylene blue sorption from aqueous solutions by almond peel: Experimental studies and modelling. *Conference proceedings of the thirteenth international water technology conference held Hurghada Egypt*. Conducted by the University of Tlemcen. Algeria: Department of Chemistry-Faculty of Sciences
- Bhardwaj N., Kundu S.C. 2010. Electrospinning: A Fascinating fibre fabrication technique. *Biotechnology Advances*. Volume 28(3):325-347
- Bhattacharyya A., Kawi S., Ray M. B. 2004. Photocatalytic degradation of orange II by TiO<sub>2</sub> catalysts supported on adsorbents. *Catalysis Today*. Volume 98:431-439
- Blaskov V., Shipocka M., Stambolova I., Vassilev S., Eliyas A., Stefanov P., Loukanov A. 2012. Influence of titanium precursor on the photocatalytic properties of TiO<sub>2</sub> sprayed films under visible light. *Journal of Physics. Conference Series*. Volume 398:012021
- Budylina E. G., Azarova M. T., Shibaeva G. A. 1995. Chemical stability and use of thermostabilised polyacrylonitrile fibres. *Fibre Chemistry*. Volume 27(1):50-51
- Carp O., Huisman C. L., Reller A. 2004. Photoinduced reactivity of titanium dioxide. *Progress in Solid State Chemistry*. Volume 32:33-177

- Castaneda L., Alonso J.C., Ortiz A., Andrade E., Saniger J. M., Banuelos J. G. 2002. Spray pyrolysis deposition and characterisation of titanium oxide thin films. *Materials Chemistry and Physics*. Volume 77:938-944
- Chauvet O., Forro L. 1995. Magnetic properties of the anatase phase of TiO<sub>2</sub>. *Solid State Communications*. Volume 93(8):667-669
- Chen J. C., Harrison I. R. 2002. Modification of polyacrylonitrile (PAN) carbon fibre precursor via post-spinning plasticization and stretching in dimethyl formamide (DMF). *Carbon*. Volume 40:25-45
- Chen X., Mao S. S. 2007. Titanium dioxide nanomaterials: Synthesis, Properties, Modifications and applications. *Chemical Reviews*. Volume 107:2891-2959
- Chew S. Y., Wen Y., Dzenis Y., Leong K. W. 2006. The role of electrospinning in the emerging field of nanomedicine. *Current Pharmaceutical Design*. Volume 12(36):4751-4770
- Chong E. J., Phan T. T., Lim I. J., Zhang Y. Z., Bay B. H., Ramakrishna S., Lim C. T. 2007. Evaluation of electrospun PCL/gelatin nanofibrous scaffold for wound healing and layered dermal reconstruction. *Acta Biomaterialia*. Volume 3:321-330
- Chong M. N., Jin B., Chow C.W.K., Saint C. 2010. Recent developments in photocatalytic water treatment technology: A review. *Water research* (44):2997-3027
- Choy K. L. 2003. Chemical Vapour Deposition of Coatings. *Progress in Materials Science*. Volume 48:57-170
- Chuangchote S., Jitputti J., Sagawa T., Yoshikawa S. 2009. Photocatalytic activity for hydrogen evolution of electrospun TiO<sub>2</sub> nanofibres. *Applied Materials and Interfaces*. Volume 1(5):1140-1143
- Costolo M.A., Lennhoff J.D., Pawle R., Rietman E.A., Stevens A.E. 2008. A nonlinear system model for electrospinning sub-100nm polyacrylonitrile fibers. *Nanotechnology*. Volume 19:035707

- De los Milagros Ballari M., Rodolfo B., Alfano O., Cassano A. 2008. Mass transfer limitations in photocatalytic reactors employing titanium dioxide suspensions I. Concentration profiles in bulk. *Chemical Engineering Journal*. Volume 136:50-65
- De los Milagros Ballari M., Brandi Rodolfo., Alfano O., Cassano A. 2008. Mass transfer limitations in photocatalytic reactors employing titanium dioxide suspensions II. External and internal particle constrains for the reaction. *Chemical Engineering Journal*. Volume 136:242-255
- De Vrieze S., De Clerck K. 2009. 80 years of electrospinning. In: Kiekens P. *International conference on Latest Advances in High-Tech Textiles and Textile-Based Materials, Proceedings*. 60-63. Presented at the International conference on Latest Advances in High-Tech Textiles and Textile-Based Materials. Ghent, Belgium: Ghent University. Department of Textiles
- De Vrieze S., Van Camp T., Nelvig A., Hagström B., Westbroek P., De Clerck K. 2009. The effect of temperature and humidity on electrospinning. *Journal of Material Science*. Volume 44:1357-1362
- Demir M. M., Gulgun M. A., Menciloglu Y. Z. 2004. Palladium nanoparticles by electrospinning from poly(acrylonitrile-co-acrylic acid) – PdCl<sub>2</sub> solutions. Relations between preparation conditions, particle size, and catalytic activity. *Macromolecules*. Volume 37:1787-1792
- Demir M. M., Yilgor I., Yilgor E., Erman B. 2002. Electrospinning of polyurethane fibres. *Polymer*. Volume 43:3303-3309
- Diebold Ulrike. 2003. The surface science of titanium dioxide. *Surface Science Reports*. Volume 48:53-229
- Eda G., Liu J., Shivkumar S. 2007. Solvents effects on jet evolution during electrospinning of semi-dilute polystyrene solutions. *European Polymer Journal*. Volume 43:1154-1167

- Fan J., Cai W., Yu J. 2011. Adsorption of N719 dye on anatase TiO<sub>2</sub> nanoparticles and nanosheets with exposed (001) facets: equilibrium, kinetic, and thermodynamic studies. *Chemistry – An Asian Journal*. Volume 6(9):2481-2490
- Farsani R. E., Shokuhfar A., Sedghi A. 2007. Conversion of Modified Commercial Polyacrylonitrile Fibers to Carbon Fibers. *International Journal of Aerospace and Mechanical Engineering*. Volume 1(4):184-187
- Ferrari A.C. 2007. Raman spectroscopy of graphene and graphite: Disorder, electron phonon coupling, doping and nonadiabatic effects. *Solid State Communications*. Volume 143(1-2):47-57
- Fong H., Chun I., Reneker D. H. 1999. Beaded nanofibres formed during electrospinning. *Polymer*. Volume 40:4585-4592
- Fridrikh S.V., Yu J.H., Brenner M.P., Rutledge G.C. 2003. Controlling the fiber diameter during electrospinning. *Physical Review Letter*. Volume 90(14):144502
- Fryczkowski R., Gorczowska M., Fryczkowska B., Janicki J. 2013. The effect of solvent on the properties of nanofibres obtained by electrospinning from a mixture of poly(3-hydroxybutyrate) and polyaniline. *Synthetic Materials*. Volume 166:14-21
- Fujishima A., Honda K, Kikuchi S. 1969. Photosensitized electrolytic oxidation on TiO<sub>2</sub> semiconductor electrode. *Journal of Chemical Society Japan*. Volume 72:108-109.
- Fujishima A., Zhang X. 2006. Titanium dioxide photocatalysis: present situation and future approaches. *Comptes Rendus Chimie*. Volume 9:750-760
- Fujishima A., Zhang X., Tryk D. 2007. Heterogeneous photocatalysis: From water photolysis to applications in environmental cleanup. *International Journal of Hydrogen Energy*. Volume 32:2664-2672

- Fujishima A., Zhang X., Tryk D. A. 2008. TiO<sub>2</sub> photocatalysis and related surface phenomena. *Surface Science Reports*. Volume 63:515-582
- Gao B., Chen G.Z., Puma G.L. 2009. Carbon nanotubes/titanium dioxide (CNTs/TiO<sub>2</sub>) nanocomposites prepared by conventional and novel surfactant wrapping sol-gel methods exhibiting enhanced photocatalytic activity. *Applied Catalysis B: Environmental*. Volume 89(3-4):503-509
- Gao Y., Lui H., Ma M. 2007. Preparation and photocatalytic behaviour of TiO<sub>2</sub>-carbon nanotubes hybrid catalyst for acridine dye decomposition. *Reaction Kinetics and Catalysis Letters*. Volume 90(1):11-18
- Gaya U. I., Halim A., Abdullah A. H. 2008. Heterogeneous photocatalytic degradation of organic contaminants over titanium dioxide. A review of fundamentals, progress and problems. *Journal of Photochemistry and Photobiology C: Photochemistry Reviews*. Volume 8:1-12
- Godini K., Azarian G., Rahmani A. R., Zolghadrnasab H. 2013. Treatment of Waste Sludge: A comparison between Anodic Oxidation and Electro-Fenton Processes. *Journal of Research in Health Science*. Volume 13(2):188-193
- Goldstein S., Aschengrau D., Diamant Y., Rabani J. 2007. Photolysis of aqueous H<sub>2</sub>O<sub>2</sub>: Quantum yield and applications for polychromatic UV actinometry in photoreactors. *Environment Science and Technology*: Volume 41:7486-7490
- Gu S.Y., Ren J., Vancso G. J. 2005. Process optimization and empirical modelling for electrospun polyacrylonitrile precursor of carbon nanofibres. *European Polymer Journal*. Volume 41:2559-2568
- Hamzeh M., Sunahara G. I. 2013. In vitro and genotoxicity studies of titanium dioxide (TiO<sub>2</sub>) nanoparticles in Chinese hamster lung fibroblast cells. *Toxicology in Vitro*. Volume 27(2):864-873
- He J., Wan Y., Yu J. 2008. Effect of concentration on electrospun polyacrylonitrile nanofibres. *Fibers and Polymers*. Volume 9(2):140-142

- Herrmann J. M. 1999. Heterogeneous photocatalysis: fundamentals and applications to the removal of various types of aqueous pollutants. *Catalysis Today*. Volume 53:115-129
- Hintsho N.C. 2011. *Synthesis of Nanostructured Titanium Dioxide and Application in Water Treatment*. Masters Dissertation. Cape Town: University of the Western Cape.
- Hislop K. A., Bolton J. R. 1999. The photochemical generation of hydroxyl radicals in the UV-vis/ferrioxalate/H<sub>2</sub>O<sub>2</sub> system. *Environmental Science and Technology*. Volume 33:3119-3126
- Hohman M. M., Shin M., Rutledge G., Brenner M.P. 2001. Electrospinning and electricity forced jets. II. Applications. *Physics of Fluids*. Volume 13:2221-2236
- Hong Y., Li D., Zheng J., Zou G. 2006. Sol-growth of Titania from electrospun polyacrylonitrile nanofibres. *Nanotechnology*. Volume 17:1986-1993
- Houas A., Lachheb H., Ksibi M., Elaloui E., Guillard C., Herrmann J. 2001. Photocatalytic degradation pathway of methylene blue in water. *Applied Catalysis B: Environmental*. Volume 31:145-157
- Hu G., Meng X., Feng X., Ding Y., Zhang S., Yang M. 2007. Anatase TiO<sub>2</sub> nanoparticles/carbon nanotubes nanofibres: preparation, characterization and photocatalytic properties. *Journal of Material Science*. Volume 42:7162-7170
- Huang J., Virji S., Weiller B. H., Kaner R. B. 2002. Polyaniline nanofibres: Facile synthesis and chemical sensors. *Journal of American Chemical Society*. Volume 125:314-315
- Im J. S., Kim M., Lee Y. 2008. Preparation of PAN-based electrospun nanofibre webs containing TiO<sub>2</sub> for photocatalytic degradation. *Material Letters*. Volume 62:3652-3655
- Jackson, D. P. 2003. *Method, Process and apparatus for high pressure plasma catalytic treatment of dense fluids*. US Patent 2003/0146310A1

- Jalili R., Hosseini S., A., Morshed M. 2005. The effects of operating parameters on the morphology of electrospun PAN nanofibres. *Iranian Polymer Journal*. Volume 14(12):1074-1081
- Janotti A., Varley J. B., Rinke P., Umezawa N., Kresse G., Van de Walle C. G. 2010. Hybrid functional studies of oxygen vacancy in TiO<sub>2</sub>. *Physical Review*. Volume 81:085212
- Jensen H., Soloviev A., Li Z., Sogaard E. G. 2005. XPS and FTIR investigation of surface properties of different prepared titania nano-powders. *Applied Surface Science*. Volume 246:239-249
- Jiang D., Xu Y., Hou B., Wu D., Sun Y. 2007. Synthesis of visible light-activated TiO<sub>2</sub> photocatalyst via surface organic modification. *Journal of Solid State Chemistry*. Volume 180:1787-1791
- Jirsak O., Sanetrnik F., Lukas D., Kotek V., Martinova L., Chaloupek J. 2005. A method of nanofibres production from a polymer solution using electrostatic spinning and a device for carrying out the method. WO Patent 2005/024101
- Jung H., Kim H., Ahn J., Park J. 2004. Fabrication of recyclable catalyst supports for synthesis of carbon nanofibres. *Metals and materials International*. Volume 10(2):199-205
- Keller N., Rebmann G., Barraud E., Zahraa O., Keller V. 2005. Macroscopic carbon nanofibres for use as a catalyst support. *Catalysis Today*. Volume 101:323-329
- Khalil K. A., Fouad H., Elsarnagawy T., Almahjdi F. N. 2013. Preparation and characterization of electrospun PLGA/silver composite nanofibres for biomedical applications. *International Journal of Electrochemical Science*. Volume 8:3483-3493
- Kholmanov I. N., Barborini E., Vinati S., Piseri P., Podesta A., Ducati C., Lenardi C., Milani P. 2003. The influence of the precursor clusters on the structural and

- morphological evolution of nanostructured TiO<sub>2</sub> under thermal annealing. *Nanotechnology*. Volume 14:1168-1173
- Kim B., Bui N., Yang K. 2009. Electrochemical Properties of Activated Polyacrylonitrile/pitch Carbon Fibres Produced Using Electrospinning. *Bulletin Korean Chemical Society*. Volume 30(9):1967-1972
- Kim C. H., Kim B., Yang K. S. 2012. TiO<sub>2</sub> nanoparticles loaded on graphene/carbon composite nanofibres by electrospinning for increased photocatalysis. *Carbon*. Volume 50:2472-2481
- Klabunde K.J., Richards R.M. (Editors). 2009. *Nanoscale materials in chemistry*. New Jersey, United States: John Wiley and Sons Inc.
- Koci K., Obalova L., Matejova L., Placha D., Lacny Z., Jirkovsky J., Solcova O. 2009. Effect of TiO<sub>2</sub> particle size on the photocatalytic reduction of CO<sub>2</sub>. *Applied Catalysis B: Environmental*. Volume 89:494-502
- Kong C. S., Yoo W. S., Lee K. Y., Kim H. S. 2009. Nanofibre deposition by electroblowing of PVA (polyvinyl alcohol). *Journal of Material Science*. Volume 44:1107-1112
- Kongkanand A., Dominguez R., Kamat P. 2007. Single wall carbon nanotubes scaffolds for photoelectrochemical solar cells. Capture and transport of photogenerated electrons. *Nano Letters*. Volume 3(7):676-680
- Koski A., Yim K., Shivkumar S. 2004. Effect of molecular weight on fibrous PVA produced by electrospinning. *Material Letters*. Volume 58(3-4):493-497
- Krivec M., Segundo R. A., Faria J. L., Silva A. M. T., Drazic G. 2013. Low-temperature synthesis and characterization of rutile nanoparticles with amorphous surface layer for photocatalytic degradation of caffeine. *Applied Catalysis B: Environmental*. Volume 140-141:9-15
- Lee S., Kim J., Ku B., Kim J., Joh H. 2012. Structural evolution of polyacrylonitrile fibres in stabilisation and carbonisation. *Advances in Chemical Engineering and Sciences*. Volume 2:275-282

- Li D., Xia Y. 2003. Fabrication of Titania Nanofibres by electrospinning. *Nano Letters*. Volume 3(4):555-560
- Li H., Liu M., Zeng Y., Huang T. 2010. Coexistence of anti-ferromagnetic and ferromagnetic in Mn-doped anatase TiO<sub>2</sub> nanowires. *Journal of Central South University of Technology*. Volume 17:239-243
- Liang D., Hsiao B. S., Chu B. 2007. Functional electrospun nanofibrous scaffolds for biomedical applications. *Advanced Drug Delivery Reviews*. Volume 59:1392-1412
- Lin T., Wang H., Wang H., Wang X. 2005. Effects of polymer concentration and cationic surfactant on the morphology of electrospun polyacrylonitrile nanofibres. *Journal of Materials Science and Technology*. Volume 21(1):1-4
- Linsebigler A. L., Lu G., Yates J.T. 1995. Photocatalysis on TiO<sub>2</sub> surfaces: Principles, Mechanisms and selected results. *Chemical Reviews*. Volume 95(3):735-758
- Liu Y., He J. 2007. Bubble electrospinning for mass production of nanofibres. *International Journal of Nonlinear Sciences and Numerical Simulations*. Volume 8:393-396
- Liu Y., Ma G., Fang D., Xu J., Zhang H., Nie J. 2011. Effects of solution properties and electric field on the electrospinning of hyaluronic acid. *Carbohydrate Polymers*. Volume 83:1011-1015
- Liu Y., Yu H., Lv Z., Zhan S., Yang J., Peng X., Ren Y., Wu X. 2012. Simulated-sunlight-activated photocatalysis of methylene blue using cerium-doped SiO<sub>2</sub>/TiO<sub>2</sub> nanostructured fibers. *Journal of Environmental Sciences*. Volume 24(10):1867-1875
- Locke B. R., Finney W. C., Grymonpre D. R. 1996. *Accelerated methods of oxidizing organic contaminants in aqueous mediums using corona induced reactions and particles therewith*. Patent WO1996032175 A2

- Lue J. T., Nalwa H. S. (Editor). 2007. Physical properties of nanomaterials. *Encyclopedia of Nanoscience and Nanotechnology*. Volume X:1-46
- Lyons J., Li C., Ko F. 2004. Melt-electrospinning part I: processing parameters and geometric properties. *Polymer*. Volume 45(22):7597-7603
- Maitra T., Sharma S., Srivastava A., Cho Y., Madou M., Sharma A. 2012. Improved graphitisation and electrical conductivity of suspended carbon nanofibres derived from carbon nanotubes/polyacrylonitrile composites by directed electrospinning. *Carbon*. Volume 50:1753-1761
- Malkin A. Y. 2013. Non-Newtonian viscosity in steady-state shear flows. *Journal of non-Newtonian Fluid Mechanics*. Volume 192:48-65
- Manuel A., da Silva T. 2009. Environmental catalysis from nano- to macro-scale. *Materials and Technology*. Volume 43(3):113-121
- Mataram A., Ismail A.F., Abdullah M. S., Ng B. C. 2011. A review of assembled polyacrylonitrile-based carbon nanofibre prepared electrospinning process. *International Journal of Nanoscience*. Volume 10(3):455-469
- Matsumoto Y. 1996. Energy positions of oxide semiconductors and photocatalysis with iron complex oxides. *Journal of Solid State Chemistry*. Volume 126:227-234
- Mavhi A. H., Ghanbarian M., Nasserli S., Khairi A. 2009. Mineralization and discolouration of textile wastewater by TiO<sub>2</sub> nanoparticles. *Desalination*. Volume 239:309-316
- Mekprasart W., Khumtong T., Rattanak J., Techitdheera W., Pecharapa W. 2013. Effect of Nitrogen Doping on Optical and Photocatalytic Properties of TiO<sub>2</sub> Thin Film Prepared by Spin Coating Process. *Energy Procedia*. Volume 34:746-750
- Menesi J., Korosi L., Bazso E., Zollmer V., Richardt A., Dekany I. 2008. Photocatalytic oxidation of organic pollutants on titania-clay composites. *Chemosphere*. Volume 70:538-542

- Miller R.J., Bennett S., Keller A.A., Pease S., Lenihan H.S. (2012). TiO<sub>2</sub> nanoparticles are phototoxic to marine phytoplankton. *PLoS one*. Volume 7(1):1-7
- Mills A., Wang J. 1999. Photobleaching of methylene blue sensitized by TiO<sub>2</sub>: an ambiguous system? *Journal of photochemistry and photobiology A: Chemistry*. Volume 127:123-134
- Minceva-Sukarova B., Mangovska B., Bogoeva-Gaceva G., Petrusevski V. M. 2012. Micro-Raman and Micro-FT-IR spectroscopic investigation of raw and dyed PAN fibres. *Croatica Chemica Acta*. Volume 85(1):63-70
- Moafi H. F., Shojaie A. F., Zanjanchi M. A. 2011. Photoactive polyacrylonitrile fibres coated by nano-sized titanium dioxide: Synthesis, characterisation, thermal investigation. *Journal of the Chilean Chemical Society*. Volume 56(1):610-615
- Mohanty P., Mishra N. C., Choudhary R. J., Banerjee A., Shripathi T., Lalla N. P., Annapoorni S., Rath C. 2012. Oxygen vacancy induced phase formation and room temperature ferromagnetism in undoped and Co-doped TiO<sub>2</sub> thin films. *Journal of Physics D: Applied Physics*. Volume 45(32):325301-325309
- Munoz I., Rieradevall J., Torrades F., Peral J., Domenech X. 2005. Environmental assessment of different solar driven advanced oxidation processes. *Solar Energy*. Volume 79:369-375
- Nataraj S. K., Yang K. S., Aminabhavi T. M. 2012. Polyacrylonitrile-based nanofibres- A state-of-the-art review. *Progress in Polymer Science*. Volume 37:487-513
- Nayak R., Padhye R., Kyratzis I. L., Truong Y. B., Arnold L. 2011. Recent advances in nanofibre fabrication techniques. *Textile Research Journal*. Volume 82(2):129-147
- Nikazar M., Gholivan K., Mahanpoor K. 2007. Enhancement of photocatalytic efficiency of TiO<sub>2</sub> by supporting on clinoptilolite in the decolourisation of azo

- dye direct yellow 12 aqueous solutions. *Journal of the Chinese Chemical Society*. Volume 54:1261-1268
- Okolongo G. N., Buttner U., Petrik L., Perold W. J. 2011. *Photo-catalyst and its preparation*. South African patent 2011/03468.
- Okolongo G. N., Buttner U., Petrik L., Perold W. J. 2011. *Water Treatment Apparatus*. South African patent 2011/03467.
- Oliveira F., Monteiro S. R., Barros-Timmons A., Lopes-da-Silva J. A. 2010. Weak-gel formation dispersion of silica particles in matrix of a non-ionic polysaccharide: Structure and rheological characterization. *Carbohydrate Polymers*. Volume 82:1219-1227
- Ono Y., Rachi t., Okuda T., Yokouchi M., Kamimoto Y., Nakajima A., Okada K. 2012. Kinetic study for photodegradation of methylene blue dye by titanium dioxide powder prepared by selective leaching method. *Journal of Physics and Chemistry of Solids*. Volume 73:343-349
- Paquien J., Galy J., Gerard J., Pouchelon A. 2005. Rheological studies of fumed silica-polydimethylsiloxane suspensions. *Colloids and Surfaces A: Physicochemical Engineering Aspects*. Volume 260: 165-172
- Patel A.C., Li S., Wang C., Zhang W., Wei Y. 2007. Electrospinning of porous silica nanofibres containing silver nanoparticles for catalytic applications. *Chemistry of Materials*. Volume 19:1231-1238
- Prahsarn C., Klinsukhon W., Roungpaisan N. 2011. Electrospinning of PAN/DMF/H<sub>2</sub>O containing TiO<sub>2</sub> and photocatalytic activity of their webs. *Material Letters*. Volume 65:2498-2501
- Qin X., Wang S. 2008. Interior structure of polyacrylonitrile (PAN) nanofibres with LiCl. *Materials Letters*. Volume 62:1325-1327
- Qin X., Wan Y., He J., Zhang J., Yu J., Wang S. 2004. Effect of LiCl on electrospinning of PAN polymer solution: theoretical analysis and experimental verification. *Polymer*. Volume 45:6409-6413

- Qui Y., Yu J. 2008. Synthesis of titanium dioxide nanotubes from electrospun fibre templates. *Solid State Communications*. Volume 48:556-558
- Raghavan P., Lim D., Ahn J., Nah C., Sherrington D. C., Ryu H., Ahn H. 2012. Electrospun polymer nanofibres: The booming cutting edge technology. *Reactive and Functional Polymers*. Volume 72:915-930
- Rahaman M. S. A., Ismail A. F., Mustafa A. 2007. A review of heat treatment on polyacrylonitrile fibre. *Polymer Degradation and Stability*. Volume 92:1421-1432
- Ramakrishna S., Fujihara K., Teo W., Yong T., Ma Z., Ramaseshan R. 2006. Electrospun nanofibres: Solving global issues. *Materials Today*. Volume 9(3):40-50
- Reddy P. M. K., Raju B. R., Karuppiiah J., Reddy E. L., Subrahmanyam C. 2013. Degradation and mineralization of methylene blue by dielectric barrier discharge non-thermal plasma reactor. *Chemical Engineering Journal*. Volume 217:41-47
- Rejeski D., Lekas D. 2008. Nanotechnology field observations: scouting the new industrial west. *Journal of Cleaner Production*. Volume 16:1014-1017
- Rincon A. G., Pulgarin C. 2003. Photocatalytic inactivation of E. coli: effect of (continuous-intermittent) light intensity and of (suspended-fixed) TiO<sub>2</sub> concentration. *Applied Catalysis B: Environmental*. Volume 44:263-284
- Rittner F., Boddenberg B., Fink R. F., Staemmler V. 1999. Adsorption of nitrogen on rutile (110). 2. Construction of full five-dimensional potential energy surface. *Langmuir*. Volume 15:1449-1455
- Roth S. V., Herzog G., Korstgens V., Buffet A., Schwartzkopf M., Perlich J., Kashem M. M. A., Dohrmann R., Gehrke R., Rothkirch A., Stassig K., Wurth W., Benecke G., Li C., Fratzl P., Rawolle M., Muller-Buschbaum P. 2011. In situ observation of cluster formation during nanoparticle solution casting on a colloidal film. *Journal of Physics: Condensed Matter*. Volume 23:254208

- Roux S. P. 2008. *Nanopollutants, their effects on the environment, and potential impacts on South African water treatment and supply infrastructure*. Technical Report. pp 40. [<http://hdl.handle.net/10204/3289>]
- Santos E. B., de Souza e Silva J. M., Mazali I.O. 2010. Raman spectroscopy as a tool for the elucidation of nanoparticles with core-shell structure of TiO<sub>2</sub> and MoO<sub>3</sub>. *Vibrational Spectroscopy*. Volume 54:89-92
- Scharnag N., Buschatz H. 2001. Polyacrylonitrile (PAN) membranes for ultra- and microfiltration. *Desalination*. Volume 139:191-198
- Senthilnathan J., Philip L. 2010. Photocatalytic degradation of lindane under UV and visible light using N-doped TiO<sub>2</sub>. *Chemical Engineering Journal*. Volume 161:83-92
- Sharma R., Bisen D. P., Shukla U., Sharma B. G. 2012. X-ray diffraction: a powerful method of characterising nanomaterials. *Recent Research in Science and Technology*. Volume 4(8)77-79
- Shi J., Chen S., Ye Z., Wang S., Wu P. 2010. Favourable recycling photocatalyst TiO<sub>2</sub>/CFA: Effects of loading percent of TiO<sub>2</sub> on the structural property and photocatalytic activity. *Applied Surface Science*. Volume 257(3):1068-1074
- Shi Z., Fan Y., Xu N., Shi J. 2000. Kinetics of photocatalytic degradation of methylene blue over TiO<sub>2</sub> particles in aqueous suspensions. *Chinese Journal of Chemical Engineering*. Volume 8(1):15-19
- Shinde P.S., Sadale S. B., Patil P. S., Bhosale P. N., Bruger A., Neumann-Spallart M., Bhosale C. H. 2008. Properties of spray deposited titanium dioxide thin films and their application in photoelectrocatalysis. *Solar Energy Materials & Solar Cells*. Volume 92:283290
- Shrestha N. K., Yang M., Nah Y., Paramasivam I., Schmuki P. 2010. Self-organised TiO<sub>2</sub> nanotubes: Visible light activation by Ni oxide nanoparticles decoration. *Electrochemistry Communications*. Volume 12:254-257

- Smith E., Dent G. 2005. *Modern Raman Spectroscopy – A practical approach*. Chichester. John Wiley & Sons Ltd.
- Snovski R., Grinblat J., Sougrati M., Jumas J., Margel S. 2014. Synthesis and characterization of iron, iron oxide and iron carbide nanostructures. *Journal of Magnetism and Magnetic Materials*. Volume 349:35-44
- Stanger J., Tucker N., Kirwan K., Coles S., Jacobs D., Staiger M. P. 2009. Effect of charge density on the Taylor cone in electrospinning. *International Journal of Modern Physics B*. Volume 23:1956-1961
- Stoilova O., Manolova N., Gabrovska K., Marinov I., Godjevargova T., Mita D. G., Rashkov I. 2010. Electrospun polyacrylonitrile nanofibrous membranes tailored for acetylcholinesterase immobilization. *Journal of Bioactive and Compatible Polymers*. Volume 25:40-57
- Stuart B.H. 2004. *Infrared Spectroscopy: Fundamentals and Applications*. Wiley. Available at: <https://www.kinetics.nsc.ru/chichinin/books/spectroscopy/Stuart04.pdf> [Accessed 18 October 2013]
- Tan S. H., Inai R., Kotaki M., Ramakrishna S. 2005. Systematic parameter study for ultra-fine fiber fabrication via electrospinning process. *Polymer*. Volume 46:6128-6134
- Thamaphat K., Limsuwan P., Ngotawornchai B. 2008. Phase characterization of TiO<sub>2</sub> powder by XRD and TEM. *Natural Science*. Volume 42:357-361
- Theivasanthi T., Alagar M. 2013. Titanium dioxide (TiO<sub>2</sub>) nanoparticles – XRD Analyses – An insight. eprint arXiv.1307.1091
- Thompson C.J., Chase G. G., Yarin A. L., Reneker D. H. 2007. Effects of parameters on nanofibre diameter determined from electrospinning model. *Polymer*. Volume 48:6913-6922
- Torimoto T., Ito S., Kuwabata S., Yoneyama H. 1996. Effects of adsorbents used as supports for titanium dioxide loading on photocatalytic degradation of

- propyzamide. *Environmental Science and Technology*. Volume 30(4):1275-1281
- Tschirch J., Dillert R., Bahnemann D., Proft B., Biedermann A., Goer B. 2008. Photodegradation of methylene blue in water, a standard method to determine the activity of photocatalytic coatings. *Research on Chemical Intermediates*. Volume 34(4):381-392
- Tuck S. J., Leach M. K., Feng Z., Corey J. M. 2012. Critical variables in the alignment of electrospun PLLA nanofibres. *Material Science and Engineering*. Volume C(32):1779-1784
- Umar M., Aziz H. A. 2013. Photocatalytic degradation of organic pollutants in water. Rashed M. N. (Ed.), *Organic Pollutants – Monitoring, Risks and Treatment*. Rijeka: InTec, 195-208
- Uyar T., Besenbacher F., 2008. Electrospinning of uniform polystyrene fibers: The effect of solvent conductivity. *Polymer*. Volume 49: 5336-5343
- Van der Schueren L., De Schoenmaker B., Kalaoglu O. I., De Clerck K. 2011. An alternative solvent system for the steady state electrospinning of polycaprolactone. *European Polymer Journal*. Volume 47:1256-1263
- Varabhas J., Chase G., Reneker D. 2008. Electrospun nanofibres from a porous hollow tube. *Polymer*. Volume 49:4226-4229
- Vinu R., Madras G. 2010. Environmental remediation by photocatalysis. *Journal of the Indian Institute of Science*. Volume 90(2):189-230
- Vitousek P. M., Mooney H. A., Lubchenco J., Melillo J. M. 1997. Human domination of earth's ecosystem. *Science*. Volume 277(5325):494-499
- Wang C., Casper F., Gasi T., Ksenofontov V., Balke B., Fecher G. H., Felser C., Hwu Y., Lee J. 2012. Structural and magnetic properties of Fe<sub>2</sub>CoGa Heusler nanoparticles. *Journal of Physics D: Applied Physics*. Volume 45:295001-295008

- Wang J., Yue Z., Ince J. S., Economy J. 2006. Preparation of nanofiltration membranes from polyacrylonitrile ultrafiltration membranes. *Journal of Membrane Science*. Volume 286:333-341
- Wang X., Ding B., Sun G., Wang M., Yu J. 2013. Electro-spinning/netting: A strategy for the fabrication of three dimensional polymer nano-fibre/nets. *Progress in Material Science*. Volume 58(8):1173-1243
- Wang X., Um I., Fang D., Okamoto A., Hsiao B., Chu B. 2005. Formation of water-resistant hyaluronic acid nanofibres by blowing-assisted electrospinning and non-toxic post treatments. *Polymer*. Volume 46:4853-4867
- Wang X., Yu J. C., Ho C., Hou Y., Fu X. 2005. Photocatalytic activity of a hierarchically macro/mesoporous titania. *Langmuir*. Volume 21:2552-2559
- Wangxi Z., Jie L., Gang W. 2003. Evolution of structure and properties of PAN precursors during their conversion to carbon fibres. *Carbon 41*. Volume 41:2805-2812
- Wannatong L., Sirivat A., Supaphol P. 2004. Effects of solvents on electrospun polymeric fibers: preliminary study on polystyrene. *Polymer International*. Volume 53:1851-1859
- Wilhelm P., Stephan D. 2007. Photodegradation of rhodamine B in aqueous solution via SiO<sub>2</sub> at TiO<sub>2</sub> nano-spheres. *Journal of photochemistry and photobiology A: Chemistry*. Volume 185:19-25
- Willis A. L., Chen Z., He J., Zhu Y., Turro N. J., O'Brien S. 2007. Metal acetylacetonates as general precursors for the synthesis of early transition metal oxide nanomaterials. *Journal of Nanomaterials*. Volume. 14858:1-7
- Woan K., Pyrgiotakis G., Sigmund W. 2009. Photocatalytic carbon-nanotube-TiO<sub>2</sub> composites. *Advanced Materials*. Volume 21:2233-2239
- Wu C., Chern J. 2006. Kinetics of photocatalytic decomposition of methylene blue. *Industrial and Engineering Chemistry Research*. Volume 45:6450-6457

- Xiao Q., Zhang J., Xiao C., Si Z., Tan X. 2008. Solar photocatalytic degradation of methylene blue in carbon-doped TiO<sub>2</sub> nanoparticle suspension. *Solar energy*. Volume 82:706-713
- Yang Q., Li Z., Hong Y., Zhao Y., Qiu S., Wang C., Wei Y. 2004. Influence of solvents on the formation of ultra thin uniform poly(vinylpyrrolidone) nanofibres with electrospinning. *Journal of Polymer Science Part B Polymer Physics*. Volume 42(20):3721-3726
- Yang R., He J., Xu L., Yu J. 2009. Bubble-electrospinning for fabrication of nanofibres. *Polymer*. Volume 50:5846-5850
- Yordem O.S., Papila M., Menciloglu Y. Z. 2008. Effects of electrospinning parameters on polyacrylonitrile nanofibre diameter: An investigation by response surface methodology. *Materials and Design*. Volume 29:34-44
- Yu D. G., Branford-White C., White K., Chatterton N. P., Zhu L. M., Huang L. Y., Wang B. 2011. A modified coaxial electrospinning for preparing fibres from a high concentration polymer solution. *Polymer Letters*. Volume 5(8)732-741
- Yu L., Yu H., Lv Z., Zhan S., Yang J., Peng X., Ren Y., Wu X. 2012. Simulated-sunlight-activated photocatalysis of Methylene Blue using cerium-doped SiO<sub>2</sub>/TiO<sub>2</sub> nanostructured fibres. *Journal of Environmental Sciences*. Volume 24(10):1867-1875
- Yusof N., Ahmad A. F. 2010. Preparation and characterization of polyacrylonitrile/acrylamide-based activated carbon fibres developed using a solvent-free coagulation process. *International Journal of Chemical and Environmental Engineering*. Volume 1(2):79-84
- Yusof N., Ismail A. F. 2012. Post spinning and pyrolysis processes of polyacrylonitrile (PAN)-based carbon fibre and activated carbon fibre: A review. *Journal of Analytical and Applied Pyrolysis*. Volume 93:1-13

- Zhang C., Yuan X., Wu L., Han Y., Sheng J. 2005. Study on morphology of electrospun poly (vinyl alcohol) mats. *European Polymer Journal*. Volume 41:423-432
- Zhang J., Maurer F. H. J., Yang M. 2011. In situ formation of TiO<sub>2</sub> in electrospun poly (methyl methacrylate) nanohybrids. *The Journal of Physical Chemistry*. Volume 115:10431-10441
- Zhang T., Oyama T., Aoshima A., Hidaka H., Zhao J., Serpone N. 2001. Photooxidative *N*-demethylation of methylene blue in aqueous TiO<sub>2</sub> dispersion under UV irradiation. *Journal of Photochemistry and Photobiology A: Chemistry*. Volume 140:163-172
- Zhang W., Wang Y., Sun C. 2007. Characterization on oxidative stabilisation of polyacrylonitrile nanofibres prepared by electrospinning. *Journal of Polymer Research*. Volume 14:467-474
- Zhang X., Goux W. J., Manohar S. K. 2004. Synthesis of polyaniline nanofibres by “nanofibre seeding”. *Journal of American Chemical Society*. Volume 126:4502-4503
- Zhang X., Yin L., Tang M., Pu Y. 2010. Optimized method for preparation of TiO<sub>2</sub> nanoparticles dispersion for biological study. *Journal of Nanoscience and Nanotechnology*. Volume 10(8):5213-5219
- Zhao J., Jia C., Duan H., Li H., Xie E. 2007. Structural properties and photoluminescence of TiO<sub>2</sub> nanofibres were fabricated by electrospinning. *Journal of Alloys and Compounds*. Volume 461:447-450
- Zhu Y., Wilding M. A. 1996. Estimation, using infrared spectroscopy, of the cyclization of poly(acrylonitrile) during the stabilisation stage of carbon fibre production. *Journal of Material Science*. Volume 31:3831-3837

## APPENDIX

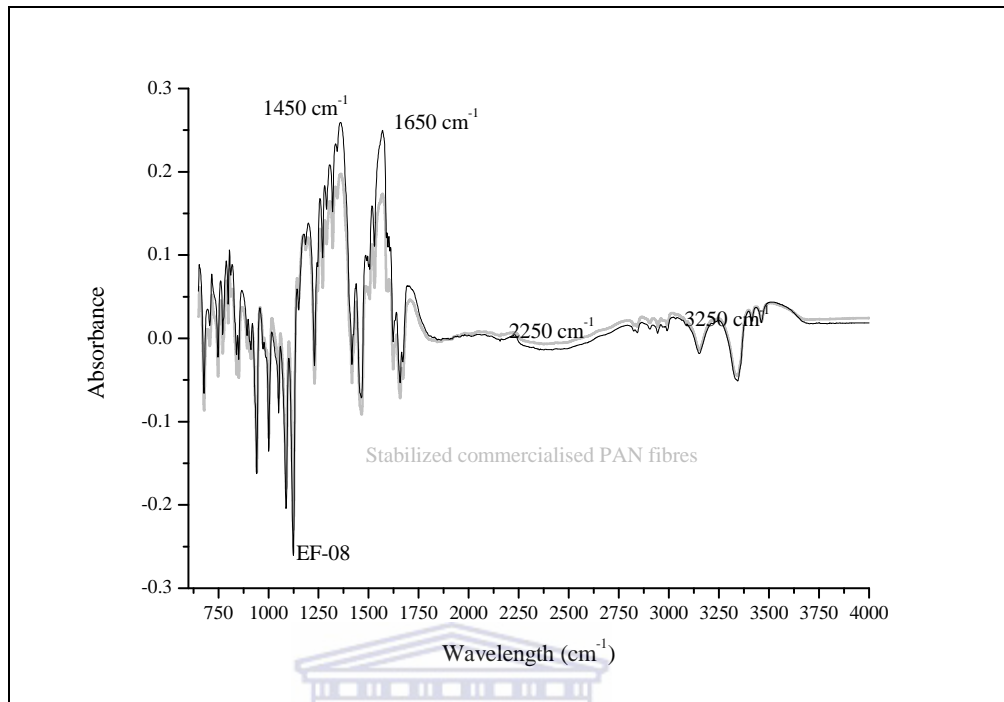


Figure A1: FTIR absorbance spectra of EF-08 over the mid-infrared region ( $4000 - 650 \text{ cm}^{-1}$ )

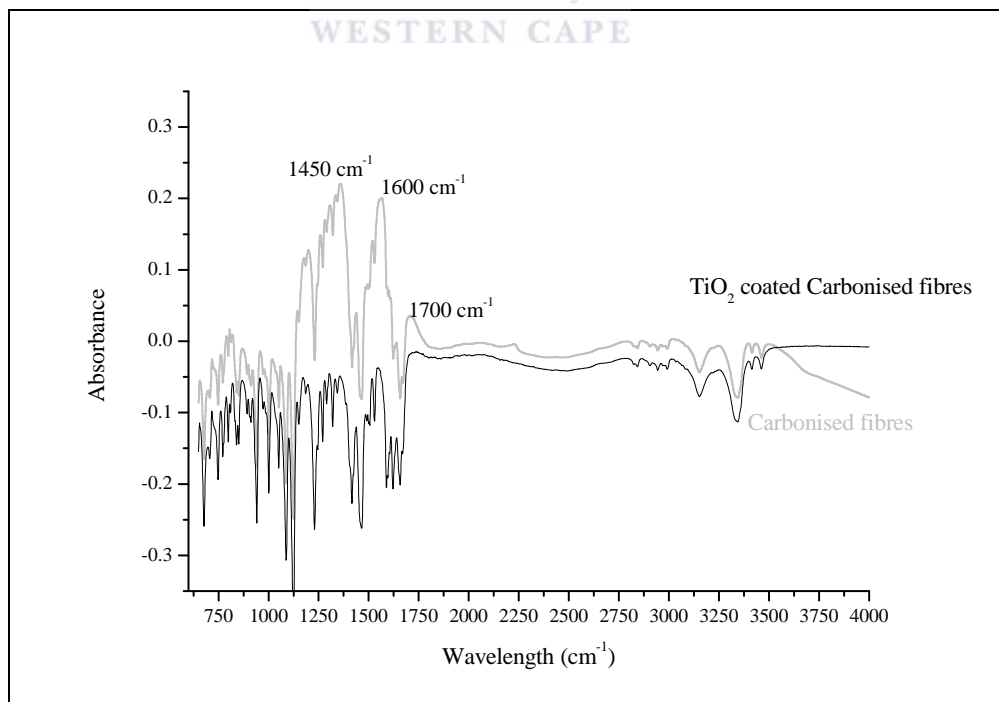


Figure A2: FTIR absorbance spectra of EF-12 over the mid-infrared region ( $4000 - 650 \text{ cm}^{-1}$ )

Table A1: The decolouration of MB during the photocatalyst study at 2 hour intervals for the commercial powder TiO<sub>2</sub>

Methylene blue degradation A - 665nm Bare TiO <sub>2</sub>		Concentration	ln (C/Co)	k	Removal %
0	1.809	9.220	0.000	0	0.00
2	0.855	4.358	-0.749	-0.375	52.74
4	0.716	3.649	-0.927	-0.232	60.42
6	0.612	3.119	-1.084	-0.181	66.17
8	0.576	2.936	-1.144	-0.143	68.16

Table A2: The decolouration of MB during the experiment at 2 hour intervals for the EF-04 series of electrospun nanofibres

Methylene blue degradation A - 665nm EF – 04a		Concentration	ln (C/Co)	k	Removal %
0	1.701	8.670	0.000	0	0.00
2	0.982	5.005	-0.549	-0.275	42.27
4	0.636	3.242	-0.984	-0.246	62.61
6	0.388	1.978	-1.478	-0.246	77.19
8	0.221	1.126	-2.041	-0.255	87.01

Methylene blue degradation A - 665nm EF- 04b		Concentration	ln (C/Co)	k	Removal %
0	1.662	8.471	0.000	0	0.00
2	1.136	5.790	-0.381	-0.190	31.65
4	0.593	3.022	-1.031	-0.258	64.32
6	0.264	1.346	-1.840	-0.307	84.12
8	0.108	0.550	-2.734	-0.342	93.50

Methylene blue degradation A - 665nm EF – 04c		Concentration	ln (C/Co)	k	Removal %
0	1.643	8.374	0.000	0	0.00
2	1.167	5.948	-0.342	-0.171	28.97
4	0.82	4.179	-0.695	-0.174	50.09
6	0.565	2.880	-1.067	-0.178	65.61
8	0.375	1.911	-1.477	-0.185	77.18

Methylene blue degradation A - 665nm EF- 04d		Concentration	ln (C/Co)	k	Removal %
0	1.737	8.853	0.000	0	0.00
2	1.479	7.538	-0.161	-0.080	14.85
4	1.097	5.591	-0.460	-0.115	36.85
6	0.836	4.261	-0.731	-0.122	51.87
8	0.615	3.135	-1.038	-0.130	64.59

Table A3: The decolouration of MB during the photocatalyst study with sampling performed at 2 hour intervals for the EF-05 – EF-08 series nanofibres

Methylene blue degradation A - 665nm EF-05		Concentration	ln (C/Co)	k	Removal %
0	2.096	10.683	0.000	0	0.00
2	1.354	6.901	-0.437	-0.218	35.40
4	1.132	5.770	-0.616	-0.154	45.99
6	1.094	5.576	-0.650	-0.108	47.81
8	1.248	6.361	-0.518	-0.065	40.46

Methylene blue degradation A - 665nm EF-06		Concentration	ln (C/Co)	k	Removal %
0	2.29	11.672	0.000	0	0.00
2	1.394	7.105	-0.496	-0.248	39.13
4	1.364	6.952	-0.518	-0.130	40.44
6	1.265	6.448	-0.593	-0.099	44.76
8	1.33	6.779	-0.543	-0.068	41.92

Methylene blue degradation A - 665nm EF-07		Concentration	ln (C/Co)	k	Removal %
0	2.126	10.836	0.000	0	0.00
2	1.657	8.445	-0.249	-0.125	22.06
4	1.516	7.727	-0.338	-0.085	28.69
6	1.484	7.564	-0.360	-0.060	30.20
8	1.505	7.671	-0.345	-0.043	29.21

Methylene blue degradation A - 665nm EF-08		Concentration	ln (C/Co)	k	Removal %
0	2.19	11.162	0.000	0	0.00
2	1.58	8.053	-0.326	-0.163	27.85
4	1.51	7.696	-0.372	-0.093	31.05
6	1.436	7.319	-0.422	-0.070	34.43
8	1.304	6.646	-0.518	-0.065	40.46

Table A4: The decolouration of MB during the photocatalyst study with sampling performed at 2 hour intervals for the EF-09 – EF-12 series nanofibres

Methylene blue degradation A - 665nm EF-09		Concentration	ln (C/Co)	k	Removal %
0	1.666	8.491	0.000	0	0.00
2	1.578	8.043	-0.054	-0.027	5.28
4	1.598	8.145	-0.042	-0.010	4.08
6	1.6	8.155	-0.040	-0.007	3.96
8	1.598	8.145	-0.042	-0.005	4.08

Methylene blue degradation A - 665nm EF-10		Concentration	ln (C/Co)	k	Removal %
0	1.676	8.542	0.000	0	0.00
2	1.596	8.135	-0.049	-0.024	4.77
4	1.591	8.109	-0.052	-0.013	5.07
6	1.643	8.374	-0.020	-0.003	1.97
8	1.621	8.262	-0.033	-0.004	3.28

Methylene blue degradation A - 665nm EF- 11		Concentration	ln (C/Co)	k	Removal %
0	1.699	8.660	0.000	0	0.00
2	1.667	8.496	-0.019	-0.010	1.88
4	1.667	8.496	-0.019	-0.005	1.88
6	1.693	8.629	-0.004	-0.001	0.35
8	1.716	8.746	0.010	0.001	-1.00

Methylene blue degradation A - 665nm EF - 12		Concentration	ln (C/Co)	k	Removal %
0	1.723	8.782	0.000	0	0.00
2	1.683	8.578	-0.023	-0.012	2.32
4	1.703	8.680	-0.012	-0.003	1.16
6	1.715	8.741	-0.005	-0.001	0.46
8	1.772	9.032	0.028	0.004	-2.84

